2013-09-12

Deformation Mechanisms in Bioinspired Multilayered Materials

Sina Askarinejad
Worcester Polytechnic Institute

Mechanics of Biological and Bioinspired Multilayered Materials

by

Sina Askarinejad

A Dissertation

Submitted to the Faculty

of the

WORCESTER POLYTECHNIC INSTITUTE

In partial fulfillment of the requirements for the

Degree of Doctor of Philosophy

in

Mechanical Engineering

December 2017

APPROVED:

Prof. Nima Rahbar, Major Thesis Advisor _____

Prof. Winston Soboyejo, Dissertation Committee _____

Prof. Leonard Albano, Dissertation Committee _____

Prof. Cagdas Onal, Dissertation Committee _____

Prof. Mark Richman, Committee Chair _____

Abstract

Light structural materials such as ceramics that possess high strength and toughness have wide applications across many engineering disciplines. Nature through the process of evolution has designed complex and effective microstructures with superb mechanical properties. Natural composites such as nacre, bone and bamboo are prime examples of such materials with high strength, stiffness and toughness. Understanding the microstructure, and multi-scale toughening and strengthening mechanisms in these materials provide a strong basis in design of next generation advanced composites. We initially extensively studied mechanics of nacreous structures using nonlinear finite element analysis. We show that the existing of pillars in the microstructure of nacre play a significant role in their strength. This is followed by fabrication of nacre-inspired ceramic/polymer composites using freeze-casting method. This self-assembly manufacturing technique was initially used to make lamellar structures of alumina nanoparticles and ice. Later, lyophilization was employed to remove the ice from the structure and, the porous ceramic scaffolds were sintered. Two different polymers were then infiltrated into the porous structures. Each fabricated composite was cut in dimensions suitable for mechanical and fracture tests. In the next phase of this study, shear-lag theory was employed to analytically investigate the mechanics of these composites. Effective mechanical properties of nacre-inspired composites were derived and presented. The experimental and analytical results were compared, and different aspects of the results were discussed. The crack-resistance curve and toughening mechanisms in these samples were also studied. Moreover, the effect of interface properties on mechanical response of nacre and nacre-inspired materials were explored. These results solve important mysteries about nacre and emphasize the role of organic-inorganic interface properties on the overall mechanical properties. We believe that natural composites are great source of inspiration, and there are valuable lessons that can be learned from nature to effectively design and fabricate high performing structural composites. Here we tried to shed a light on some of these inspirations. Additionally, in this thesis, mechanical and fracture properties of bamboo samples were explored theoretically and experimentally. Different toughening mechanisms along with crack-resistance curve were studied.

Acknowledgment

First and foremost, I want to express my sincerest gratitude to my supervisor, Prof. Nima Rahbar, for his supervision, advice, and guidance throughout the research. I attribute my PhD to his encouragement and effort; without him, this thesis would not have been completed or written. I could not have imagined having a better advisor and mentor for my Ph.D study.

I would like to thank my thesis committee members, Prof. Winston Soboyejo, Prof. Leonard Albano, Prof. Cagdas Onal, and Prof. Mark Richman for their insightful comments and invaluable advice. I also thank our laboratory technicians, Donald Pelegrino and Russ Lang for all their helps and suggestions.

I am extraordinarily fortunate in having so many friends during my time at Worcester Polytechnic Institute. They helped me without any persuasion to complete my dissertation. Siamak G. Faal, Shadi T. Kalat, Sina Yousseffian, Naser Pourakbar Sharifi, Jessica Rosewitz, Giuseppe Ardito, Arvand Navabi and Habibeh Ashouri, thank you all. I also owe so much to the people of 923 Pleasant st., 21 Lancaster st., 5 Hackfeld rd. and 19 Lee st., for being there everyday to make me laugh, so thank you Mohammadreza Moharrami, Hossein Salahshoor, Amirmahdi Ghasemi, Ali Moradi, Shahin Hajilar, Siavash Vahidi and Milad Farzad, for taking care of me. You are more important to me than you realize.

Last but not the least, I would like to thank my parents, my brother, Hossein, and sister, Sara for supporting me spiritually throughout my PhD but more important for their unconditional love. This dissertation would be incomplete without mentioning the support given by my love, Faezeh Shalchy, to whom this dissertation is also dedicated. Without her lifting me up when this thesis seemed interminable, I doubt it would ever have been completed.

Finally, I acknowledge National Science Foundation for funding this research.

Published Content

Chapter 2 has been adapted from:

Askarinejad, S., & Rahbar, N. (2015). Toughening mechanisms in bioinspired multilayered materials. Journal of The Royal Society Interface, 12(102), 20140855.

Chapter 6 has been adapted from:

Askarinejad, S., Kotowski, P., Youssefian, S., & Rahbar, N. (2016). Fracture and mixed-mode resistance curve behavior of bamboo. Mechanics Research Communications, 78, 79-85.

Chapter 7 has been adapted from:

Askarinejad, S., Kotowski, P., Shalchy, F., & Rahbar, N. (2015). Effects of humidity on shear behavior of bamboo. Theoretical and Applied Mechanics Letters, 5(6), 236-243.

Contents

List of Figures

List of Tables

1

Background

Significant research in the past has been focused on improving the mechanical properties of lightweight structural materials due to the large demand in bioengineering, aerospace, automotive, armor and construction applications. This primarily includes advanced structural materials which are lightweight materials with outstanding mechanical properties such as strength and toughness. Meanwhile, there are various materials in nature that inherently have these exceptional mechanical properties [1], and there is, therefore, a great interest in understanding and analyzing the structure and mechanical behavior of these materials [2]-[7]. Evolution has brought about beautiful optimized solutions to many problems. Nacre [8], mantis shrimp club [9], bone [10], deep sea sponge [11], bamboo [12, 13] and elk antler [14] are some of these structural biological materials. In this thesis, nacre and bamboo which possess hierarchical structure and toughening mechanisms were studied. The final goal of this study is to use these material and the lessons we can learn from their deformation mechanisms in order to design and fabricate advanced composites.

1.1 Nacre

Layered structure and super-strong interface in nacre is the origin of high strength, stiffness and toughness [15]. Nacre is a natural biocomposite made aragonite platelets biological macromolecules. The volume fraction of the organic phase is around 5%. This phase is extremely important in nacre's fracture toughness [16, 17]. Previous research on this natural material has shown

that its layered brick and mortar structure is the origin of the remarkable mechanical properties [17]. The inorganic phase exists as polygonal tablets with 3-5 μm diameters and the organic phase has a thichess of around 20 nm. The simple brick and mortar structure make the material so much tougher than than its constituents. The Young's modulus of nacre is reported to be around 70 GPa and its tensile strength has been reported to be around 170 MPa [18].

1.2 Bamboo

In recent years, there has been increasing interest in the use of bamboo, the fast growing naturally occurring bio-composite material, as an eco-friendly structural material [19]-[22]. This interest is due to the bamboo's attractive combinations of relatively high strength-to-weight ratio, stiffness-to-weight ratio and shape factor [21]-[25]. Such unique properties has resulted in structural applications of bamboo in bicycles and housing in rural and urban environments [26]. In countries such as China, bamboo has been used as structural material for centuries [27]. Bamboo has also been used to fabricate structural elements and as alternative to steel in reinforced concrete [28].

Excluding the outer layer (epidermial layer) of bamboo stalk, its structure consists of fibers and vascular bundles that are surrounded by parenchyma cells. Researchers attribute the outstanding mechanical properties of bamboo to the presence of the fibers which are non-uniformly distributed in the cross section of bamboo [29, 30]. The structure of the fibers in which cellulose fibrils are surrounded by a matrix of mainly lignin and hemicellulose has also been previously investigated [31]-[33]. Between 20% and 30% of the cross-sectional area of the stalk is made of longitudinal fibers which are heavily concentrated near the exterior layer [34]. The non-uniform distribution and the orientation of these fibers makes bamboo an orthotropic material with high strength along the fibers, and low strength transversal to the fibers [35]-[37]. Moreover, due to this structure, bamboo is a representative of a natural Functionally Graded Material (FGM) [38]-[39].

FGMs may be characterized by their variation in composition and structure over volume. This variation results in corresponding changes in the properties of the material in a continuous manner which may reduce the stress concentration and increase bonding strength [40]-[42]. However, in spite of

its structural application, there have been very few mechanistic studies of the toughening mechanisms in bamboo [24]. There have also been no such studies that clearly show the resistance curve behavior of bamboo. Instead, most of the prior studies have involved the use of topology optimization in the understanding of deformation, and studies of mechanical properties [43, 44].

2

Preliminary Finite Element Analysis on Nacreous Structure

2.1 Introduction

Learning lessons from nature is a key element in the design of tough and strong composites. Many biological materials are composites with outstanding mechanical properties, while the microstructural components from which they are made do not possess similar properties. Nacre is a wonder of nature in its mechanical properties in terms of strength and toughness. This structural material exhibits a toughness (in energy terms) some orders of magnitude higher than that of its primary component ($CaCO_3$), and its strength is among the highest in shell structures [45]-[47]. Inspired by this structure, there have been significant efforts in the past decades to synthesize new materials with mechanical performance comparable to nacre [48]-[57]. The essence of success is to understand the deformation mechanisms inherent in nacre. Hence, mechanical models are needed in order to answer these fundamental questions. The main goal of this study is to explain the basic deformation and toughening mechanisms and the resulting stress distribution in nacre-like multilayered materials through different stages of deformation.

Nacre is a natural composite made of 95 % brittle aragonite platelets ($CaCO_3$ tablet) [17] and only 5 % biological macromolecules which has an important effect on nacre's fracture resistance [58]. The elastic modulus of the aragonite is generally assumed to be about $E = 100$ GPa [45, 59]. A relatively thick (0.2-0.9 μm) and brittle aragonite is separated by nano-scale

inter-layers (approximately 20 nm). The mineral layer exists as closely packed polygonal tablets (3-5 μm diameters), separated by a nano-scale organic gap. The tensile strength and Young's modulus of wet nacre are reported to be approximately 140 MPa and 70 GPa, respectively [45, 60, 61]. The existence and role of water in the structure of nacre has been investigated by many researchers. It has been mentioned that the effect of water was to increase the ductility of nacre and increase the toughness by almost tenfold [62, 63].

Wang et al. (2001), performed a study investigating the behavior of abalone nacre and pearl oyster nacre under different test setups. The results of four-point bending tests show a Young's modulus of $E \sim 70$ GPa. The tensile curves are highly nonlinear and the yield stress is in the range of 105-140 MPa [18]. Other researchers have described the origin of toughness by crack deflection, fiber pull-out and organic matrix bridging [52, 64]. Barthelat et al. (2006 and 2007) also performed a numerical and experimental investigation on deformation and fracture of nacre and proposed their results from image correlation, finding the experimental crack resistance curves for nacre with logarithmic function fit [65]. They claimed that the large breaking strain in the experiments and simulations was due to the waviness of the platelets. However, the numerical model based on the waviness of the platelets over predicts the strength and under predicts the ductility [66]. Li et al. (2004) studied the nano-scale structure of red abalone shell and suggested that the tablets themselves are made of nano-grains [8]. They found that although the tablet strength does not directly affect the deformation mechanism, the integrity of the tablets is due to these nano-grains which prevent the tablets from breaking during the deformation process. Nano-indentation was used by other research groups to study the properties of the individual components of nacre [67]. These studies emphasize that the platelets possess a high fracture stress, i.e. they will remain intact in the deformation process of nacre under low strain rates.

Many researchers believe that the organic matrix in the structure of nacre plays the key role in its high fracture toughness [58]. There has therefore been a great interest in understanding the mechanical behavior of the organic matrix. Smith et al. (1999) believe that the natural adhesives elongate in a stepwise manner. They claimed that opening of the organic macromolecules' folded domains cause a modular elongation and is the origin of toughness in the natural fibers and adhesives. In that study, a single molecule of protein was pulled and the behavior of a short molecule and long molecule was investigated. It was mentioned that the short molecules behave more stiffly but

required less energy to break [68]. In another study, Mohanty et al. (2008) investigated the mechanical response of the organic matrix of nacre. Atomic Force Microscopy (AFM) was used to pull the organic phase away from the aragonite. The results show a high adhesion force between the proteins and the platelets and are evidence of organic-inorganic interactions [69]. Different experimental approaches have been used to determine the mechanical properties of the organic matrix in different stages of deformation [70]-[74].

Molecular dynamics simulations have also been used to investigate the role of the organic matrix on the mechanical response of nacre [75]-[77]. In one study, done by Ghosh et al. (2007), the mechanical response of the organic matrix in proximity of aragonite platelets was investigated and it was indicated that the high elastic modulus of the proteins may be due to the mineral-organic interactions. Barthelat et al. (2006) used a two-dimensional finite element model of indentation to fit the experimental nano-indentation load-penetration depth curves of nacre, giving an elastic modulus of around 2.84 GPa [66]. Xu et al. (2011) considered the extension of a single biopolymer molecule as a series of helical springs, so that, unfolding of one module increases the stiffness of the biopolymer molecule. In that study, it was shown that a larger spring outer diameter causes a smaller spring constant [78]. Overall, these studies showed that the organic matrix has a high elastic modulus in the range of 4.0 GPa, while unfolding the entangled domains increases its stiffness during the deformation process.

Schaffer et al. (1997) claimed that abalone nacre forms by growth through mineral bridges rather than on heteroepitaxial nucleation [79], and many researchers have confirmed this [77, 80, 81]. Song et al. (2003) were the first to consider the role of pillars (mineral bridges) in enhancing the strength of the structure [82]. They believe that the mineral bridges between the tablets increase the fracture strength of the organic matrix interface by a factor of 5. It was also shown that the cracks propagate along the organic matrix. Their Transmission Electron Microscopy (TEM) images showed that the average length of the cracks in each of the organic layers is about 2 μm, and this is because of the crack deflection due to the presence of mineral bridges in the biomaterial. In another study, Song et al. (2003) studied the properties and performance of the organic matrix and mineral bridges in nacre's structure [83]. In that study, it was shown that the microstructure of nacre should be referred to as "brick-bridge-mortar" structure. Cartwright et al. (2007) also studied the dynamics of nacre self-assembly which indicates the presence of the shear mineral bridges between the platelets in the nacre of gastropods

[84]. Their observations show that the mineral tablets start growing through pores in the membrane and initiate the tablet above. They also pointed out how the pore size may influence the rate of growth of mineral bridges (incomplete growth will create asperities on the surface of the platelets). Similar crystalline orientation of platelets in different layers has been shown as strong evidence of the existence of mineral bridges and of a self-assembly mechanism in nacre [85, 86, 87]. Checa et al. (2011) also used high-resolution imaging techniques to prove the existence of shear mineral bridges and asperities between the layers of platelets in the nacre of gastropods [88]. Furthermore, as Ghosh et al. (2007) pointed out, the organic matrix behaves more stiffly in proximity of the minerals [75]. Hence, the existence of pillars and asperities affect the mechanical properties of nacre through two mechanisms: a) directly, by inclusion of their own properties, and b) indirectly, by stiffening the organic matrix.

Beside experimentations and observations, there are different numerical and theoretical approaches to model the mechanical response of nacre [89]-[95]. Katti and Katti (2001) numerically modeled the mechanical behavior of nacre with an elastic 3D finite element model based on brick and mortar microstructure, assuming the organic matrix behaves linearly [96, 97]. The results show that the organic layer needs to have a high modulus in order to capture the experimental results on nacre. Evans et al. (2001) constructed a model consisting of platelets and asperities with a frictionless interface [98]. Their results show that the nano-scale asperities provide a strain-hardening large enough to ensure the formation of multiple dilatation bands but not so large that platelets fracture internally. Shao et al. (2012) also studied the size effect on the mechanical response of nacre, and proposed a discontinuous crack-bridging model for fracture toughness analysis of nacre [99]. The effect of pre-existing structural defects was investigated in the crack-bridging based model in another study by Shao et al. (2014) [100]. More recently, Begley et al. (2012) [101] studied the brick and mortar structure and proposed a model to guide the development of these composites. In that study, the uniaxial response of the brick and mortar composites was analyzed and the role of different parameters such as the bricks' aspect ratio and the volume percentage of the mortar part were investigated. The proposed analytical model by Begley et al. (2012) [101] is used here to validate some of the results.

In this chapter, we propose a micromechanics-based model to investigate the role of platelets, mineral bridges (pillars), nano-scale asperities and the

organic matrix in the overall deformation mechanism of nacre. The main and new hypotheses in our numerical model are that 1) the nano-scale pillars have near theoretical strength; and 2) the existence of these nano-scale features confine the organic matrix to the proximity of mineral platelets and hence, increase their otherwise low stiffness.

2.2 The Micromechanical Model

2.2.1 Nacreous structure

A detailed investigation on the microstructure of nacre reveals that the structure of abalone nacre is more than a mortar-brick repeating unit as shown in the increasing scale image, Figure 2.1. Nano-asperities, proteins (organic matrix) and mineral pillars (previously referred to as mineral bridges) fill inside the inter-layers and gaps. The statistical studies on abalone nacre illustrate that the average length of one platelet on the cross section is approximately equal to 4.0 μm and the aspect ratio of the platelets are generally around 8.0 [83] measured as L/D, where L is the length of the platelets and D is the thickness. The pillars are placed in the gap between two layers, normal to the longitudinal side of the platelets.

2.2.2 Finite element models

Aragonite platelets were modeled as beam elements with a bending stiffness set to represent the flexural behavior of hexagonal platelets with $E_{tab} = 100$ GPa, although they carry minimal bending stresses. The length of a single platelet was considered to be about 4.0 μm and its thickness was estimated to be about 0.52 μm. The inter-layer gap was 24 nm and the gap between two adjacent platelets in a layer was estimated as 20 nm. The density of the platelets was set to be around 3 gr/cm^3. ABAQUS/Explicit software package was used to carry out the finite element simulations.

The fundamental assumption in this model is that the strength of mineral bridges is equal to their *theoretical strength* $= \sigma \sim E/30$, since the gap between the platelets is less than the critical length scale (30 nm) [92]. Hence pillars were modeled as link elements with stiffness equal to the shear modulus of aragonite $E_{pillars} = G_{tab} = 40.0$ GPa and $\sigma_{pillars} = 3.3$ GPa. The area fraction of pillars, β_1, was estimated to be about 1.0-4.0 %. Moreover, since

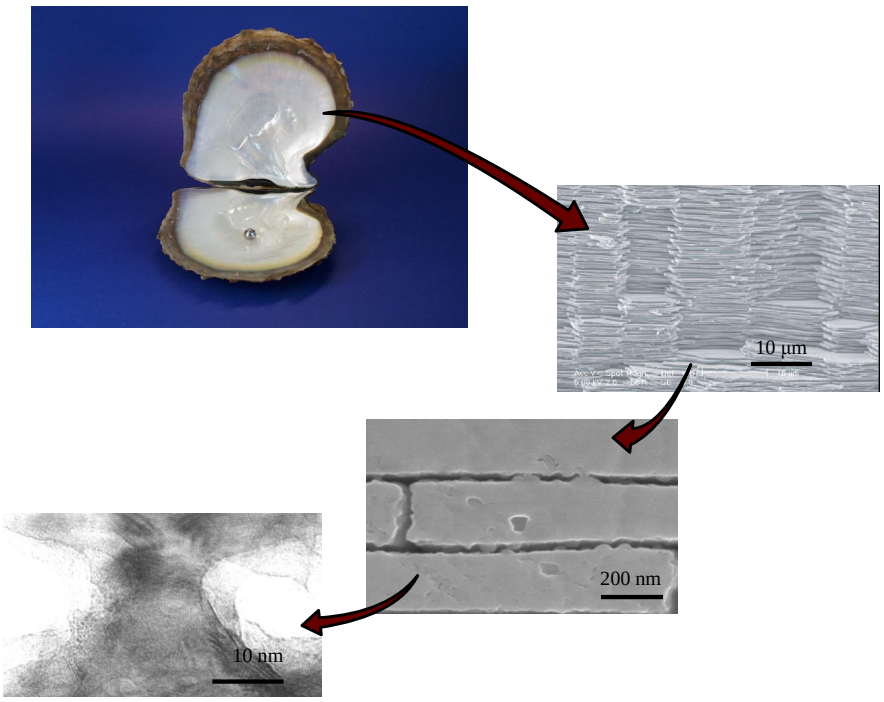

Figure 2.1: Scanning Electron Microscopy (SEM) images of the microstructure of nacre [18]

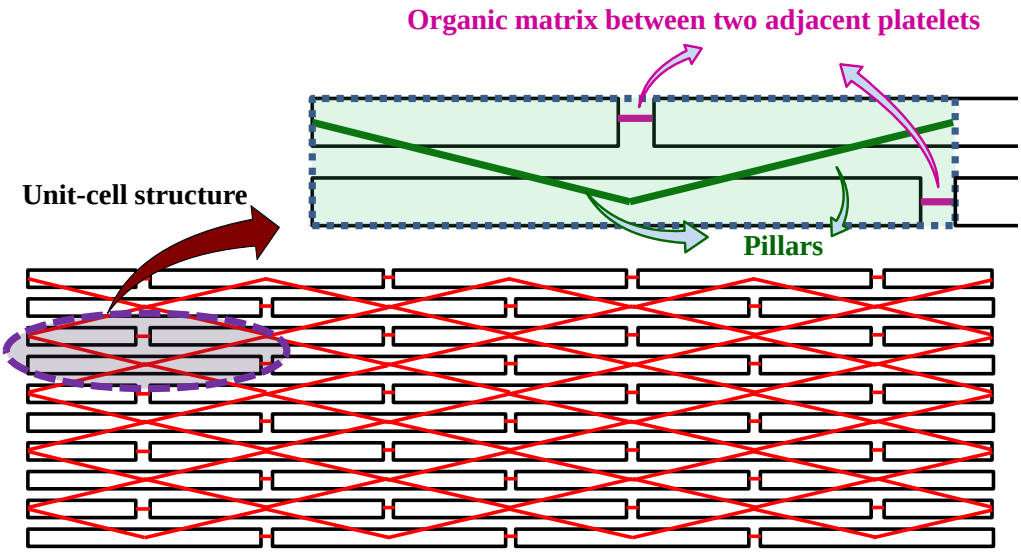

Figure 2.2: Schematic of the arrangement of the link elements representing the organic matrix, pillars and asperities in the model

the density of the pillars in the central region of the platelets is higher than the density of pillars in the outer region of platelets [83], in our model, the pillars modeled as link elements connecting the middle of the platelets in two adjacent rows in each unit-cell, Figure 2.2.

In the proposed model, the behavior of proteins is approximated to be linear elastic before failure. We believe that pillars and asperities confine the organic layer in between the aragonite platelets. This results in a high stiffness value for the organic matrix in the range of ~ 4.0 GPa. The organic matrix's strength is considered to be near theoretical strength of ~ 200 MPa. The organic matrix in-between the two neighboring platelets was modeled as link elements connecting the edges of the platelets, Figure 2.2.

It has been previously shown that the asperities in different layers interpose in many spots. This interlocking affects nacre's behavior by involving more short molecules and making the organic matrix behave [97]. The nano-asperities in-between two adjacent platelets provides confinement and entanglement of short molecules in the organic matrix in the proximity of mineral platelets. This is the physical mechanism that provides the high stiffness of the organic matrix. Observations also show nano-scale mineral islands are

about 30-100 nm in diameter and 10 nm in amplitude. Nano-asperities show a statistical distribution with average spacing of 60-120 nm. [18]. Accordingly, the area fraction of the asperities, β_2, was estimated to be about 40.0 %. Hence, the asperities were modeled as link elements to reflect the effects of the interactions of the organic matrix with platelets. This element fails when the displacement between the two platelets in adjacent layers reaches to the point of no-interaction between the organic matrix and the platelet, which is when the stress in the organic matrix reaches its strength limit. The asperities are modeled as link elements with stiffness equal to the shear modulus of the organic matrix, $E_{asperities} = 1.6$ GPa, and the strength of about 200 MPa.

The mechanical behavior of each element in the structure of nacre is shown in Figure 2.3. Using the material properties, geometry, and area fraction of the components, a unit-cell model was created. Displacement was applied in equal time steps to the right hand side of the system, while the left hand side of the unit-cell was fixed in the X direction. Figure 2.2 shows a schematic of the unit-cell structure and the way the link elements are arranged to capture the mechanical response of the proposed components. In this system, each element is guaranteed to behave in its natural state, e.g. pillars are modeled as link elements in the direction parallel to the platelets, which translates into shear behavior with no bending.

The unit-cell was used to model the deformation mechanism in a super-cell representing the multilayered structure of nacre. The super-cell was composed of 10 elements in 20 layers for each simulation. Using symmetry, only a quarter of the sample was modeled under a four-point bending experiment. The four-point bending experiment was modeled by applying the linear displacement on the right hand side of the super-cell as shown in Figure 2.4. For a super-cell, average stress in the layers is plotted versus the average strain of the total cross-section.The simulations were performed for several multilayered models, using the mechanical properties and the prescribed area fractions.

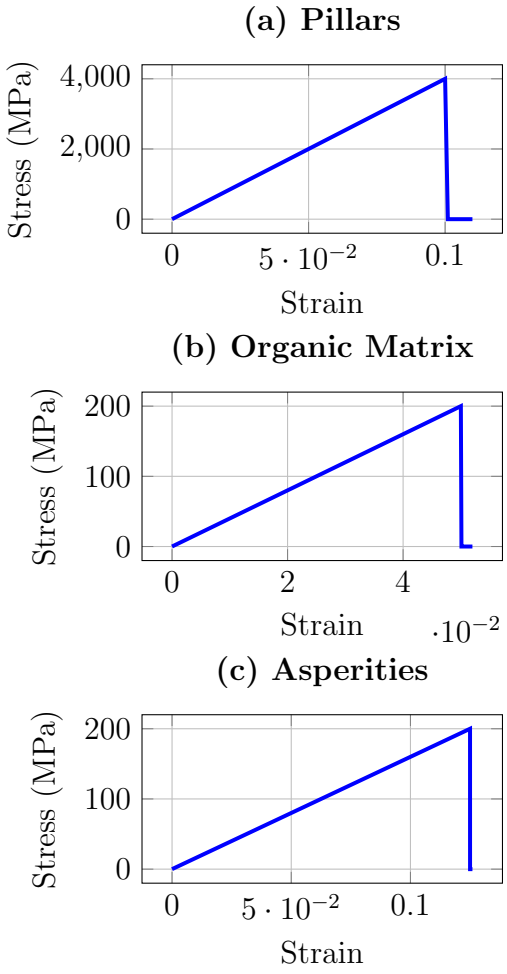

Figure 2.3: Stress-strain behavior of the components present in the unit-cell: (a) Pillars, (b) Organic matrix, (c) Asperities

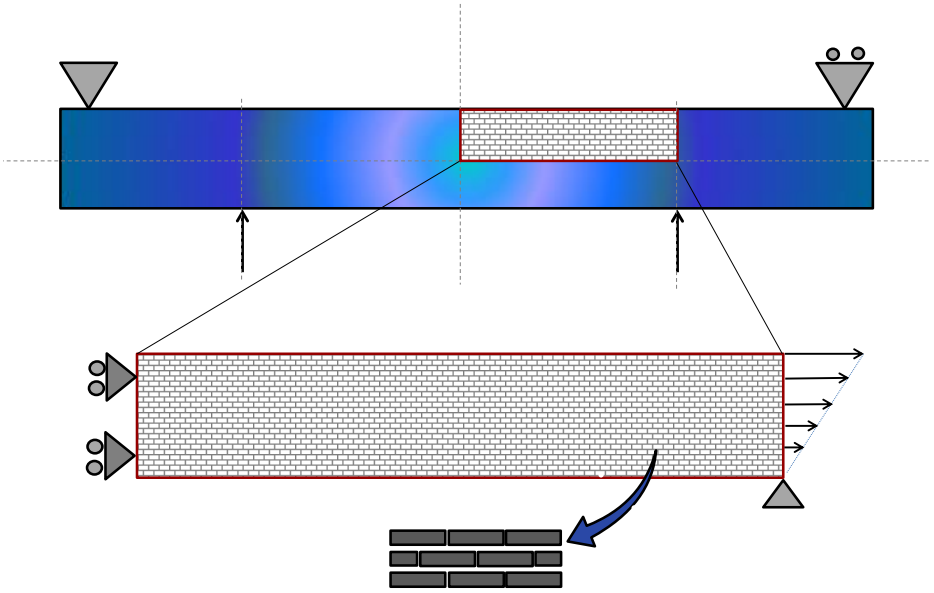

Figure 2.4: Schematic of model used for the simulation of the four-point bend experiment

2.3 Results

2.3.1 Unit-cell behavior and nacre micromechanical model

The simulation result for the mechanical behavior of the unit-cell is presented in Figure 2.5a. The structural components in the unit-cell are schematically presented in Figure 2.5b. All elements carry the load during the early stages of deformation until the stress in the organic matrix under tension in both layers exceeds their strength. Hence, all the elements synergistically contribute to the Young's modulus of the suggested unit-cell. The initial stiffness of the unit-cell with an organic matrix with stiffness value of 4.0 GPa, 40.0 % area fraction of asperities and 2.0 % of pillars is about $E = 78.8$ GPa. In the second stage of the loading phase, the pillars and the proteins in shear carry the load. At the end of this stage, pillars break as the stress reaches their strength, and the proteins are the only elements that carry the load. In the third stage, the stiffness of the system comes from asperities (effective organic matrix). The simulation ends with the failure of the asperity elements, which represents the point of no organic-inorganic interaction between the

proteins and the platelets due to the excessive displacement between the two parallel platelets with respect to each other.

The simulation result for a multilayered system similar to the microstructure of nacre is presented in Figure 2.6. Here, average stress in the layers is plotted versus the average strain. Stress averaging is done by dividing the summation of the forces in each layer by the total cross sectional area in every stage of deformation. The stress-strain curves are in agreement with the previous experimental results [98]. The experimental response of four-point bending test on nacre showed a stiffness of about 70 GPa and a large inelastic deformation area in the stress-strain curve. These values are similar to the simulation results for a model with 40.0 % area fraction of asperities, 2.0 % area fraction of pillars and an organic matrix with the stiffness of about 4.0 GPa. Additionally, the yield stress of 110 MPa and ultimate strength of 150 MPa is close to the experimentally resulted values of 105 MPa and 140 MPa, respectively. Progressive failures of the organic matrices, pillars and asperities make the model exhibit significant tensile toughness[1] and a large inelastic deformation. In nacre, tablets sliding spreads throughout the material, and each of the local extensions generated at local sliding zones add up and cause high strains measured at the macro-scale.

[1]In this paper *tensile toughness* is defined as area under the stress-strain curve.

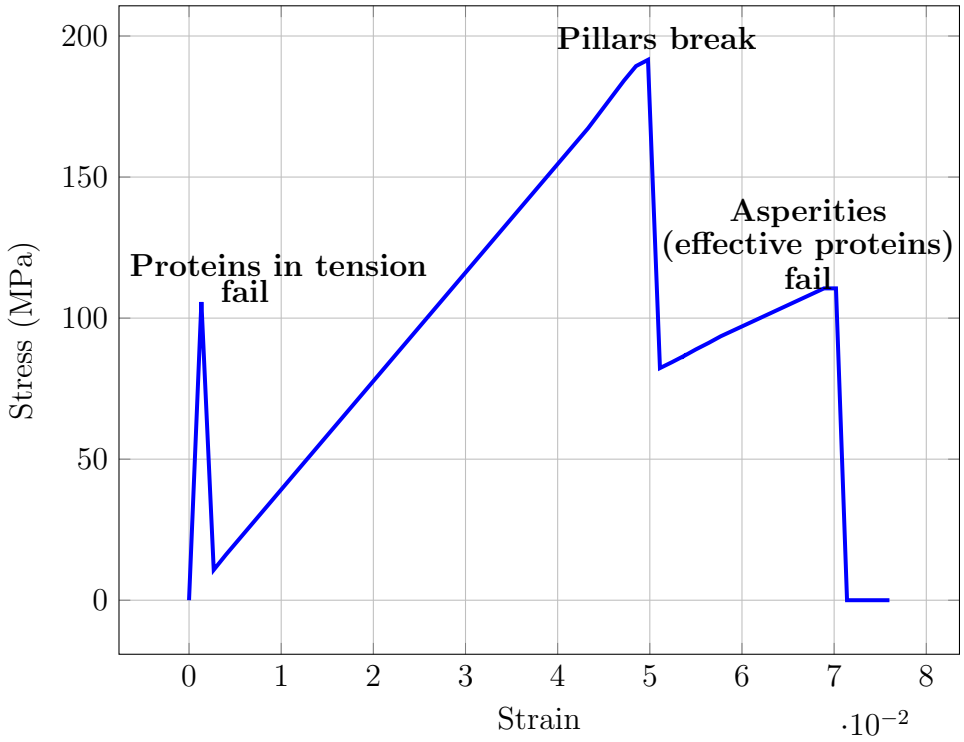

(a)

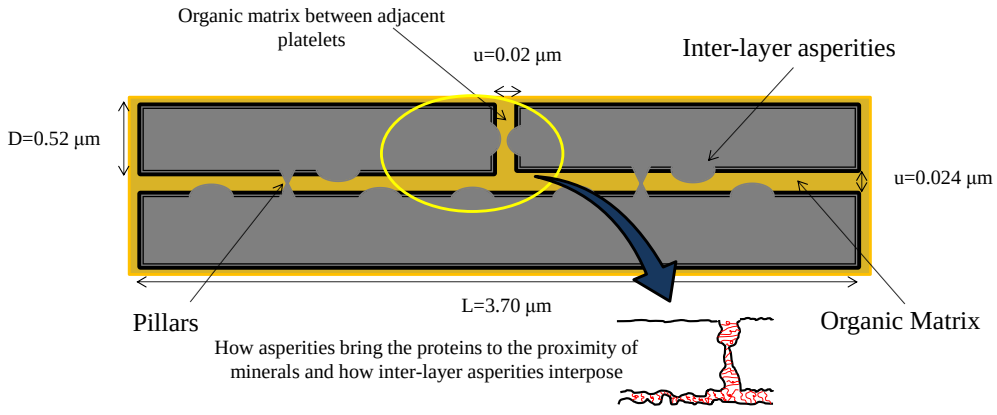

(b)

Figure 2.5: (a) Stress-strain plot of the suggested unit-cell, (b) Schematic graph of components in the unit-cell structure

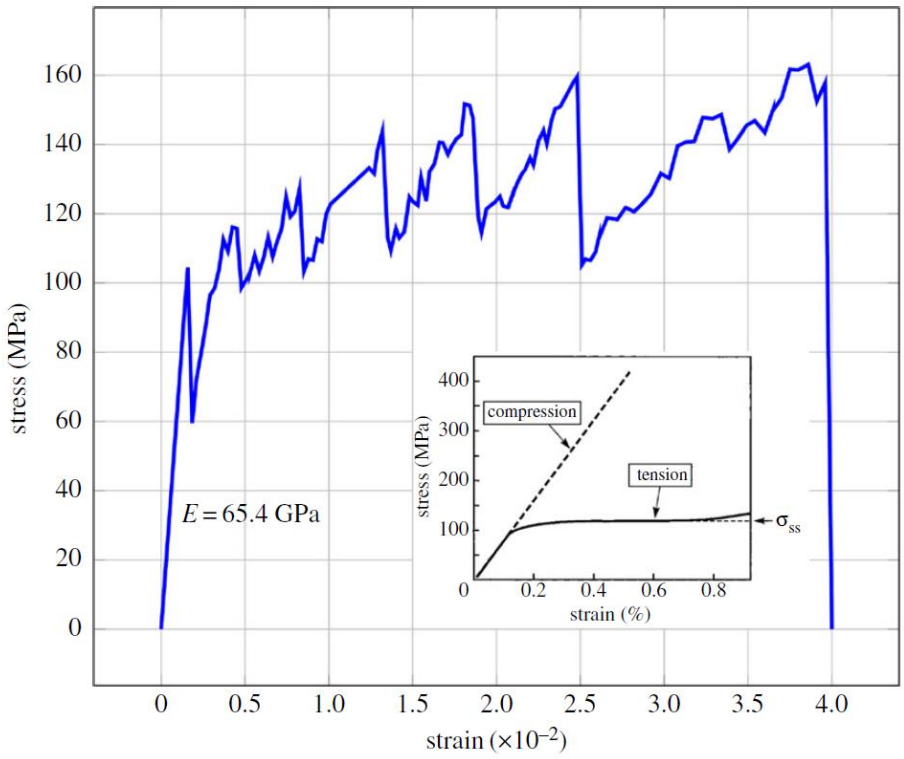

Figure 2.6: Nacre micromechanical model response (compared with the experimental results investigated by Evans et al. (2001) [98])

3

Mechanics of Nacre-inspired Ceramic/Polymer Composites

3.1 Introduction

It has been shown that layered structure and super-strong interface in nacre is the origin of high strength, stiffness and toughness [15, 102]. Nacre is a natural composite made of 95 % aragonite platelets and 5 % biological macromolecules. The organic phase is extremely important in nacre's fracture toughness [17, 16]. Previous research on nacre has shown that its layered brick and mortar structure is the origin of the remarkable mechanical properties [17]. The simple brick and mortar structure makes the material so much tougher than its constituents. Nacre's mechanical properties are strongly dependent on the nano-scale size of the components and hierarchy in its structure [103, 104, 105, 102]. One of the important nano-scale features discussed in the literature is the roughness of the tablets which is called "the asperities." For example, Evans et al. (2001) [98] constructed a model consisting of platelets and asperities. Their model calculates the stresses needed to displace the plates, resisted by elastic contacts at the asperities. All these studies can be a guide to design and fabricate man-made lamellar composites; however, more theoretical models are needed.

Layered structures can result in high toughness values if properly implemented [106]-[108]. Salehinia et al. (2014) studied the properties of multilayered ceramic/metal composites and investigated the effect of plastic deformation of metals in these materials [109]. There are several analytical studies

on the mechanics of multilayered materials [110]-[114]. An analytical model proposed by Jager and Fratzl (2000) [115] estimated the maximum stress and strain of the composite, by advancing previously established models of mineralized collagen fibrils [116]. A micromechanical model developed by Kotha et al. (2000) [117] derived axial and shear stress distributions in platelets on the assumption that the load carried by the platelets remains constant, and inter-platelet load transfer occurs by shear. Shuchun and Yueguang (2007) [118] used the classical shear-lag model to study the interdependence of the overall elastic modulus, and the number of hierarchical levels in bone-like materials, and compared their results against the Tension-Shear-Chain (TSC) model postulated by Gao et al. (2003) [92] and finite element simulations. Investigations by Chen et al. (2009) [119] were focused on understanding the characteristic length for efficient stress transfer in staggered biocomposites via derivation of an analytical model followed by numerical simulations. Wei et al. (2012) [120] laid down a criterion which reveals the existence of a unique overlap length in biological composites that contributes to an optimization of both strength and toughness. In a study by Begley et al. (2012) a micromechanical model is proposed for brick and mortar structure with elastic bricks and elastic perfectly plastic thin mortar layers [101]. This study was first to provide a map for designing tough, strong and stiff materials with brick and mortar structure.

The hierarchical structure is the main inspiration behind numerous attempts to design and fabricate multilayered micro and nanostructured materials [103, 121, 122, 123]. Various methods such as electrophoresis [124], dip coating [125], sol-gel [126], and deposition of mineral or clay platelets [127] have been developed to synthesize nacre-like structure. However, in all these methods the maximum size of the samples that can be fabricated is around several microns which is not practical for mechanical applications [128]. Freeze casting proves to be one of the most effective approaches to overcome this limitation where bioinspired multilayered composites are made in larger scales [129, 130, 131]. A porous bone-like ceramic was the first structural material made using freeze casting method [132]. The cooling rate and the solution concentration play important roles in improving the mechanical response of these scaffolds [133, 134]. Ceramic/polymer and ceramic/metal composites were the first bioinspired composite materials made by freeze casting method [134, 51]. However, the effect of the structure on the toughness and the toughening mechanisms and the role of the components were not fully understood. The main goal of this study is to explain the basic de-

formation, strengthening and toughening mechanism and the resulting stress distributions in multilayered materials. The microscale layers and nanoscale features in the samples made by freeze casting and investigating their mechanics distinguish our study from others.

In this paper, we have also focused on the toughness of multilayered lamellar structures.The effect of lamella thickness on mechanical performance, especially toughness of the materials was investigated experimentally and theoretically. The effect of material's architecture, which can be controlled in freeze casting, on the crack-resisting curve of samples, was also studied. Moreover, the effect of mortar properties was assessed by making lamellar composites with different matrix constituents. Furthermore, the importance of imperfect interface in man-made samples particularly samples made by freeze casting technique was investigated. The results of this study can be used as a guide to optimize the mechanics of bioinspired lamellar and brick and mortar materials.

3.2 Materials and Method

3.2.1 Experimental Procedure

The cumbersome freeze casting technique, broadly described as the templating of porous ceramic scaffolds by solidification of a solvent, was used in this study to create the multilayered ceramic/polymer composites. A directional freezing machine with controllable temperature and cooling rate was built, and used to fabricate the porous lamellar structured ceramic samples. All the steps such as the slurry preparation, controlled solidification of the slurry, sublimation of the solvent and densification of the green body or sintering, play important roles in the final structure of the ceramic scaffold and, therefore, mechanical performance of the composites. Hence, in this study, role of solidification rate is explored.

Lamellar alumina scaffolds were prepared by freeze casting of water-based suspensions. The suspensions (solid content 40 wt.%) were prepared by dispersing alumina powders with an average diameter of about 150 nm (nano α-Al_2O_3 powder, 99.85%, 40 nm grain size, Inframat Advanced Materials) in deionized water. An ammonium polymethacrylate anionic dispersant (Dar van CN, R.T. Vanderbilt Co., Norwalk, CT, 1.2 wt.% of the powder) and an organic binder (polyvinyl alcohol, 1.2 wt.% of the powder) were then added to achieve a uniform powder dispersion, and to ensure the integrity of the ceramic structure after removal of the ice. The suspensions were then poured into a cylindrical Teflon mold (25 mm in diameter, 50 mm in height), placing on a copper cold finger. The temperature of this cold finger was monitored with a temperature sensor. A ring heater and cold bath connected to a liquid nitrogen tank were used to manipulate the temperature of the slurry (Fig. 3.1). In order to obtain parallel ceramic lamella aligned over macroscopic dimensions (centimeters), the copper surface, where the ice nucleates, was scratched with a silicon carbide paper and a small vibration was applied to the mold during freezing.

The cold finger was then cooled down to -130 °C with a cooling rate varying between 1 and 25 °C/min. Later, the frozen ice/alumina samples were freeze-dried in order to remove the ice from the structure. Afterwards, the sensitive porous Alumina scaffolds were sintered at 1500 °C for 2 hours to densify the ceramic lamella. This resulted in a bulk ceramic porous scaffold, several centimeters in size with macroscopically oriented dense lamellar structure. PDMS and PU were infiltrated into the porous sintered scaffold

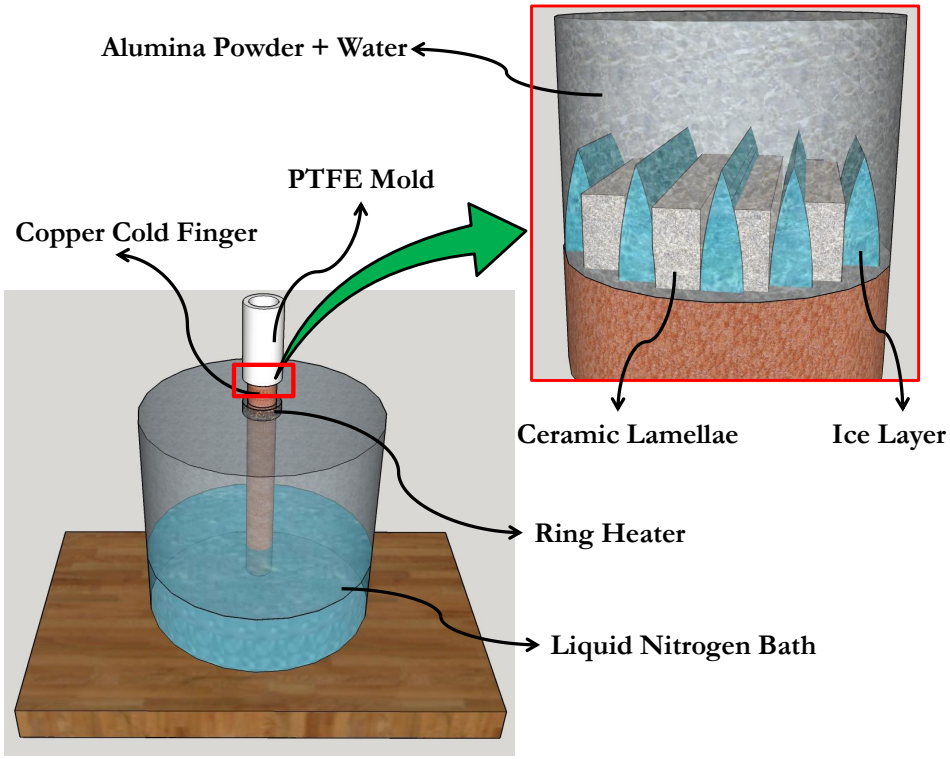

Figure 3.1: Schematic of the freeze casting method used to make samples with microstructures

to create the ceramic/polymer composites and study the role of different parameters and the resulting mechanical properties. Finally, vacuum and vibration were applied to soak the polymer into the structure and fill all the gaps and holes. Table 3.1 presents the mechanical properties of constituent materials used to make the samples.

Table 3.1: Mechanical properties of constituent materials

Material	Elastic Modulus (MPa)	Strength (MPa)
Alumina	50,000	150
PDMS	5	20 [135]
PU	300	50 [136]

Tensile Testing

The mechanics of the lamellar structured ceramic/polymer composites made by freeze casting method have not been fully explored in the past. We studied the mechanical properties of these samples using tensile tests. Dog-bone samples according to ASTM standard D638 were made and tested using an Instron 8548 microtester (Instron, Norwood, MA, USA).

Single-edge notch bending test

We have also investigated the fracture toughness of these samples with dimensions of 22 mm long, 4 mm thick and 8 mm wide. To perform a single-edge-notch bending experiment, a notch of 0.3 mm depth was created on the samples. The three-point bending test setup was used to perform the experiment. The loading rate of 1 mm/min was used for the experimental procedure. A Canon EOS 600D camera was used to track the crack growth during the experiment as the load was applied and increased on the samples. The recorded raw data were used to calculate the fracture toughness and energy release rate of the composite samples. Energy release rate, J was calculated from the applied load and instantaneous crack length according to ASTM Standard E1820-06 [137], and was decomposed into elastic and plastic contributions:

$$J = J_{el} + J_{pl}. \tag{3.1}$$

The elastic contribution J_{el} is based on linear elastic fracture mechanics:

$$J_{el} = \frac{K^2}{\bar{E}} \tag{3.2}$$

where K is the stress-intensity factor and $\bar{E}$ is the plane strain Young's modulus,

$$\bar{E} = \frac{E}{1-\nu^2} \tag{3.3}$$

where ν is Poisson's ratio. The plastic component J_{pl} is given by:

$$J_{pl} = \frac{2A_{pl}}{Ba'} \tag{3.4}$$

where A_{pl} is the plastic area under force vs. displacement curve, B is the specimen thickness and a' is the uncracked ligament length $(W - a)$.

3.2.2 The micromechanical model

Interlayer, shear-lag analysis A micromechanical model was also developed to predict the mechanical properties and guide the design of the lamellar structured composites. In order to discuss the effective properties of a multilayered composite, the balance of forces for the components of the unit-cell, followed by periodic boundary condition should be considered. Hence, the well-known shear-lag theory was employed on a simplified two-dimensional unit-cell of the multilayered composite [138, 139]. The previously developed shear-lag models for the layered composites contain several approximations. One of the important simplifications in these models is the assumption of decoupling the x and y directions in the in-plane shear stress, τ_{xy}. This decoupling permits 2-D planar elasticity problems to be simplified to a 1-D analysis. The in-plane shear stress following infinitesimal theory of deformation is defined as:

$$\tau_{xy} = G_{xy}\Big(\frac{\partial v}{\partial x} + \frac{\partial u}{\partial y}\Big) \tag{3.5}$$

where v is displacement in the y direction, u is the displacement in the x direction and G_{xy} is in-plane shear modulus. Hence, considering the layers of composite lying down in x direction, the fundamental assumption common to all planar, shear-lag analyses is that:

$$\frac{\partial v}{\partial x} = 0 \Longrightarrow \tau_{xy} \propto \frac{\partial u}{\partial y}. \tag{3.6}$$

Unidirectional composites can be considered as a layered structure assuming significantly stiff fibers in between soft matrix interlayer. If it is assumed that there are n (an odd number) layers in the geometry while odd layer numbers are the matrix and the even layer numbers are the fibers, and assuming a linear interpolation between $\langle u^{(i+1)} \rangle$ and $\langle u^{(i-1)} \rangle$, the Hook's law can be written as:

$$\tau_{xy}^{(i)} = 0, \qquad i = 2m \tag{3.7}$$

$$\tau_{xy}^{(i)} = \frac{G_{xy}^{(i)}}{t_i}(\langle u^{(i+1)} \rangle - \langle u^{(i-1)} \rangle), \qquad i = 2m+1 \tag{3.8}$$

where m is an integer and $\langle * \rangle$ indicates averaging over the thickness of the layer and can be defined as:

$$\langle u^{(i)} \rangle = \frac{1}{t_i} \int_{y_{i-1}}^{y_i} u(x,y) dy \tag{3.9}$$

where u(y_i) and u(y_{i-1}) are the axial displacements on the two edges of layer i. Another relation between displacement and shear stress can be derived by using stress equilibrium and Hook's law. The stress equilibrium in layer i can be written as:

$$\frac{\partial \sigma_x^{(i)}}{\partial x} + \frac{\partial \tau_{xy}^{(i)}}{\partial y} = 0 \tag{3.10}$$

Integrating over the thickness leads to:

$$\frac{d(t_i \langle \sigma_x^{(i)} \rangle)}{dx} = \tau(y_{i-1}) - \tau(y_i) \tag{3.11}$$

Later, using the stress-strain relation in the x direction and differentiating with respect to x and averaging over the thickness we have:

$$\epsilon_x = \frac{\partial u}{\partial x} = \frac{\sigma_x}{E_x^{(i)}} - \frac{\nu_{xy}^{(i)} \sigma_y}{E_x^{(i)}} \tag{3.12}$$

$$\frac{d^2 \langle u^{(i)} \rangle}{d^2 x} = \frac{1}{t_i E_x^{(i)}} \frac{d(t_i \langle \sigma_x^{(i)} \rangle)}{dx} - \frac{\nu_{xy}^{(i)}}{E_y^{(i)}} \frac{d(\sigma_y^{(i)})}{dx} \tag{3.13}$$

where ν_{xy} is the Poisson's ratio. Another assumption in the shear lag theory is that in the Equation 3.13 the second term of the right side is much less than the first term. Hence, the simplifications lead to the following equation:

$$\frac{d^2\langle u^{(i)}\rangle}{d^2x} = \frac{\tau(y_{i-1}) - \tau(y_i)}{t_i E_x^{(i)}}. \tag{3.14}$$

Considering these calculations the shear-lag theory for lamellar structured stiff fibers and soft matrix with perfect interface can be summarized in the following equation:

$$\mathbf{A_T}\frac{d^2\tau_T}{d^2x} - \mathbf{B_T}\tau_T = -\tau_{I,0} \tag{3.15}$$

where $\mathbf{A_T}$ is an $\frac{(n-3)}{2} \times \frac{(n-3)}{2}$ diagonal matrix with the ith diagonal element being:

$$(A_T)_{i,i} = \frac{t_{2i+1}}{G_{xy}^{(2i+1)}} \tag{3.16}$$

and $\mathbf{B_T}$ is an $\frac{(n-3)}{2} \times \frac{(n-3)}{2}$ matrix with the following elements:

$$(B_T)_{i,i-1} = -\frac{1}{E_x^{(2i)}t_{2i}}, \quad (B_T)_{i,i} = \frac{1}{E_x^{2(i+1)}t_{2(i+1)}} + \frac{1}{E_x^{(2i)}t_{2i}}, \quad (B_T)_{i,i+1} = -\frac{1}{E_x^{2(i+1)}t_{2(i+1)}} \tag{3.17}$$

A transformation to an equation for average axial stresses in the stiff layers leads to the following expresion.

$$\frac{d^2P_T}{d^2x} - \mathbf{M_{I,\sigma}}P = -\mathbf{M_{I,\sigma}}P_{I,\infty} \tag{3.18}$$

where P is the vector of forces per unit plate depth on the layers, and can be defined as:

$$P = (t_1\langle\sigma_x^{(1)}\rangle,\ t_2\langle\sigma_x^{(2)}\rangle,\ ...,\ t_{n-1}\langle\sigma_x^{(n-1)}\rangle). \tag{3.19}$$

Now, if we assume that the layers with even numbers are the stiff layers, then the force vector per unit plate depth, P_T, on these layers is defined as:

$$P_T = (t_2\langle\sigma_x^{(2)}\rangle,\ t_4\langle\sigma_x^{(4)}\rangle,\ ...,\ t_{n-3}\langle\sigma_x^{(n-3)}\rangle) \tag{3.20}$$

$P_{I,\infty}$ is the far field or steady state tensile stresses in each layer when there are no shear stress boundary conditions; in other words, the tensile forces in the layers under constant axial stress far away from any ends, discontinuities or breaks in any layers. Hence, it can be defined as:

$$(P_{I,\infty})_i = t_{2i} E_x^{(2i)} \left(\frac{(\tau_{xy}^{(1)} - \tau_{xy}^{(n)})x + t_T \sigma_0(0)}{t_T E_{I,x}^0} \right) \tag{3.21}$$

where $t_T = \sum_{n=2,4}^{n-1} t_i$ and $E_{I,x}^0 = \frac{1}{t_T} \sum_{n=2,4}^{n-1} E_x^{(i)} t_i$ that is the contribution of the stiff layers and $\sigma_0(0)$ is the total applied stress in the x direction when x=0. Moreover, as presented in [140], $[M_{I,\sigma}] = [I_L]^{-1}[A_T]^{-1}[B_T][I_L]$.
where $[I_L]$ is an $(n-1) \times (n-1)$ matrix with 1 on the diagonal and in lower half of the matrix zero elsewhere. Hence the elements of $[I_L]^{-1}$ are: $[I_L]^{-1}_{i,j} = 1$ if $i = j$, $[I_L]^{-1}_{i,j} = -1$ if $j = i - 1$, otherwise $[I_L]^{-1}_{i,j} = 0$. Assuming that the fibers are all same in thickness and properties and the matrix layers have the same thickness and properties, $[M_{I,\sigma}]$ summarizes to:

$$\mathbf{M_{I,\sigma}} = \frac{G_m}{E_b t_b t_m} \begin{pmatrix} 1 & -1 & 0 & 0 & ... \\ -1 & 2 & -1 & 0 & ... \\ 0 & -1 & 2 & -1 & ... \\ & & \downarrow & & \\ ... & -1 & 2 & -1 & 0 \\ ... & 0 & -1 & 2 & -1 \\ ... & 0 & 0 & -1 & 1 \end{pmatrix}$$

Here we assumed an idealized composite geometry that is schematically presented in Fig. 3.2. The wallpaper symmetry group is pmm, with two bricks per unit cell, which are separated by one brick height vertically, and shifted by a distance of s horizontally. The mortar thickness between adjacent plates in each layer (vertical mortar) is assumed to be small in comparison to the brick dimensions. It assumed that the components deform only in the x-direction (the arrangement of the bricks in the through-thickness direction does not factor into the response).
For the assumed geometry, $\mathbf{M_{I,\sigma}}$ would be as following:

$$\mathbf{M_{I,\sigma}} = \frac{G_m}{E_b t_b t_m} \begin{pmatrix} 1 & -1 \\ -1 & 1 \end{pmatrix}$$

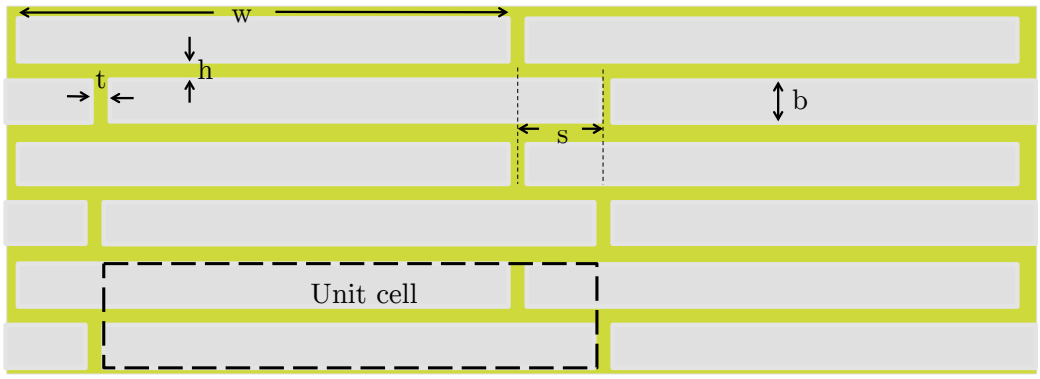

(a)

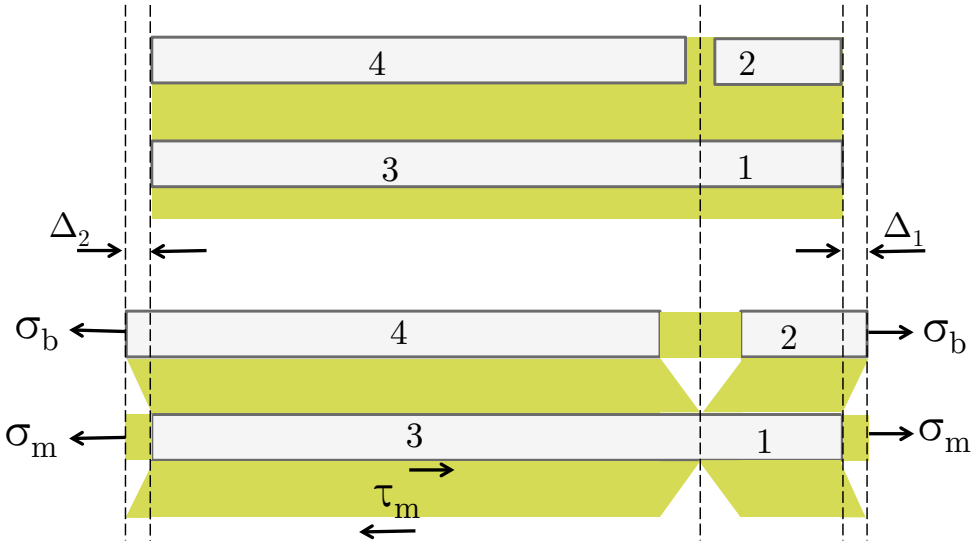

(b)

Figure 3.2: (a) Schematic of idealized super-cell structure and the length parameters (t= thickness of the vertical interface, h= thickness of the polymer layer, w= length of the bricks,b= thickness of the ceramic layers, s= overlap) (b) Unit-cell structure assumed to apply the shear-lag theory

In other words the matrix A_T in Eq. 3.16 will be summarized in one term only as $A_T = \frac{t}{G}$. Hence, this notation leads to the following complete set of governing equations:

$$u_1{}'' = \frac{G_m}{E_b hb}(u_1 - u_2) \longrightarrow 0 < x < s \tag{3.22}$$

$$u_2{}'' = \frac{G_m}{E_b hb}(u_2 - u_1) \longrightarrow 0 < x < s \tag{3.23}$$

$$u_3{}'' = \frac{G_m}{E_b hb}(u_3 - u_4) \longrightarrow -(w - s) < x < 0 \tag{3.24}$$

$$u_4{}'' = \frac{G_m}{E_b hb}(u_4 - u_3) \longrightarrow -(w - s) < x < 0 \tag{3.25}$$

The corresponding boundary conditions can be written as the followings:

$$u_1(0) = u_3(0) = 0 \tag{3.26}$$

$$u_2(s) = \Delta \tag{3.27}$$

$$u_2(s) - u_3(s - w) = \epsilon.w \tag{3.28}$$

$$u_3{}'(0) = u_2{}'(0) = \alpha[u_2(0) - u_3(0)] \tag{3.29}$$

$$u_1{}'(s) = u_3{}'(s - w) = 0 \tag{3.30}$$

$$u_1{}'(0) = u_2{}'(s) = u_3{}'(s - w), \tag{3.31}$$

where $\alpha = \frac{E_m}{E_b t}$. Using these boundary conditions the displacement of the different parts of model, u_1, u_2, u_3 and u_4 were calculated.

Effect of Imperfect Interface The quality of the interface plays an important role on the overall mechanical properties of composites [141]-[147]. In perfectly bonded interfaces, tractions and displacements are continuous across the interface. However, in many cases, the perfect interface assumption is not adequate. The classical approach to an imperfect interface is to relax interfacial continuity and allow a discontinuity in stresses and displacements at the interface [148]. In static loading conditions, stress equilibrium requires the stresses in the interface to be continuous regardless of the quality

of the interface. The remaining discontinuities in displacements are functions of interfacial stresses.

$$\begin{aligned} \sigma_{xx}^{(1)} &= \sigma_{xx}^{(2)} = D_n[u_x], \qquad [u_x] = u_x^{(2)} - u_x^{(4)} \\ \tau_{xy}^{(1)} &= \tau_{xy}^{(2)} = D_s[u_{xy}], \qquad [u_{xy}] = u_x^{(2)} - u_x^{(1)} \end{aligned} \tag{3.32}$$

where D_n and D_s are called interface parameters. The parameters represent the ability of the interphase to transfer stress. A perfect interface can be represented by $D_n = D_s = \infty$ which implies vanishing of displacement jumps, and a completely detached interface can be represented by $D_n = D_s = 0$. Intermediate values describe an imperfect interface.

In order to implement the effect of interface into the developed shear-lag models, Eq. 6.2 was modified as follows:

$$(A_T)_{i,i} = \frac{t_{2i+1}}{G_{xy}^{(2i+1)}} + \frac{1}{D_s^{(2i+1)}} \tag{3.33}$$

where D_s is the interface parameter, previously described. Using this new assumption, the governing equations were derived and solved.

3.3 Results and Discussion

3.3.1 Experiments: microstructure analysis, mechanical response and fracture properties of lamellar composites

The results show that changing the cooling rate changes the lamella thickness. During the process of preparing the samples, the temperature of the cold finger was monitored and manipulated by combining a cold bath with ring heaters. The cold finger was cooled to $-130\,^{\circ}\mathrm{C}$ with the cooling rate varying between 1 and $25\,^{\circ}\mathrm{C}$/min. Controlling the cooling rates under 3 $^{\circ}$C/min is challenging, and cooling rates above 20 $^{\circ}$C/min generally cause excessive vibrations in the machine. Fig. 3.3 shows an SEM image of a typical ceramic scaffold before polymer infiltration. The ceramic layers can be as thin as 4 μm and as thick as 20 μm, using the presented framework. Fig. 3.4 compares the different microstructures of the composite samples made with different

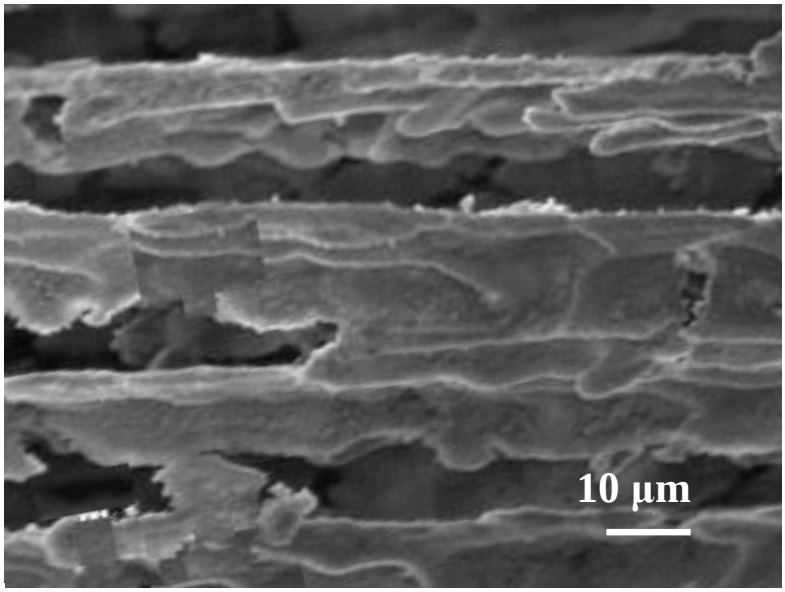

Figure 3.3: SEM image of a bioinspired ceramic scaffold with lamellar structure before polymer infiltration

cooling rates. It is clear from the images that increasing the cooling rate will decrease the lamella thickness.

An important feature in the structure of nacre that can be mimicked here, in the samples made by freeze casting method, is the asperities that appear on one side of each ceramic layer. Asperities play important role in enhancing the polymer/ceramic interfaces [102]. Fig. 3.5 shows the asperities in the structure of fabricated composites.

Fig. 3.6a compares the stress-strain curves obtained by tensile testing on Al_2O_3/PDMS samples. Four average lamella thicknesses are the result of four average cooling rates. The graphs show that there is a trade-off between strength and ductility of the samples. In these samples, as the lamella thickness decreases, the stiffness and strength increase and the ductility decreases. This is only true for the case of soft polymers, since the weak properties of the polymer causes a low state of stress after the vertical rupture.

Fig. 3.6b compares the stress-strain curves of Al_2O_3/PU samples made with different cooling rates. The graphs show that there is an optimum value for the strength. For small lamella thicknesses, the matrix causes the plates to fracture, however, for larger thicknesses, the plates tolerate the stress

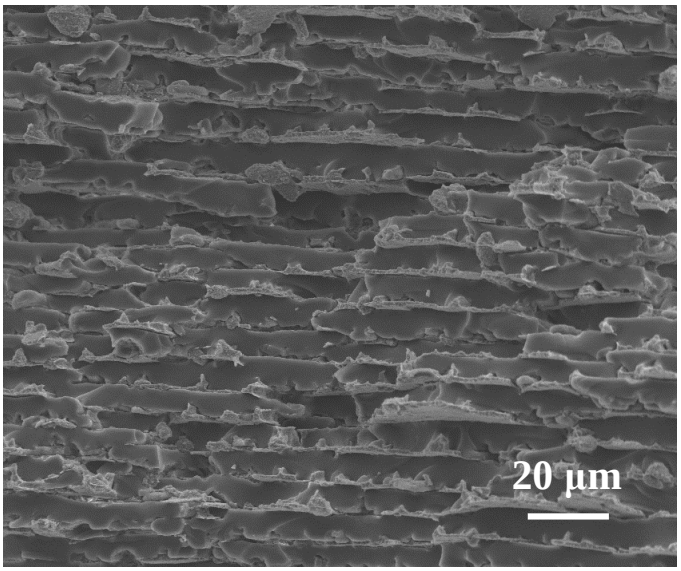

(a)

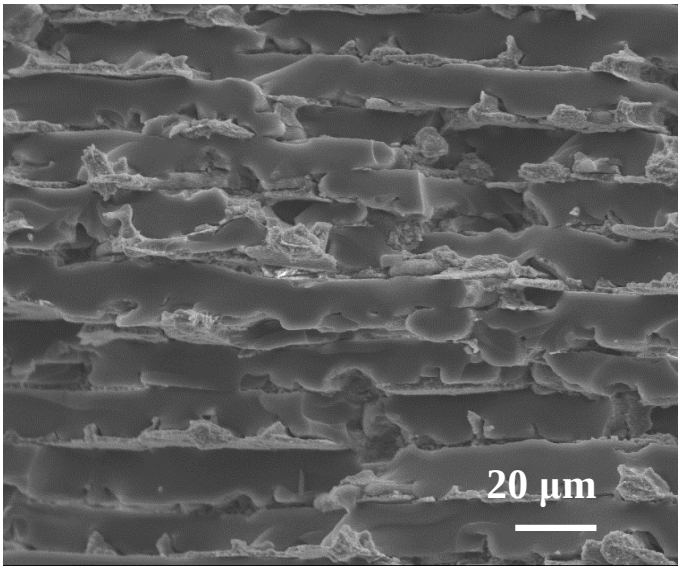

(b)

Figure 3.4: SEM image of (a) a lamellar structured composite with lamella thickness of about 4 μm fabricated with cooling rate of 20 °C/min, and (b) a lamellar structured composite with lamella thickness of about 11 μm fabricated with cooling rate of 5 °C/min

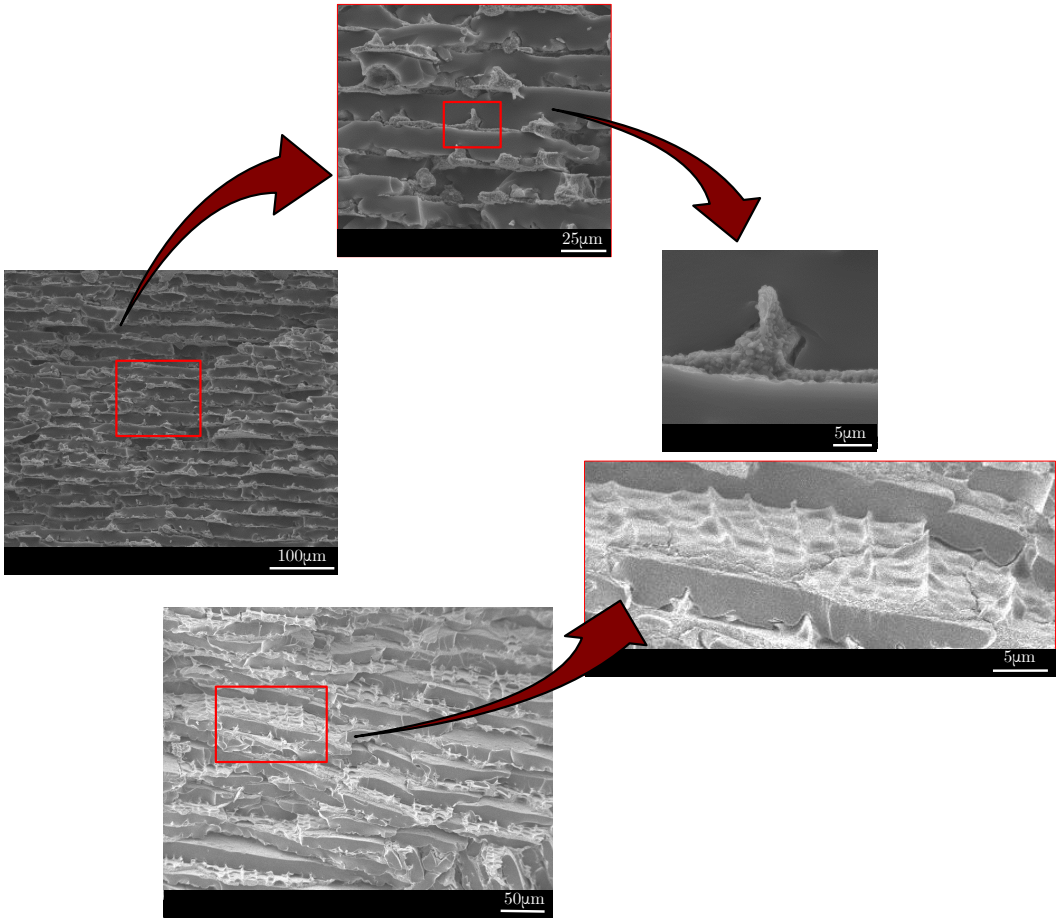

Figure 3.5: Presence of asperities in the structure of samples made by freeze casting play important roles in their mechanical properties.

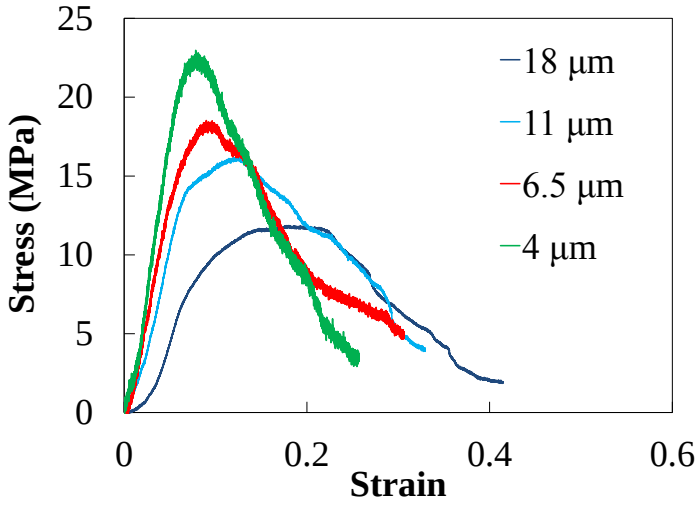

(a)

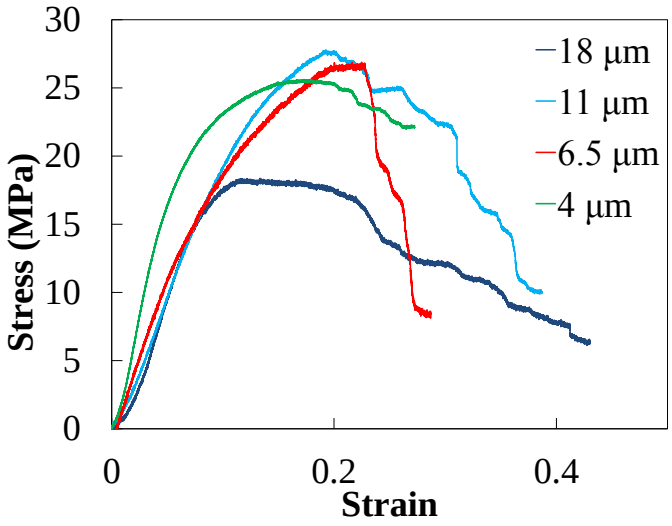

(b)

Figure 3.6: Stress-strain relationships for (a) Al_2O_3/PDMS and (b) Al_2O_3/PU samples as a function of lamella thicknesses

and the shear stress in the mortar determines the strength. For Al_2O_3/PU samples, the drop in the state of stress is lower, after vertical rupture, than the drop in the state of stress in Al_2O_3/PDMS samples. Comparing these data shows that the stiffness and ultimate strength of Al_2O_3/PU samples are higher than those of the Al_2O_3/PDMS samples. However, this is only due to the higher stiffness and strength of the PU in comparison to PDMS. The larger ultimate strains in samples is due to the fiber pull-out effect which is more pronounced in the samples with PDMS. The toughness and toughening mechanisms are extensively discussed in Section 3.3.

Single-edge-notch bending tests were performed on the samples and the stress at each crack length was used to find the R-Curve of the fabricated samples [149]. Fig. 3.7a and 3.7b compare the crack resistance curves for Al_2O_3/PDMS and Al_2O_3/PU samples made with different cooling rates, respectively. The influence of ceramic lamella thickness on fracture energy in these samples can be clearly observed in these results.

Fig. 3.7a demonstrates that the crack resistance increases as the crack grows in the samples with the larger lamella thicknesses, and this is due to the effective fiber (lamellae) pull-out mechanism that occurs toward the final stage of deformation. This toughening mechanism is less effective in samples with smaller lamella thickness. The same mechanism can be observed in the Al_2O_3/PU samples. However, as the matrix in this case is significantly stiffer than PDMS, the fiber pull-out mechanism is indeed less effective. Hence, the R-Curve of samples with small lamella thickness (4 μm) drops significantly. However, it must be noted that all composite samples fabricated here with lamella thicknesses of more than 4 μm outperform nacre with respect to fracture energy. The plane strain critical energy release rate (J_{I_C}) for samples with different lamella thickness and different matrix material is also presented in Fig. 3.8. The toughening mechanisms and related phenomena are extensively discussed in section 3.3.

3.3.2 Elastic modulus, strength and effect of imperfect interface

The volume fraction of the ceramic phase in the samples made by freeze casting can be assumed to be the same for all the samples since the alumina to water ratio is the same in all the initial solutions. Analytically, the prescribed shear-lag model was used to derive four second order differential equations

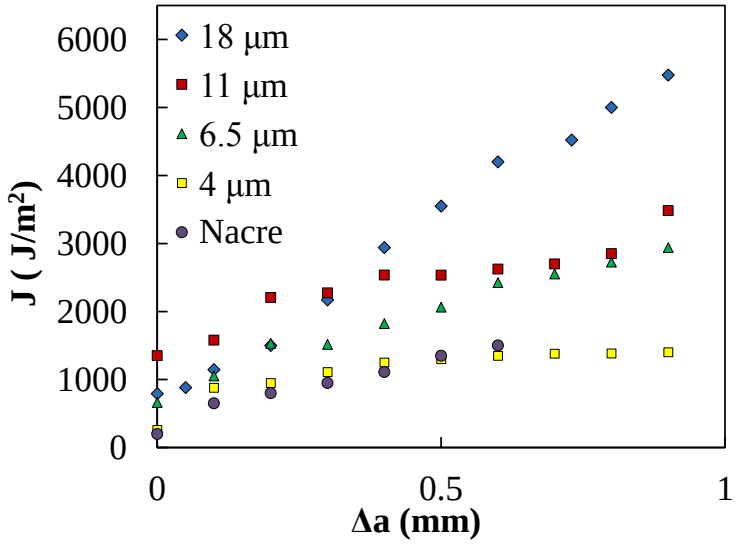

(a)

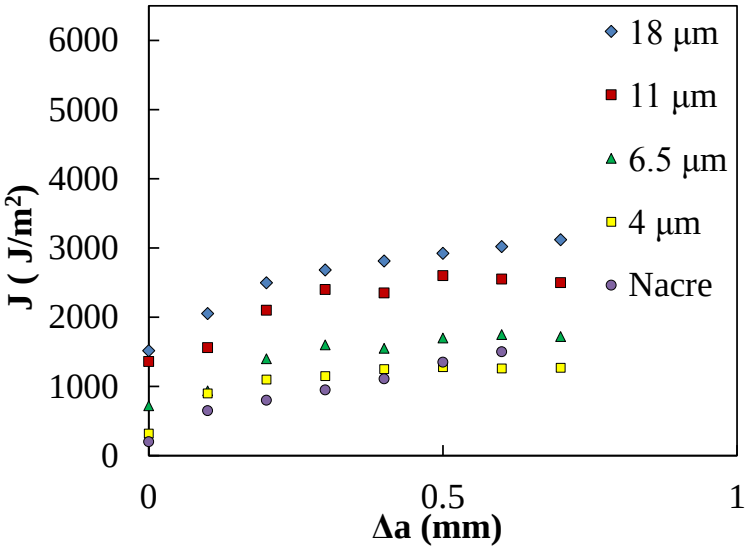

(b)

Figure 3.7: Crack resistance curves: Energy release rate as a function of crack growth in (a) Al_2O_3/PDMS samples, and (b) Al_2O_3/PU samples. For comparison, the nacre data is extracted from [150].

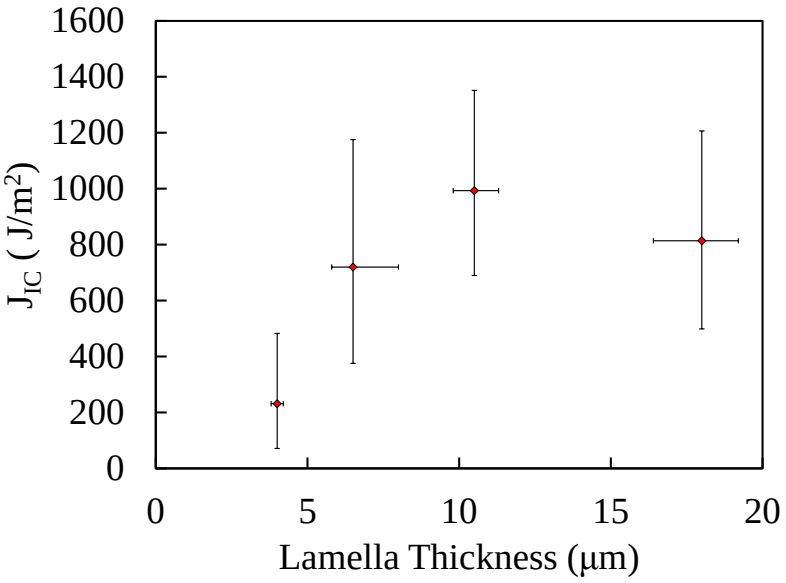

(a)

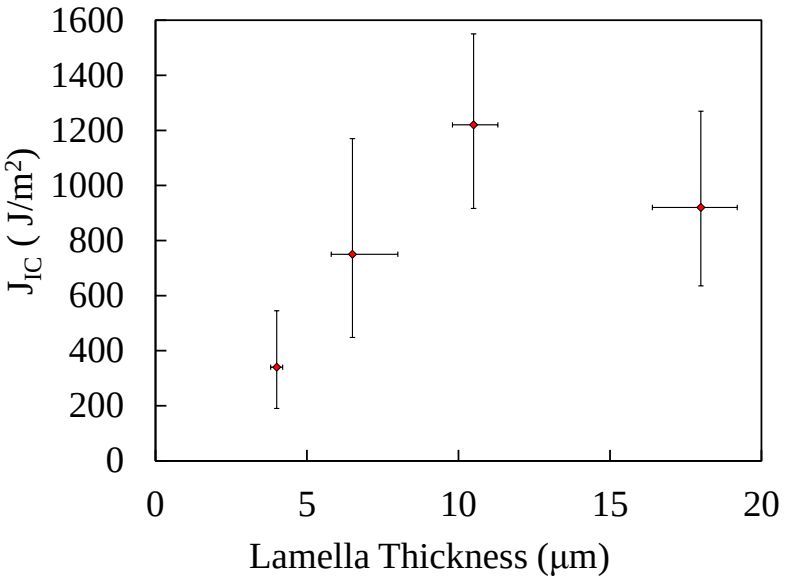

(b)

Figure 3.8: Plane strain critical energy release rate, G_c, as a function of lamella thickness in (a) Al_2O_3/PDMS samples, and (b) Al_2O_3/PU samples

of motion, corresponding to the four parts of the unitcell, Figure 3.2. After solving the equations subjected to the boundary conditions, the maximum stress in the bricks (σ_b), the maximum shear stress in the horizontal interface (τ_i), the stress in the vertical interfaces (σ_i), and the composite stress (σ_c) can be found as:

$$\sigma_b = E_b u_2'(0) \tag{3.34}$$

$$\tau_i = \frac{G_m}{h} u_2'(0) \tag{3.35}$$

$$\sigma_i = E_b u_1'(0) \tag{3.36}$$

$$\sigma_c = \frac{1}{2} E_b \big[u_1'(0) + u_2'(0)\big] \tag{3.37}$$

The effective properties of the composite can then be readily obtained from these equations. Using Eq. 3.37, the stress in the composite can also be found as a function of sample geometry, properties of the components, and the composite strain. Dividing the stress by the strain in the composite leads to the stiffness of the composite as a function of microstructural geometries and properties of the constituents, as:

$$E_c = \frac{\begin{array}{r} wE_b\Big[\big[\frac{1}{2}\sinh(\beta s) + \alpha(\cosh(\beta s)+1)\big]\sinh(\beta(s-w)) - \\ \alpha\sinh(\beta s)\big[1+\cosh(\beta(s-w))\big]\Big] \end{array}}{\begin{array}{c} \big[(1+\alpha w)(\cosh(\beta s)+1)\big]\sinh(\beta(s-w)) - \\ \sinh(\beta s)[(1+\alpha w)(1+\cosh(\beta(s-w)) - \frac{w}{2}\beta] \end{array}}, \tag{3.38}$$

where w is the length of ceramic layer, s is the overlap of the layers, and α and β parameters are defined as follows:

$$\beta = 2\sqrt{\frac{G_m}{E_b h b}}, \qquad \alpha = \frac{E_m}{E_b t}. \tag{3.39}$$

Using Eqs. 3.34-3.36, the stress in the bricks, shear stress in the mortar and stress in the vertical interfaces can also be obtained.

$$\sigma_i = \frac{wE_b\epsilon_c\Big[\big[2\beta sinh(\beta s) + \alpha(cosh(\beta s)+1)\big]sinh(\beta(s-w)) - \alpha sinh(\beta s)\big[1+cosh(\beta(s-w))\big]\Big]}{\big[(1+\alpha w)(\cosh(\beta s)+1)\big]\sinh(\beta(s-w)) - \sinh(\beta s)[(1+\alpha w)(1+\cosh(\beta(s-w)) - \frac{w}{2}\beta\big]} \tag{3.40}$$

$$\sigma_b = \frac{wE_b\epsilon_c\alpha\Big[\big[cosh(\beta s)+1)\big]sinh(2\beta(s-w)) - \alpha sinh(\beta s)\big[1+cosh(\beta(s-w))\big]\Big]}{\big[(1+\alpha w)(\cosh(\beta s)+1)\big]\sinh(\beta(s-w)) - \sinh(\beta s)[(1+\alpha w)(1+\cosh(\beta(s-w)) - \frac{w}{2}\beta\big]} \tag{3.41}$$

$$\tau_i = \frac{wE_b\epsilon_c\Big[\big[cosh(\beta s)+1\big]sinh(\beta(s-w))\Big]}{\big[(1+\alpha w)(\cosh(\beta s)+1)\big]\sinh(\beta(s-w)) - \sinh(\beta s)[(1+\alpha w)(1+\cosh(\beta(s-w)) - \frac{w}{2}\beta\big]} \tag{3.42}$$

Finally, α and β parameters can be simply modified to implement the effects of imperfect interfaces into the shear lag model as:

$$\alpha = \frac{D_s b E_m}{E_b t(2E_m + bD_s)}, \qquad \beta = 2\sqrt{\frac{G_m D_s}{E_b b(D_s h + E_m)}}. \tag{3.43}$$

The elastic modulus and the stresses in different elements of the idealized 2-D lamellar structure can then be derived as a function of interface property. Fig. 3.9 shows the effect of ceramic lamella thickness on the elastic modulus of the samples. The figure also compares the experimental and theoretical results found in this study.

Comparing the theoretical results of models with perfect and imperfect interfaces show that the effect of imperfection increases as the lamella thickness decreases. Moreover, comparing the experimental results with the theoretical ones show that the samples with higher lamella thickness behave similarly to the samples with the perfect interface, however, as the lamella thickness decreases, the results lean mostly toward the samples with the imperfect interface. The interface imperfection parameter is assumed to be rather higher

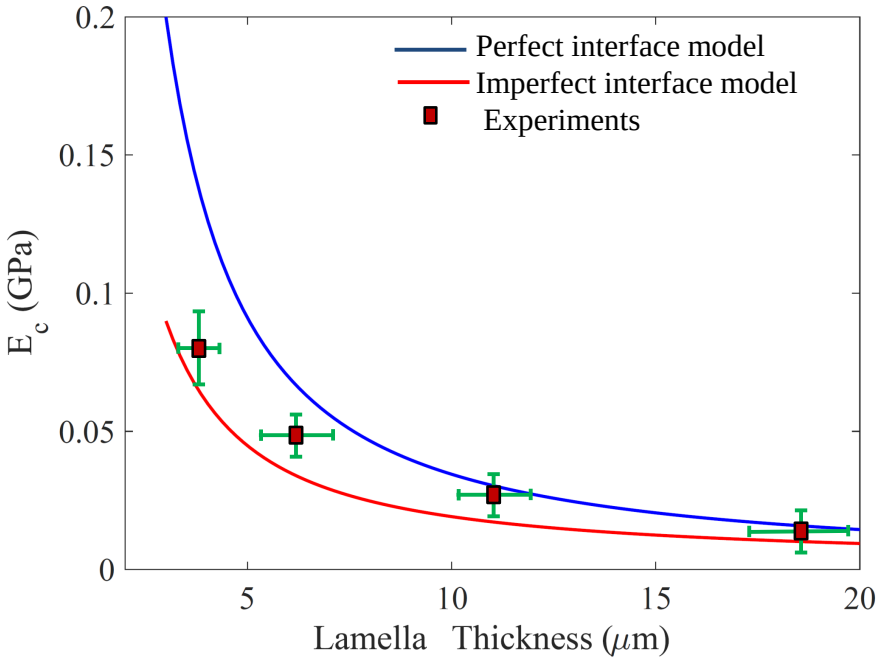

Figure 3.9: Effect of ceramic lamella thickness on the elastic modulus of the bioinspired Al_2O_3/PDMS samples. The mortar thickness assumed to be 50% larger than the ceramic lamella thickness according to the SEM images and the volume fraction of the polymer. The error bars represent the standard deviation in the lamella thickness and the elastic moduli.

for PDMS samples than the ones for PU samples. This is due to two physical phenomena: 1) a molecule agglomerate of PU is larger than PDMS, and this prevents perfect influx of the polymer into the surface voids of the ceramic lamella; and 2) the curing time for PDMS is higher, and this causes more interaction between the ceramic and the polymer layers before the final curing stage. These two different levels of interface imperfection are presented in SEM images obtained from the samples in Fig. 3.10

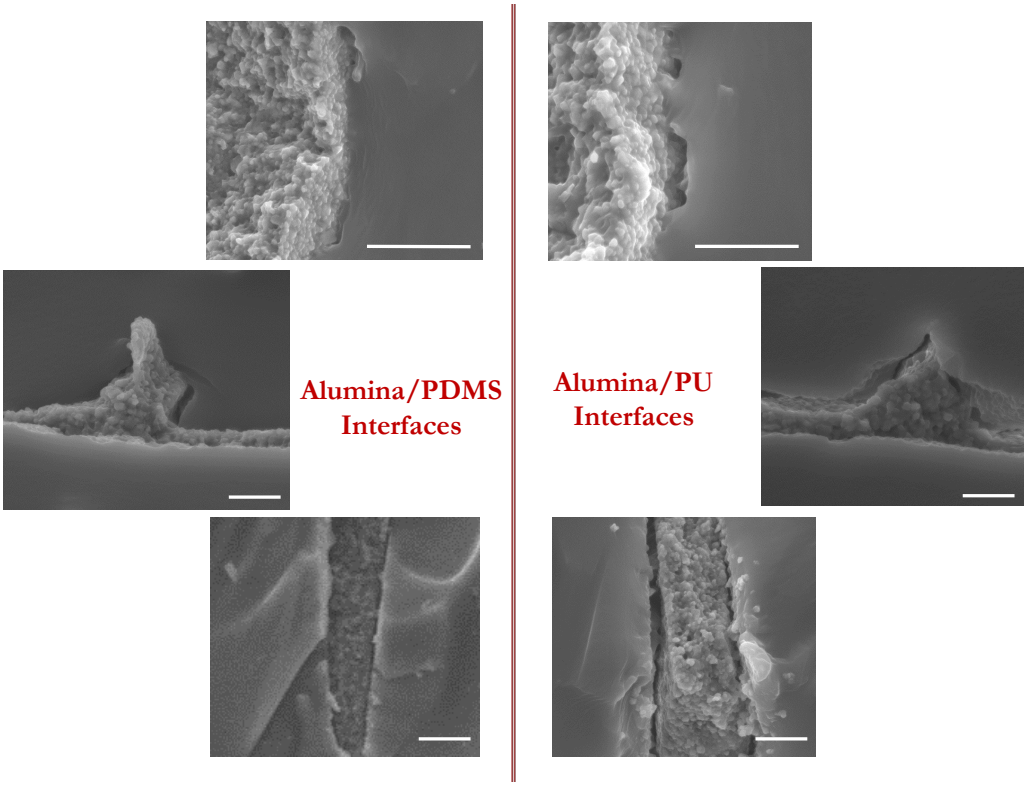

Figure 3.10: The interface property in the samples is a function of different chemical and physical properties of polymers. The imprecations are more dominant at the alumina/PU interfaces.

Using the stresses found in the previous sections, following the shear-lag theory, the composite's strength can now be predicted. The magnitude of stresses in each element at different strain levels defines the failure sequences in the material system. As it can be seen in a unit-cell structure, the vertical interface would fail first if the bricks can tolerate the applied stress. However,

the failure in the horizontal interfaces eventually causes the sample's final rupture.

In all these multilayered composites, the ideal scenario is to prevent the failure in the bricks, as it will quickly diminish the strength of the composite. This leads to the use of strong ceramics in these composites. The random flaws in some of the plates does not significantly affect the system as long as there are strong horizontal interfaces. Consequently, the composite can still carry the load after vertical failure, such that the strength is essentially dictated by the stress required to subsequently fail all the horizontal interfaces, or fracture the bricks.

The presented analytical framework is used here to find the peak stress (ultimate strength) of the samples. Obviously, the mechanical response of the components as well as the length scales in the model ultimately define the sequence of failure of the elements, and therefore, the peak stress in the system. In the multilayered composites, the vertical rupture happens at the peak stress. If the vertical rupture is delayed due to a mechanism, the peak stress will increase.

The ideal failure scenario that can occur in a multilayered structure is that the vertical interfaces fail first, then some horizontal interfaces start to fail, following by a failure of all vertical interfaces (vertical rupture), and then failure of all horizontal interfaces (horizontal rupture). However, in the lamellar structured composites with a large volume fraction of polymer, the model shows that vertical rupture happens in a small additional strain after the start of vertical interfaces failure. In Al_2O_3/PU samples, horizontal interfaces start to fail in a higher stress than the Al_2O_3/PDMS samples. The drop in the composite stress (σ_c) is smaller in Al_2O_3/PU samples after vertical rupture. Hence, Al_2O_3/PU samples exhibit a large strain energy in that step. However, more effective fiber pull-out mechanism can be observed in Al_2O_3/PDMS samples since the stress in the bricks never actually reaches to their strength during the fiber pull-out process. Fig. 3.11 schematically summarizes the failure sequence in the Al_2O_3/PDMS and Al_2O_3/PU samples.

The stress required for a specific failure event (e.g. vertical rupture) is found by equating the associated stress with the material strength and solving for the composite strain ϵ_c required for that event. The composite stress (σ_c) can then be found by multiplying the obtained strain by the composite modulus for that specific event.

In order to find the peak composite stress, failure stress, and failure strain, the following steps need to be taken, since the lamellar structure assumed to

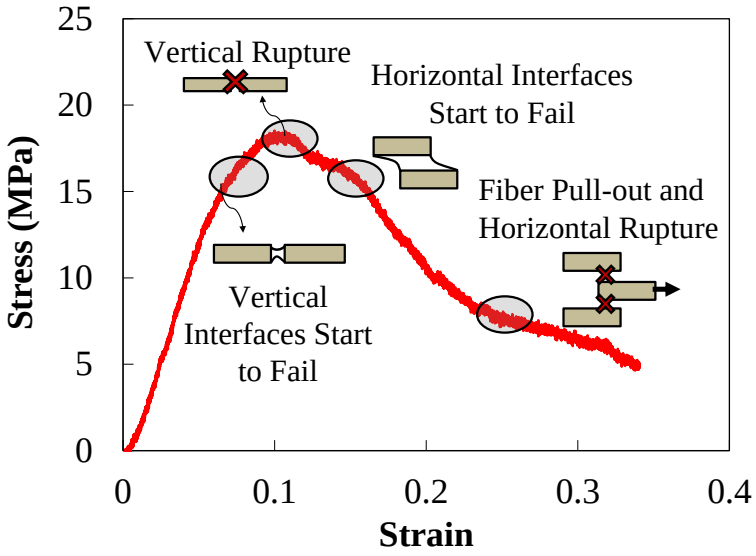

(a)

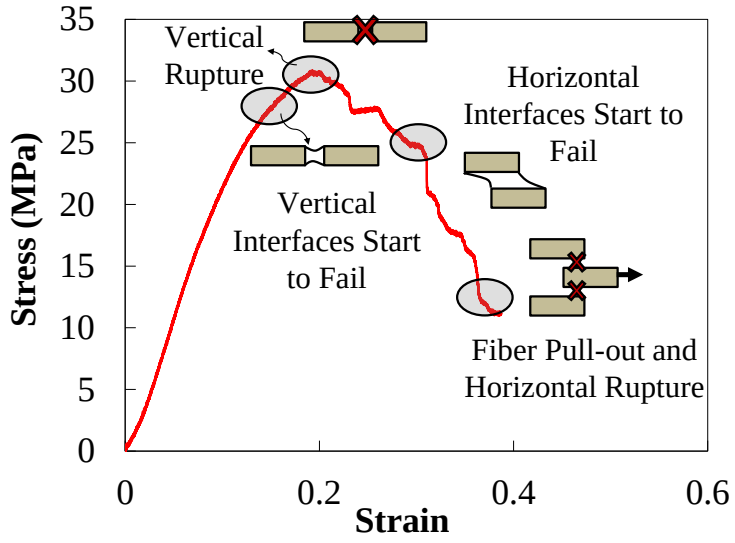

(b)

Figure 3.11: Failure sequences in (a) Al_2O_3/PDMS, and (b) Al_2O_3/PU samples

be a brick and mortar structure with large mortar fractions [101]: 1) Using the properties of the constituents, calculate the strain in which each of the elements would fail; 2) The minimum strain, is defined as the first failure event. If this strain corresponds to either the brick failure or horizontal interface failure, a catastrophic failure will occur, and the corresponding stress is the peak and failure stress; 3) If the minimum strain corresponds to the vertical interface, the next failure event needs to be found. In order to do that, the stress in the bricks and horizontal interface should be found assuming the failed vertical interface ($\alpha = 0$); 4) If either of stresses in the brick or the horizontal interface (with $\alpha = 0$) is less than their strengths, the sample fails and the stress in vertical interface is the peak and failure stress; 5) If the stresses in the bricks and horizontal interfaces are smaller than their strengths, more strain can be applied to the sample; 6) Using the new modulus and the computed stresses in the elements, the failure strains of the brick and horizontal interface can be found. The stress corresponding to the minimum strain determines the failure stress; and 7) If this stress is more than the vertical interface failure stress, the obtained stress is the peak stress. Fig. 3.12 schematically shows some of the possible scenarios that can happen. The highest stress in each of the possible scenarios defines the ultimate strength of the samples.

Fig. 3.13a and 3.13b show the calculated analytical strength as a function of ceramic lamella thickness. Similarly, the results of the analytical calculation of strength with the imperfect interface are presented in these figures. It can be observed from these results that the experimental results are similar to the analytical solutions for the imperfect interface problem for the samples with low ceramic lamella thicknesses. Additionally, in Fig. 3.13b the theoretical results show that there is an optimum value for the lamella thickness to achieve the highest strength in Al_2O_3/PU samples. This optimum thickness value decreases as the interface gets weaker. The overall drop in the strength value is mainly due to the brick failure which occurs because of the small aspect ratio of the layers and the high strength of the polymer layers. The effect of interface properties is indeed pronounced in predicting the material properties in these cases. Hence, the results clearly show that the effect of interface modification is quite significant on the strength and toughness of samples.

The presented model can also be used to study tensile toughness (area under the stress-strain curve) of the samples by using the values found for the strength of samples. Fig. 3.14a and 3.14b show the trend in toughness with

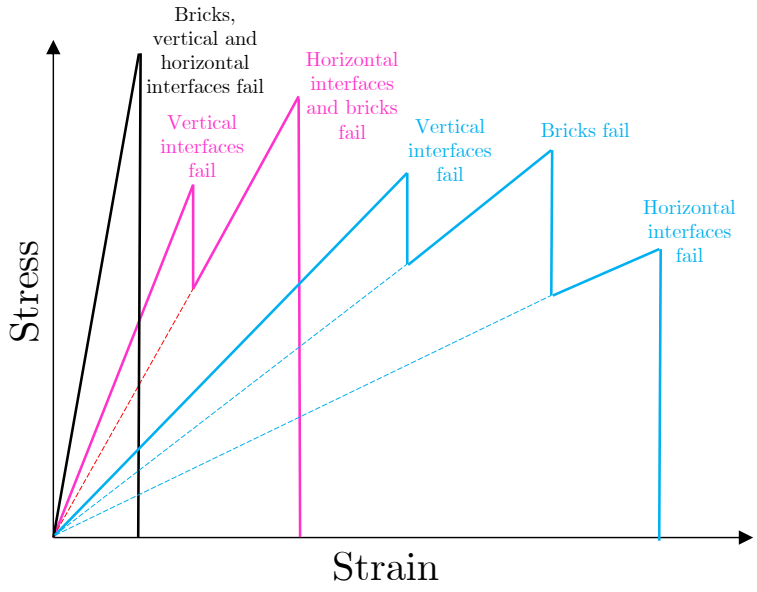

Figure 3.12: Some of the possible scenarios could be predicted using the theoretical analysis. All the parameters are effective on the failure sequences and subsequently the maximum strength.

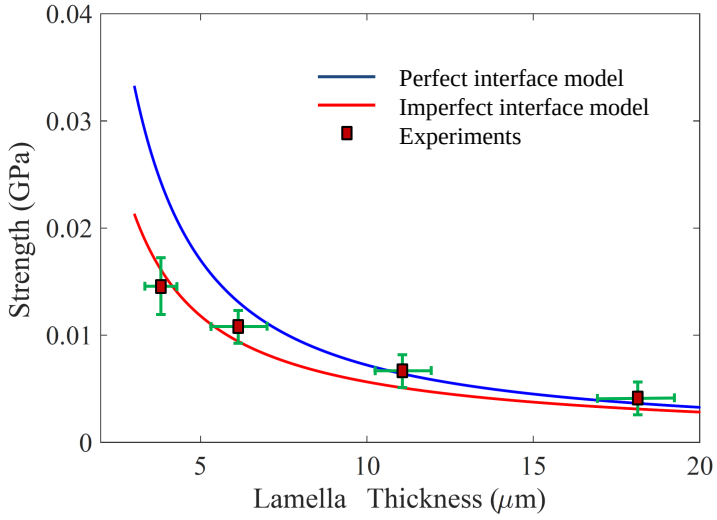

(a)

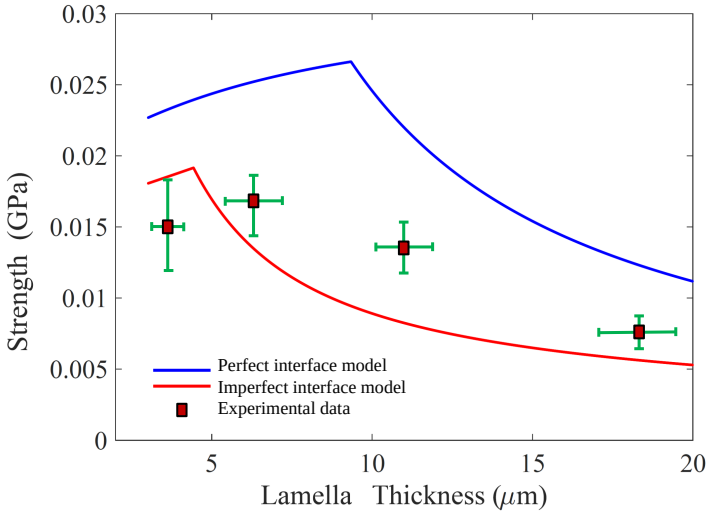

(b)

Figure 3.13: Effect of ceramic lamella thickness on the strength of the (a) Al_2O_3/PDMS and (b) Al_2O_3/PU samples. The mortar thickness assumed to be 50% larger than the ceramic lamella thickness according to the SEM images. The error bars represent the standard deviation in the lamella thickness and the strength.

respect to the elastic moduli of composites. The toughness values calculated from the experimental results are also presented in these figures. Experimental results for all samples are predicted closely with the analytical solutions, and the trend in toughness variation as a function of elastic modulus matches well with the presented imperfect interface model. The differences between the experimental and modeling results can be listed as: 1) The thickness and length of the plates are not uniform throughout the samples, and the limitations in the manufacturing method (such as excessive vibration in higher cooling rates) caused some minor anomalies in the microstructure; 2) The behavior of the polymer layer may be different at different thicknesses while we assume the same number for the specific material in the theoretical model; 3) The interactions of polymer with ceramic layer at the final stage of deformation that is important in toughening mechanisms is not included in the shear-lag model. When the polymers are soft, the toughness increases as the elastic modulus increases; however, when the polymer are stiff and strong, the toughening mechanisms at the later stages of the deformation are less effective and the toughness does not increase as the elastic modulus increases.

3.3.3 Fracture Toughening mechanisms

The tensile toughness added to materials due to the presence of fibers in the system can be calculated by the following equation [151]:

$$\Delta K = 2f \int_0^{u_*} \bar{\sigma}(u) du \tag{3.44}$$

where K is the toughness, f is the volume fraction of fibers, u is the crack opening, u_* is the minimum of two crack opening values, opening at the crack mouth and opening at the edge of the bridging zone, whichever is smaller (Fig. 3.15). $\bar{\sigma}$ is the net traction applied on the matrix crack by fibers in the crack wake. In fiber/matrix systems, both intact fibers and fibers that fail away from the crack plane increase the stress needed for crack growth [152]. Unbroken fibers toughen the system by bridging effect and the broken ones resist crack opening by frictional sliding as the fibers pull out of the matrix [153].

In the studies about the composites with ceramic fibers, they usually assign a specific number for the strength of the fibers (S), however this is not what happens in the reality. If we assume a certain number for the strength of the fibers, they must fail at the location of the highest stress, which eliminates

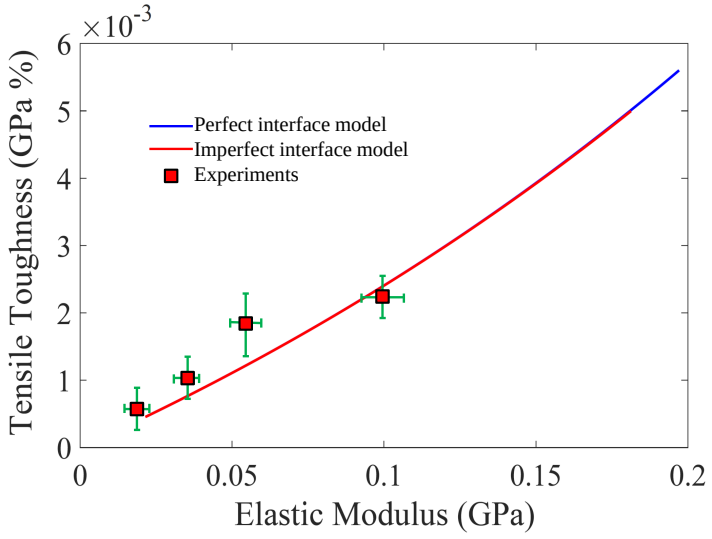

(a)

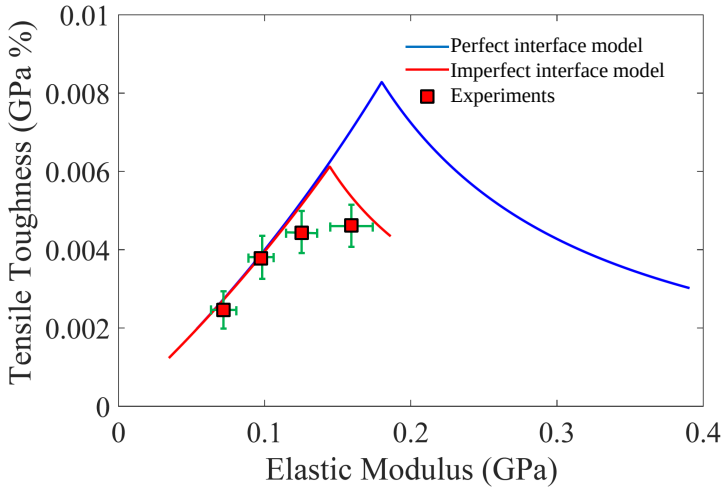

(b)

Figure 3.14: Variation of tensile toughness in (a) Al_2O_3/PDMS and (b) Al_2O_3/PU samples: Tensile toughness increases as the elastic modulus increases in samples with the soft matrix (such as PDMS). For PU samples, there is an optimum value for the toughness as the elastic modulus increases. The effect of imperfect interface is significant in these samples.

the effect of fiber pull-out in the analysis. Here, the contribution of both fiber bridging and pull-out on the crack growth resistance is taken to account by considering the statistical nature of failure in brittle ceramic fibers.

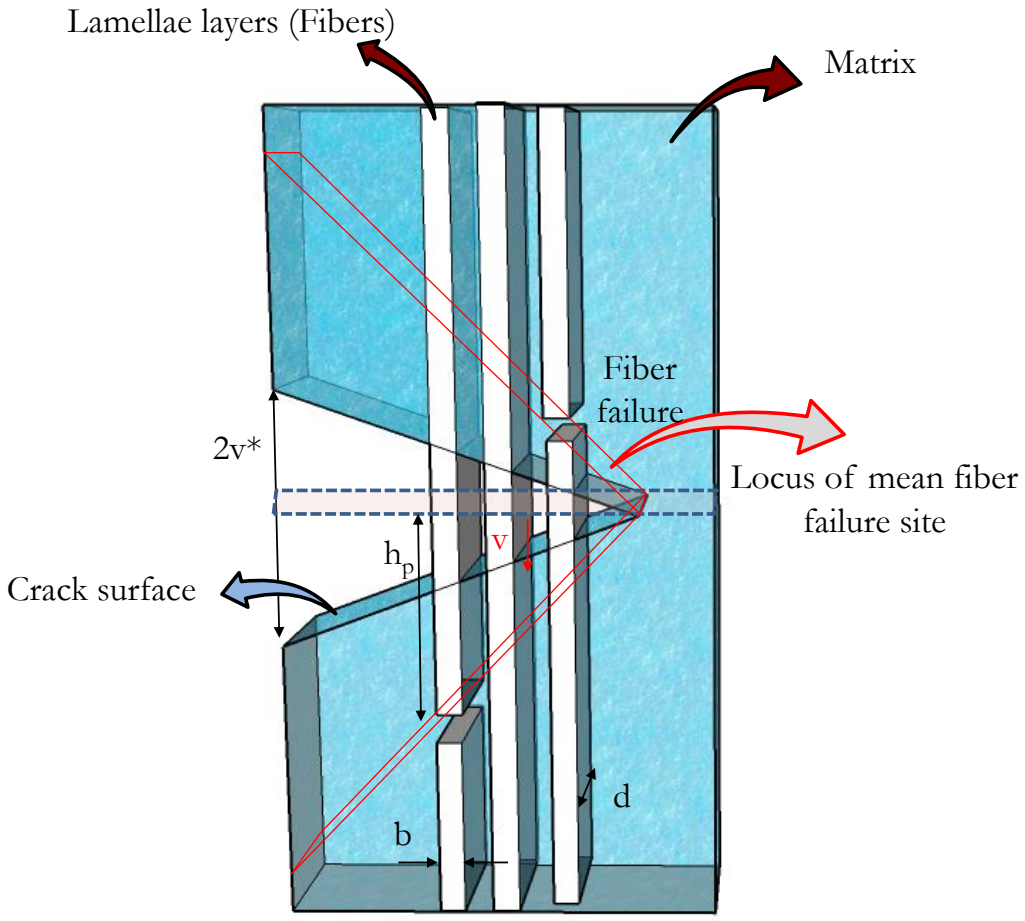

Figure 3.15: A schematic indicating crack bridging by intact and fractured lamellae layers. Different dimensions and the locus of mean fiber failure site are shown in the figure. Fiber pull-out length can also be found.

The fibers are assumed to have a highly imperfect interface so that they slip with respect to the matrix in the crack wake at a constant shear resistance, τ, which can be found by analyzing the matrix shear strength and

the interface properties [154]. The resulting slip length, l, is presumed to be large enough to allow all of the interfacial shear to be accommodated along the zone of sliding. The axial stress in each intact fiber varies within the slip length,

$$\sigma = T(1 - \frac{z}{l}), \qquad l = \frac{TA}{M\tau} \tag{3.45}$$

where T is the stress in the fiber at the crack plane, $A = b \times d$ is the fiber cross section area (b is the fiber thickness and d is the lamellae layer depth), $M = 2(b + d)$ is the fiber circumference exposed to the matrix, and z is the distance from the crack plane. A further assumption of the analysis is the use of a fiber strength distribution that satisfies weakest-link statistics. The probability density function, P, for fiber failure as a function of the peak stress, T, and the distance from the crack plane, z, can be derived as:

$$P = \frac{2md}{A_0\sigma_0^m}(T - \frac{2z\tau}{b})^{m-1} \exp\Big(\frac{-2bdT^{m+1}}{(m+1)\tau A_0\sigma_0}\Big) \tag{3.46}$$

where d is the depth of the lamellae layers, m is the shape parameter and σ_0 is the scale parameter. Eq. 3.46 is the basic formula that governs several statistical parameters such as pull-out length, $\langle h \rangle$, the mean strength, $\langle S \rangle$ and the net stress, $\bar{\sigma}$. These parameters play important roles in toughness of the lamellar structured composites. The average failure position for all fibers that have failed at a stress less than T can be found and simplified as:

$$\bar{h} = \frac{A_0}{4(b+d)}\Big(\frac{\sigma_0}{\eta}\Big)^m \Gamma\Big(\frac{m+2}{m+1}\Big) \tag{3.47}$$

where Γ is the complete gamma function and:

$$\eta = \Big[\frac{A_0\sigma_0^m\tau(m+1)}{2A}\Big]^{\frac{1}{m+1}}. \tag{3.48}$$

As it can be seen in this equation, the fiber pull-out length can be calculated as a function of the lamellae thickness and the shear stress in the mortar. Fig. 3.16 shows the fiber pull-out length versus the lamellae thickness for different shear resistance of mortar. As the shear resistance increases, the pull-out length decreases.

Therefore, the corresponding solution for the mean strength of all the fibers is:

$$\bar{S} = \eta\Gamma\Big(\frac{m+2}{m+1}\Big). \tag{3.49}$$

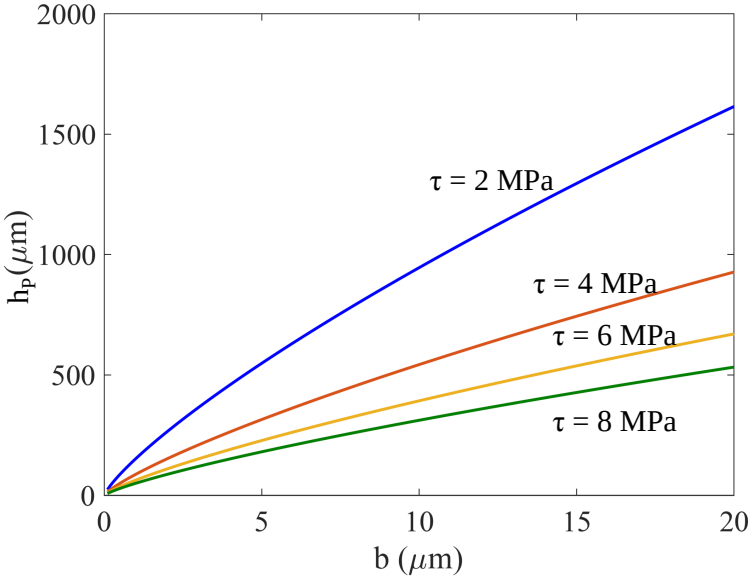

Figure 3.16: Fiber pull-out length as a function of lamellae thickness for different shear resistance of the mortar. Decreasing the shear resistance and increasing the lamellae thickness increase the fiber pull-out length.

In order to find the effect of fibers on the toughness of composites, the fraction of fibers that fail at each location behind the crack tip and the associated failure site should be determined. The fraction of failed fibers near the matrix crack front can be assumed to be zero. As the matrix crack grows, the weaker fibers begin to fail in the immediate crack wake, near the crack plane. Thereafter, upon additional crack extension, farther fibers fail in the wake, at locations further from the crack plane. Hence, for failed fibers, the stress at the crack plane is:

$$\sigma_p = \frac{2\pi\tau}{(b+d)}(h-u) \qquad (h > u) \tag{3.50}$$

$$\sigma_p = 0 \qquad (h < u) \tag{3.51}$$

where u is the crack opening displacement. Moreover, for intact fibers, the peak stress, T, can be determined by the following equation:

$$T = \left(\frac{4\pi E_f \tau (1+\zeta) u}{b+d}\right)^{\frac{1}{2}} \tag{3.52}$$

where ζ is:

$$\zeta = \frac{E_f f}{E_m(1-f)} \tag{3.53}$$

Using these analysis, the average stress, $\bar{\sigma}$, on the fibers at an opening u can be written as:

$$\bar{\sigma} = (1-q)T + q\langle\sigma_p\rangle \tag{3.54}$$

where q is the fraction of fibers that have failed at opening, u, and $\langle\sigma_p\rangle$ is the average value of the pull-out stress associated with all prior failures. An important point in using this equation is that the number of fibers assumed to be sufficient to allow use of average values, which is quite practical in microstructured lamellar composites. The fraction of failed fibers at an opening u can be found using the proposed probability function, P, by finding the cumulative fiber failure probability at $S = T$.

$$q \equiv \int_0^S \int_0^l P(z,T)dzdT \tag{3.55}$$

Hence, the average stress in the fibers in the lamellar structured composite with respect to the crack opening, geometric parameters and mechanical properties of the constituents can be derived as:

$$\begin{aligned}\bar{\sigma} = \eta\sqrt{\frac{u}{\nu}}\exp\Big[-(\frac{u}{\nu})^{\frac{m+1}{2}}\Big] + \frac{\eta}{(1+\zeta)(1+m)}\big\{1-\exp[-(\frac{u}{\nu})^{\frac{m+1}{2}}]\big\} \\ \times\big\{\gamma[\frac{m+2}{m+1},(\frac{u}{\nu})^{\frac{m+1}{2}}] - \frac{\eta(m+1)}{2E_f}(\frac{u}{\nu})\big\}.\end{aligned} \tag{3.56}$$

The average stress for a crack opening length is a function of geometry, shear resistance and Weibull parameters. Fig. 3.17 shows the dependence of average stress on the prescribed parameters.

Using this analysis, the details on toughness can be highlighted by separately considering the contributions of fiber bridging and fiber pull-out. Hence, the bridging and pull-out components of the toughness can be found and simplified as:

$$\Delta K = 2f\int_0^{u_*}\bar{\sigma}(u)du = 2f\int_0^{u_*}[(1-q)T+q\langle\sigma_p\rangle]du = 2f\Big(\underbrace{\int_0^{u_*}[(1-q)T]du}_{\Delta K_b} + \underbrace{\int_0^{u_*}q\langle\sigma_p\rangle du}_{\Delta K_p}\Big) \tag{3.57}$$

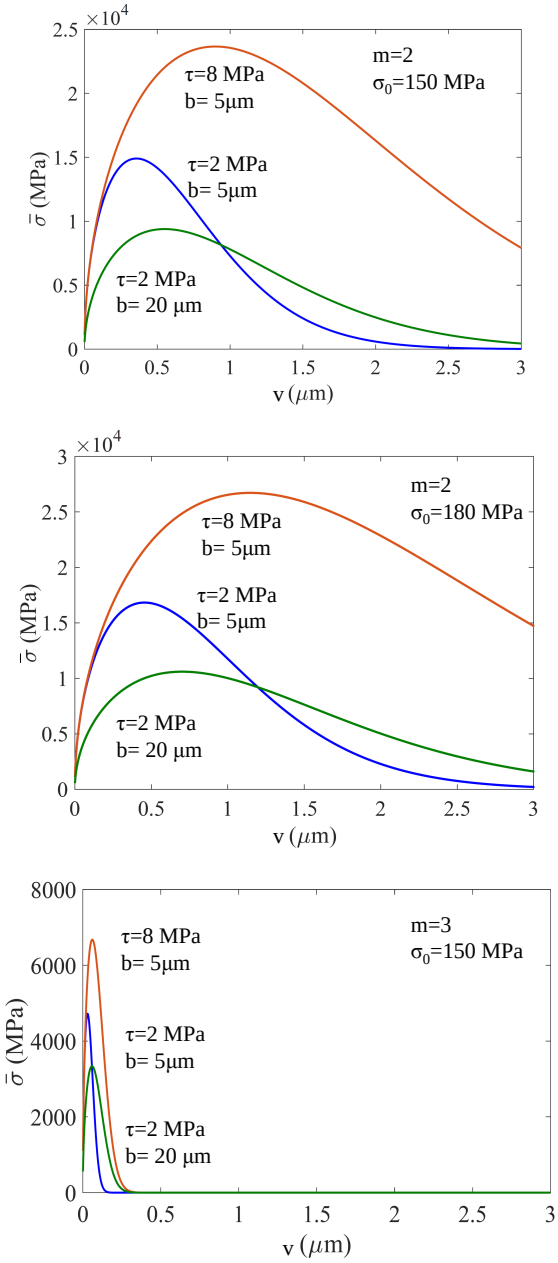

Figure 3.17: Stress/displacement characteristics for a crack surface bridged by fibers. The purpose of these graphs is to illustrate the dependence of toughness on the shear resistance and thickness of the lamellae at particular amount of m and σ_0

$$\Delta K_b = \frac{4f\nu\eta}{m+1}\gamma\Big[\frac{3}{m+1}\ , (\frac{u_*}{\nu})^{\frac{m+1}{2}}\Big] \tag{3.58}$$

$$\Delta K_p \sim \langle h\rangle^2\Big(\frac{(b+d)\tau}{bd}\Big) \tag{3.59}$$

where $\gamma(r,s)$ is the incomplete gamma function and:

$$\nu = \frac{\eta^2 bd}{4E_f\tau(1+\zeta)(b+d)} \tag{3.60}$$

As it is shown, the crack mouth opening (u_*), has an important effect on toughening mechanism [155]. If we assume that the crack has an elliptical shape, u_* can be found with the following equation:

$$u_* = \frac{2K_c}{\bar{E}}\sqrt{\frac{a}{\pi}} \tag{3.61}$$

where $\bar{E}$ is the plane strain Young's modulus and a is the length of crack. Using the equation the fiber pull-out and bridging energy release rates can be found as a function of the major contributing parameters (Fig. 3.18).

Moreover, selection of lamella's mean strength, m, and lamella's strength distribution function, σ_0, within the typical range obtained experimentally [156], enables prediction of specific stress/displacement characteristics for a crack surface bridged by lamella. Here, we used the values of m and σ_0 previously found experimentally for alumina samples [157, 158]. For our samples made by freeze casting and sintered in 1500°C for two hours, both these values are assumed to be less than the regular alumina samples. Moreover, in the freeze casting process, larger number of flaws appear in the ceramic lamella of samples fabricated with a high cooling rate. Hence, for samples with thinner lamella, a smaller value of m should be assumed. Considering all these assumptions, the extreme cases for our bioinspired composite corresponds to Al_2O_3/PDMS samples with lamella thickness of 18 μm with the highest fiber pull-out toughening, and Al_2O_3/PU samples with lamella thickness of 4 μm with the highest fiber bridging effect. These findings can also be observed in the R-Curves found by fracture experiments presented in Fig. 3.7.

The contributions to overall fracture energy from the toughening mechanisms, $\Delta J = \Delta J_b + \Delta J_p$, in PDMS samples are compared in Table 3.2.

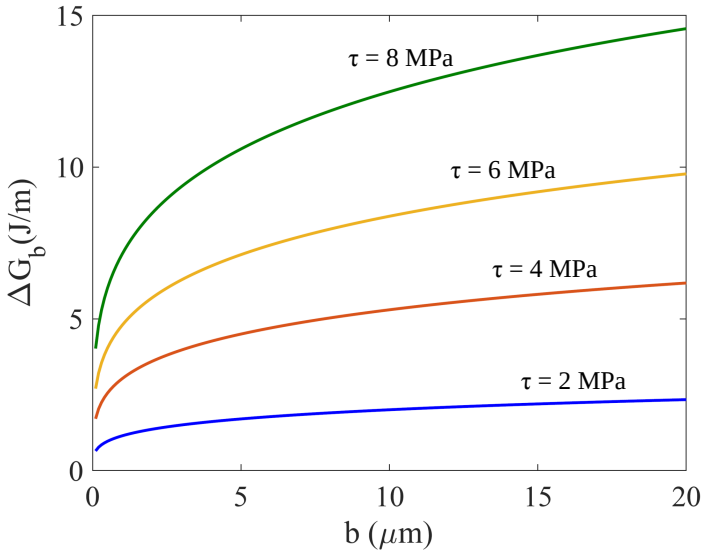

(a)

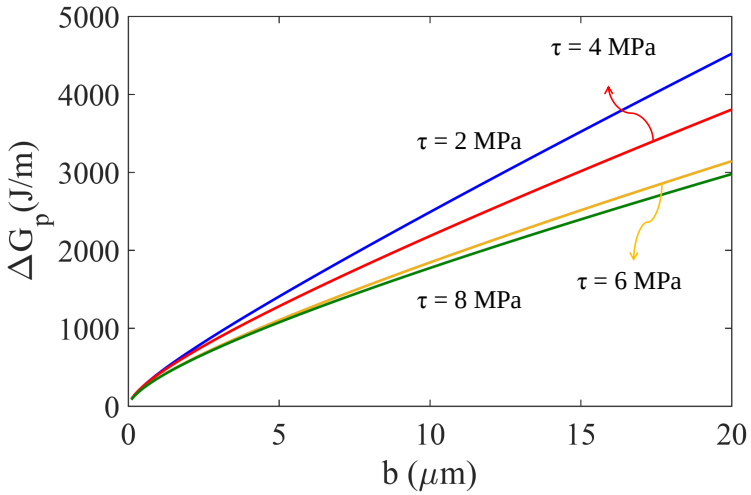

(b)

Figure 3.18: The energy release rate gradient due to the bridging and pull-out toughening mechanisms. As the results show, in the lamellar structured composites, the effect of fiber pull-out is more significant than the bridging effect.

These data clearly validates the presented theoretical framework in predicting fracture energies of bioinspired lamellar composites for the range of lamella thicknesses investigsated.

Table 3.2: Comparison between the theoretical and experimental energy release rate data

Lamella Thickness (μm)	$\Delta J_p + \Delta J_b (J/m^2)$	$\Delta J_{exp} (J/m^2)$
4	1015	550 $\pm$ 428
6.5	1623	1920 $\pm$ 121
11	1786	2120 $\pm$ 254
18	4361	4820 $\pm$ 322

3.4 Implications

The implications of these results are quite significant in the design of biologically inspired super-tough ceramic composites. Man-made brick and mortar and lamellar ceramic/polymer composites with optimized structure and components' mechanical properties can outperform nacre in toughness. However, microstructural requirements to improve strength, stiffness, and toughness are different for lamellar structures. Decreasing the lamella thickness increases the elastic modulus in the layered structure and the detailed properties of the matrix play the main role in the maximum amount of stress that the composite can tolerate. The results presented here would, therefore, suggest that there are different material design parameters that need to be taken to account to achieve the optimal material properties for a specific application using the freeze casting technique. There are also some design and fabrication limitations for lamellar structured samples made by this method: 1) the thickness of the layers are limited to 4-18 μm, 2) there are limitations in material selection with specific desired properties, and 3) there are limitations in matrix material selection due to the complexity of matrix infiltration. There is also a significant need to investigate the effect of weak interface properties in these bioinspired composites in order to compute the optimum microstructure and materials selection. Interface properties which depend on the chemical and mechanical bonding between ceramic lamella and matrix, impose another important design parameter into the multilayered materials mechanics models.

3.5 Conclusions

We have investigated the mechanical response of bioinspired structural composites made by freeze casting method. Al_2O_3/PDMS and Al_2O_3/PU lamellar composites were fabricated, characterized and experimentally analyzed. The main goal of this study is to understand the deformation and toughening mechanisms of the lamellar structured composites. For this purpose, an experimental setup was built and used to fabricate multilayered ceramics/polymer composite using the cumbersome freeze casting technique. A shear-lag model was also developed to study the effective properties of these composites.

The overall performance of multilayered bioinspired materials depends on four important factors: 1) geometry of the microstructure which can be controlled by the cooling rate in freeze casting method, 2) properties of the ceramic lamella, 3) properties of the polymer (matrix), and (4) the ceramic/polymer interface properties. The results show that the toughness of composite decreases as the ceramic layer thickness decreases. Hence, the optimum thickness depends on the overall mechanical properties of the components. Fiber bridging and pull-out processes were theoretically and experimentally investigated as the main toughening mechanisms, and correlated with the increase in the crack resistance curve of the samples.

In this chapter, the imperfect interface model was also implemented in the shear-lag model describing the deformation mechanisms in multilayered composites. The analytical results using the imperfect interface model match well with the experimental results obtained from the samples fabricated by freeze casting technique. Hence, the findings of this study allow us to optimize and improve the mechanical performance of lamellar structured composites made by freeze casting. Moreover, the results of this study emphasize the effect of interface properties (which is the key feature in biological materials) and further enable us to focus on nature's strategy to create superb biological composites such as nacre.

4

Organic-inorganic Interfaces in Nacre

4.1 Introduction

Exceptional combination of mechanical properties, high stiffness, high strength and high ductility makes nacre one of the toughest materials known. Outstanding properties arises from the stacking structure of nacre and the nanoscale vital features in that structure. Moreover, problem-solving strategies of naturally growing composites such as nacre give us a fantastic vision to design, optimize and fabricate tough, stiff while strong composites. In order to provide the outstanding mechanical functions, nature has evolved complex and effective functionally graded interfaces. Particularly in nacre, organic-inorganic interfaces in which the proteins behave stiffer and stronger in proximity of calcium carbonate minerals provide an impressive role in structural integrity and mechanical deformation of the natural composite. This proximity layer is called the interphase layer. Further research on the toughening mechanisms and the role of the interphase properties is essential as a guide to design and synthesize new materials. In this study, a micromechanical analysis of the mechanical response of Brick-Mortar and Brick-Bridge-Mortar composites is presented considering interphase properties. The well-known shear-lag theory was employed on a simplified two-dimensional unit-cell of the multilayered composite. The closed-form solutions for the displacements in the elastic components as a function of constituent properties can be used to calculate the effective mechanical properties of composite such as elastic

modulus, strength and work-to-failure. The results solve important mysteries about nacre and emphasize the role of the organic-inorganic interface (interphase) properties. The effect of mineral bridges is also studied. Our results show that the properties of proteins in mineral bridges proximity are also significant especially in increasing the elastic modulus of the structural composite. Detailed relationships are presented to identify future directions for advanced material design and development. More studies need to be performed on the effect of imperfect interface in manmade materials and on the strategies to enhance the interface properties.

There are many analytical studies on the structure of multilayered composites. Analytical model proposed by Jager and Fratzl (2000)[115] estimated the maximum stress and strain of the composite, by advancing previously established models for the mechanical properties of mineralized collagen fibrils [116]. Micromechanical model developed by Kotha et al. (2000) [117] derived axial and shear stress distribution in platelets on the assumption of a fundamental basis that the load carried by the platelets remains constant and inter-platelet load transfer occurs by shear. Tension-shear-chain (TSC) model postulated by Gao et al. (2003) [92] established the relationship between stiffness, aspect ratio of minerals, mineral volume fraction and material properties. Additionally, a critical overlap length, using Griffith's fracture criterion, was developed which attributed to the existence of an optimal aspect ratio of mineral crystals in biological composites. Shuchun and Yueguang (2007) [118] used shear-lag model to study the interdependence of the overall elastic modulus and number of hierarchical levels in bone-like materials, and compared their results against TSC model and finite element simulations.

Interfaces in composite materials are one of the main sources of their complex behavior. Many studies have investigated the role of interface in nacre and nacre-inspired composites. Barthelat et al. (2012) studied the effect of interface on the toughness of different species of nacre [159]. In another study, Zhang et al. (2016) reviewed the interface interaction design in the graphene-based artificial nacre nanocomposites [160]. They focused on the effect of different chemical bonding on the mechanical response of these samples. In a similar study, the effect of adhesion energy between the fiber and matrix in clay nanocomposites is studied and discussed by Wang et al. (2014) [143]. Ghosh et al. (2007) investigated the interaction between the protein and the minerals in nacre and claimed that protein behaves stiffer and stronger in proximity of minerals [75]. This is usually the case in natural

materials that the transitions between different materials happen in a gradual manner. In other words, the protein acts as a functionally graded material whose properties changes as its distanced from minerals varies.

In this chapter, the proximity layer (interphase) is assumed as one extra layer between minerals and protein. Furthermore, shear-lag model is used to investigate the role of interphase properties such as its stiffness and thickness in overall mechanical performance of nacre. The effect of mineral bridges and their volume percentage on the mechanical properties of nacre is analyzed using this model. The results solve a great mystery about high stiffness of nacre that cannot be justified without considering the mineral bridges.

4.2 Materials and Methods

In order to discuss the effective properties of the multilayered composite, the balance of forces for the components of its unit-cell following by period boundary condition should be applied. Hence, the shear-lag theory employed on a simplified 2D unit-cell was taken into consideration. Shear-lag analyses in the composites always contain several approximations. One of important simplifications involved is the assumption about in-plane shear stress, τ_{xy}, to decouple the x and y directions. This decoupling permits 2D-planar elasticity problems to be simplified to a 1D analysis. The in-plane shear stress by exact linear elasticity is:

$$\tau_{xy} = G_{xy}(\frac{\partial v}{\partial x} + \frac{\partial u}{\partial y}) \tag{4.1}$$

where v is displacement in the y direction and u is the displacement in the x direction and G_{xy} is in-plane shear modulus. Hence, considering the layers of composite lying down in x direction, the fundamental assumption common to all planar, shear-lag analysis is that:

$$\frac{\partial v}{\partial x} = 0 \Longrightarrow \tau_{xy} \propto \frac{\partial u}{\partial y} \tag{4.2}$$

For unidirectional composites the shear-lag theory can be summarized in the following equation:

$$\frac{d^2 P_I}{d^2 x} - [M_{I,\sigma}]P = -[M_{I,\sigma}]P_{I,\infty} \tag{4.3}$$

where P is the vector of forces per unit plate depth on the layers and can be defined as:

$$P = (t_1 < \sigma_x^{(1)} >, t_2 < \sigma_x^{(2)} >, ..., t_{n-1} < \sigma_x^{(n-1)} >) \tag{4.4}$$

considering the layers with even numbers as the stiff layers:

$$P_1 = (t_2 < \sigma_x^{(2)} >, t_4 < \sigma_x^{(4)} >, ..., t_{n-3} < \sigma_x^{(n-3)} >) \tag{4.5}$$

and $P_{I,\infty}$ is the far field or steady state tensile stresses in each layer when there are no shear stress boundary conditions; in other words, the tensile forces in the layers under constant axial stress far away from any end or from any discontinuities or breaks in any layers. Moreover, the Matrix M can be defined as:

$$M_{I,\sigma} = \frac{\beta^2}{E_b t_b t_m} \begin{pmatrix} 1 & -1 & 0 & 0 & ... \\ -1 & 2 & -1 & 0 & ... \\ 0 & -1 & 2 & -1 & ... \\ & & \downarrow & & \\ ... & -1 & 2 & -1 & 0 \\ ... & 0 & -1 & 2 & -1 \\ ... & 0 & 0 & -1 & 1 \end{pmatrix}$$

The idealized composite geometry is shown in Fig. 4.1. The wallpaper symmetry group is pmm, with two bricks per unit cell, which are separated by one brick height vertically, and shifted by s horizontally. For s=$\frac{w}{2}$, the symmetry increases to cmm. The mortar thickness between adjacent plates in each layer(vertical mortar) is assumed to be small in comparison to the brick dimensions (t). It is assumed that the components deform only in the x-direction (the arrangement of the bricks in the through-thickness direction does not factor into the response).

For the assumed geometry $M_{I,\sigma}$ would be as following:

$$M_{I,\sigma} = \frac{\beta^2}{E_b t_b t_m} \begin{pmatrix} 1 & -1 \\ -1 & 1 \end{pmatrix}$$

Hence, this notation leads to the following complete set of governing equations:

$$u_1{}'' = \frac{\beta^2}{E_b.h.b}(u_1 - u_2) \longrightarrow 0 < x < s \tag{4.6}$$

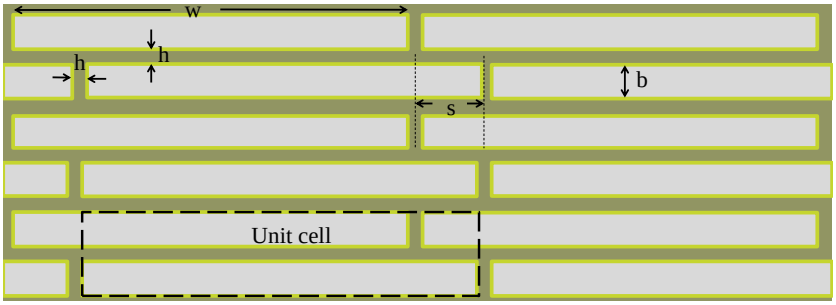

(a)

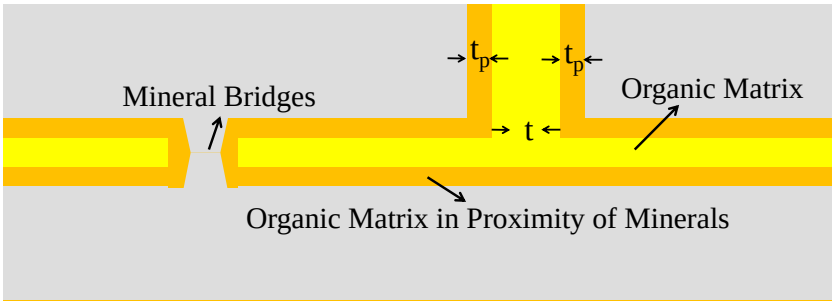

(b)

Figure 4.1: (a) Schematic of idealized super-cell structure and the length parameters (b) Unit-cell structure assumed to apply the shear-lag theory.

$$u_2{}'' = \frac{\beta^2}{E_b.h.b}(u_2 - u_1) \longrightarrow 0 < x < s \tag{4.7}$$

$$u_3{}'' = \frac{\beta^2}{E_b.h.b}(u_3 - u_4) \longrightarrow -(w - s) < x < 0 \tag{4.8}$$

$$u_4{}'' = \frac{\beta^2}{E_b.h.b}(u_4 - u_3) \longrightarrow -(w - s) < x < 0 \tag{4.9}$$

where h is the thickness of mortar. Considering the assumed geometry, $h = 2t_p + t$ in which t_p is the thickness of proximity mortar and t is the thickness of regular mortar. Moreover, the definition of β (if we ignore the mineral pillars in the system) is as following:

$$\beta^2 = \frac{\kappa E_m}{2(\kappa + 2\xi(1-\kappa))(1+\nu)} \tag{4.10}$$

where $\kappa = \frac{E_{mp}}{E_m}$ in which E_{mp} is the elastic modulus of proximity layer and $\xi = \frac{t_p}{h}$. The corresponding boundary (and symmetry) conditions are given by:

$u_{11}(0) = u_{12}(0) = 0$, $u_2(s) = \Delta$, $u_2(s) - u_3(s - w) = \epsilon.w$,
$u_3(0) = u_2(0) = \alpha.(u_2(0) - u_3(0))$, $u'_{11}(s) = u'_{12}(s - w) = 0$,
$u'_{11}(0) = u'_2(s) = u'_3(s - w)$
where α is defined as following:

$$\alpha = \frac{\kappa E_m}{E_b h(\kappa + 2\xi(1-\kappa))} \tag{4.11}$$

Using these boundary conditions the displacement of the different parts of model, u_1, u_2, u_3 and u_4 can be calculated.

4.3 Results and Discussion

In order to investigate the effect of this proximity layer in mechanical properties of nacre and nacre-inspired composites, we refer to one of the studies done by Ghosh et al. (2007) on nacre's organic matrix [75]. Their results show that the organic matrix behaves differently when it is in proximity of minerals. Fig 4.2 shows their molecular dynamics simulation results. The protein behaves approximately three times stronger and six times stiffer and

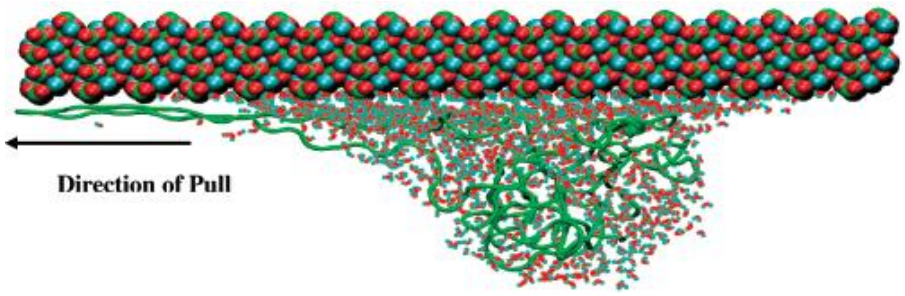

(a)

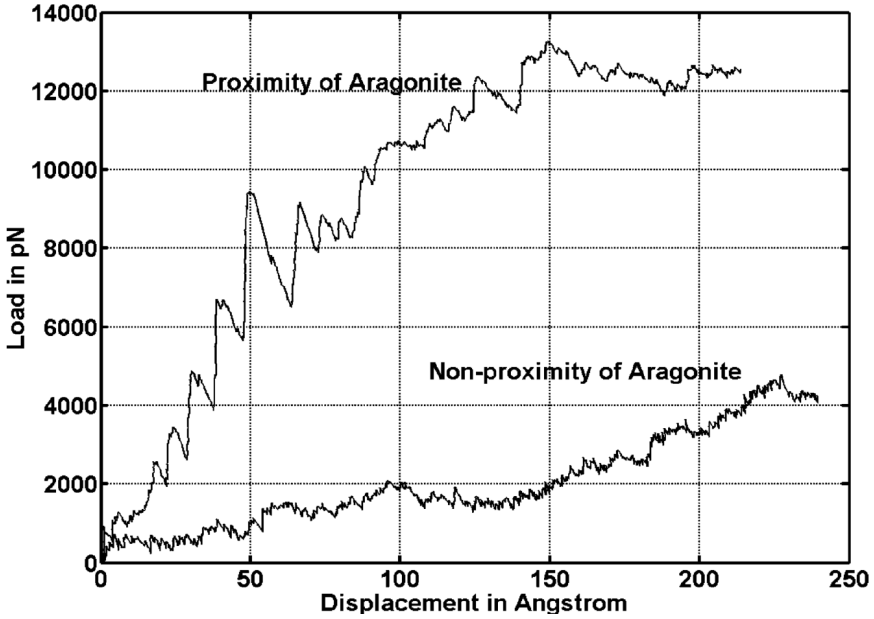

(b)

Figure 4.2: (a) Atomistic simulation of organic matrix of nacre in proximity of aragonite, (b) Comparison between mechanical response of regular protein and protein in proximity of minerals

Using the same formulation used in chapter 3 can be used in order to find the effective mechanical properties of nacreous structure. The effect of properties and thickness of proximity layer on elastic modulus of nacreous materials is shown in the following figures.

These figures show that the effect of proximity layer thickness is more pronounced on modulus of nacre.

4.3.1 Effect of Mineral Bridges

In our finite element analysis on nacreous structure, we showed that mineral bridges have a significant effect on mechanical properties of nacre. Here, we are trying to show this effect using analytical solutions. If we follow the formulation for a unit-cell structure including mineral bridges, the only parameter that changes is β. The new formulation for β would be as following:

$$\beta^2 = \frac{f}{2bh(1+\nu)} + \frac{\kappa E_m}{2(\kappa + 2\xi(1-\kappa))(1+\nu)} \tag{4.12}$$

where f is the volume fraction of mineral bridges. Considering this formulation, the effect of proximity layer on mechanical response of samples including mineral bridges would be as shown in figure 4.4.

Figure 4.5 shows the effect of mineral bridges volume fraction on elastic modulus of nacre.

These results are extremely important and solve a mystery about nacre. In many studies on nacreous structures, the effect of mineral bridges was neglected, however our results show that mineral bridges have significant effect. Figure 4.6 show the effect of 2.5 % mineral bridges on elastic modulus of samples.

4.3.2 Strength and Toughness

The final goal of our studies on the role of proximity layer is to shed light on the effect of proximity layer properties and thickness on strength and subsequently toughness of nacre and nacreous structures. Using the obtained equations we can follow an algorithm to calculate the final strength of these composites. The algorithm used can be summarized as: 1) Using the properties of the constituents, calculate the strain in which each of the elements would fail; 2) as the stresses in all elements of vertical interfaces are same, the regular protein in the vertical interfaces fail first, 3) In order to find the next

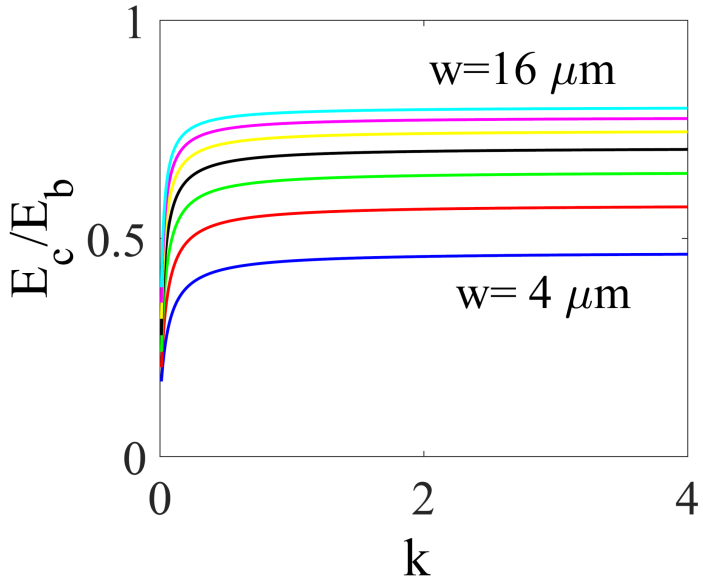

(a)

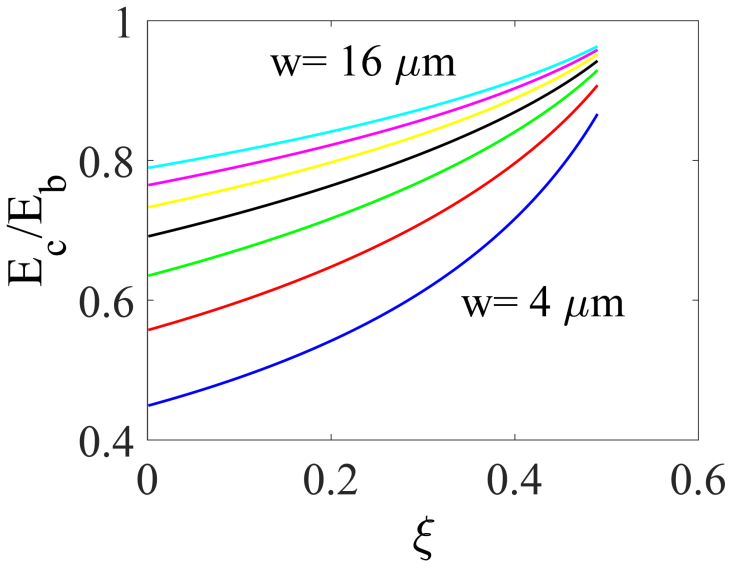

(b)

Figure 4.3: (a) Effect of increasing κ for $\xi = 0.05$ on elastic modulus of nacre, (b) Effect of increasing ξ for $\kappa = 10$ on elastic modulus of nacre

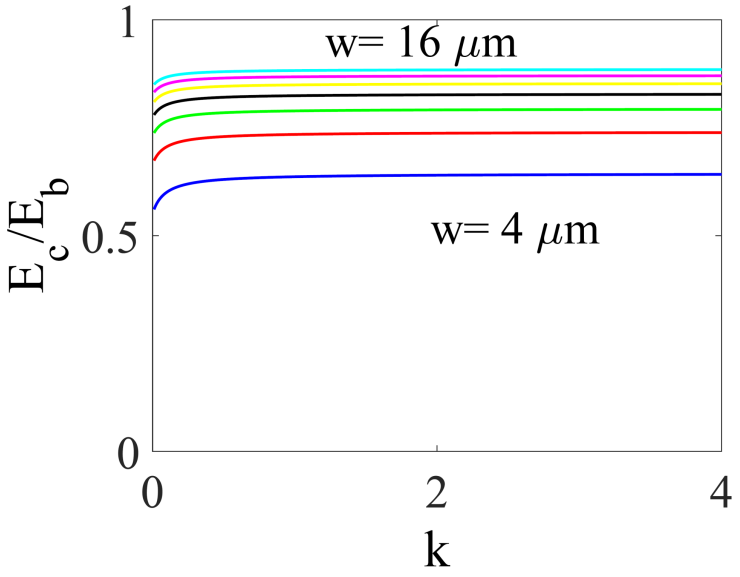

(a)

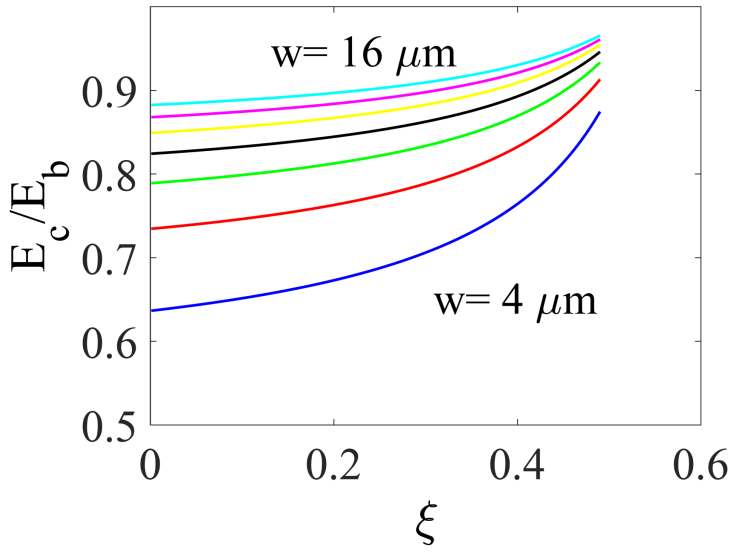

(b)

Figure 4.4: (a) Effect of increasing κ for $\xi = 0.05$ on elastic modulus of nacre, (b) Effect of increasing ξ for $\kappa = 10$ on elastic modulus of nacre, considering 2.5 % volume percent of mineral bridges

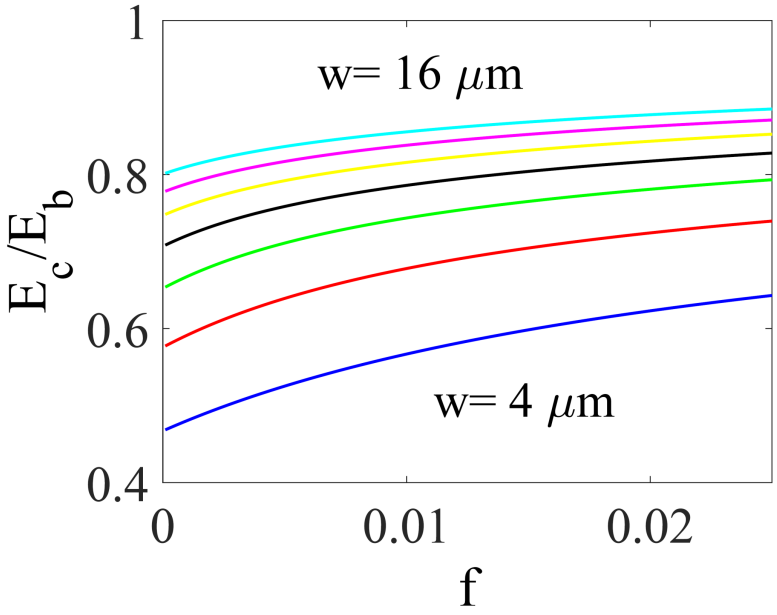

Figure 4.5: Effect of volume percent of mineral bridges on elastic modulus of nacre while $\xi = 0.05$ and $\kappa = 10$

failure event that, the stress in the bricks and horizontal interface should be found assuming the failed vertical interface ($\alpha = 0$); 4) If either of stresses in the brick or the horizontal interface (with $\alpha = 0$) is less than their strengths, the sample fails and the stress in vertical interface is the peak and failure stress; 5) If the stresses in the bricks and horizontal interfaces are smaller than their strengths, more strain can be applied to the sample; 6) Using the new modulus and the computed stresses in the elements, the failure strains of the brick and horizontal interface can be found. The stress corresponding to the minimum strain determines the failure stress; and 7) If this stress is more than the vertical interface failure stress, the obtained stress is the peak stress.

The results show that the proximity layer properties have relatively minor effect on the strength of nacreous materials. This is due to the point that the main factor in determining the strength of materials are the weakest links. With the assumed mechanical properties the regular protein is the weakest link and therefore is very similar for all the samples. With the calculated states of stress we are able to find the tensile toughness (area under stress-

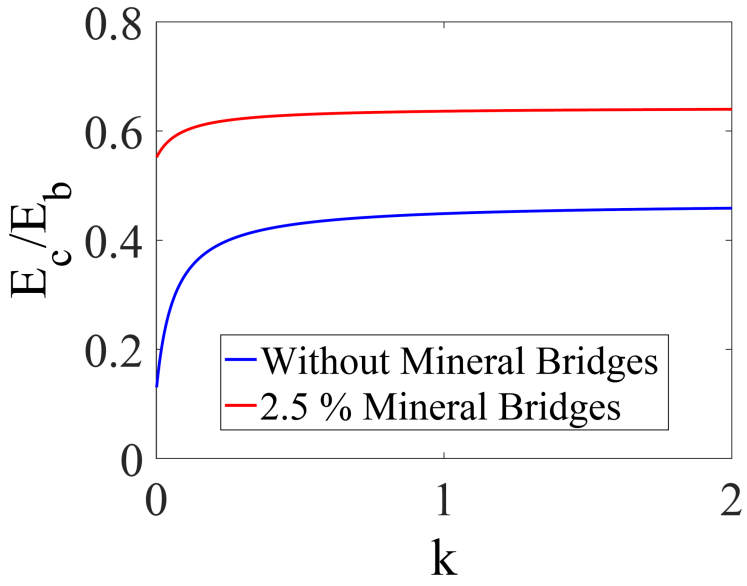

(a)

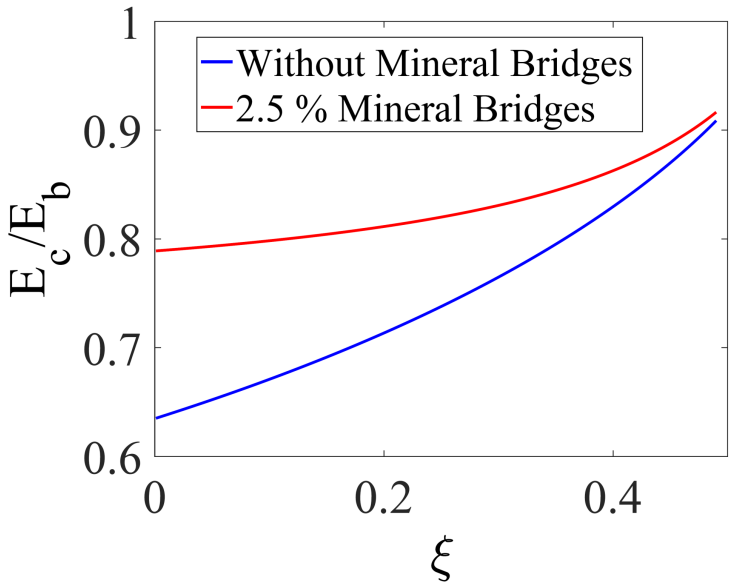

(b)

Figure 4.6: (a) Effect of increasing κ for $\xi = 0.05$ on elastic modulus of nacre, (b) Effect of increasing ξ for $\kappa = 10$ on elastic modulus of nacre, considering 2.5 % volume percent of mineral bridges

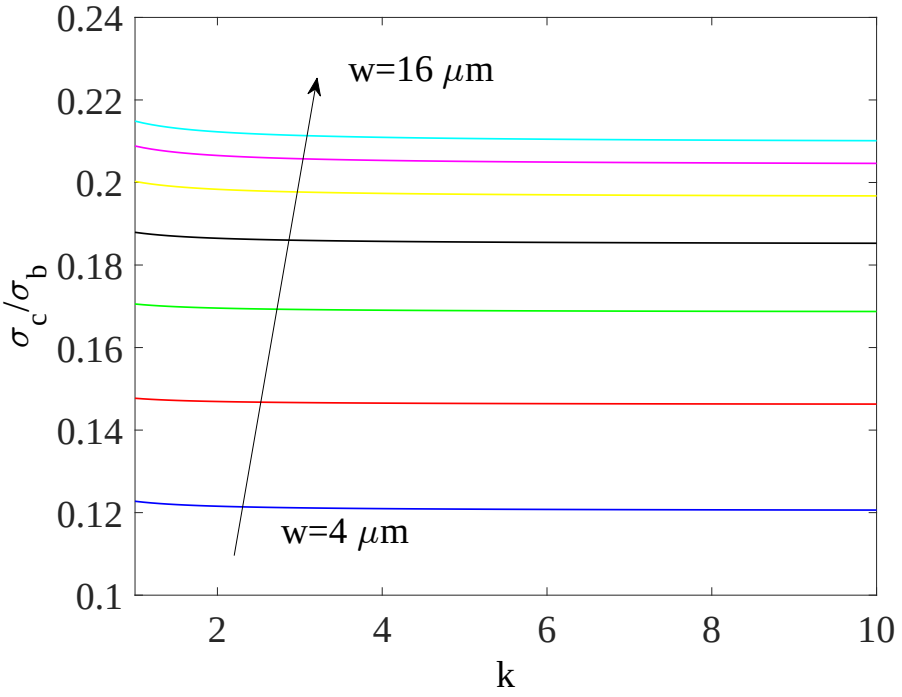

Figure 4.7: Effect of increasing κ for $\xi = 0.05$ on strength of nacre

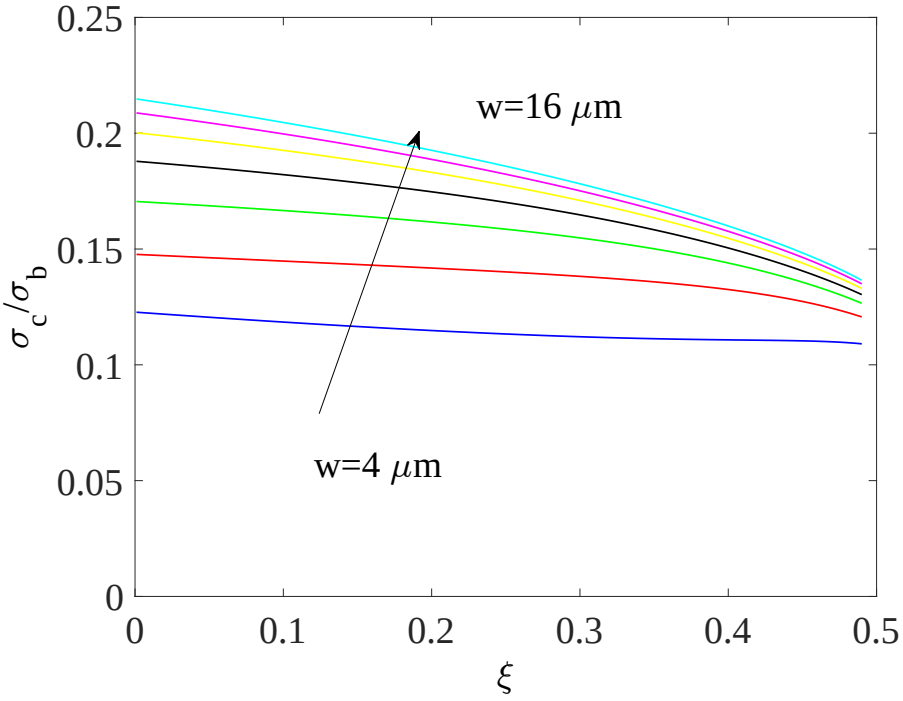

Figure 4.8: Effect of increasing ξ for $\kappa = 10$ on strength of nacre

strain curve) of the models.

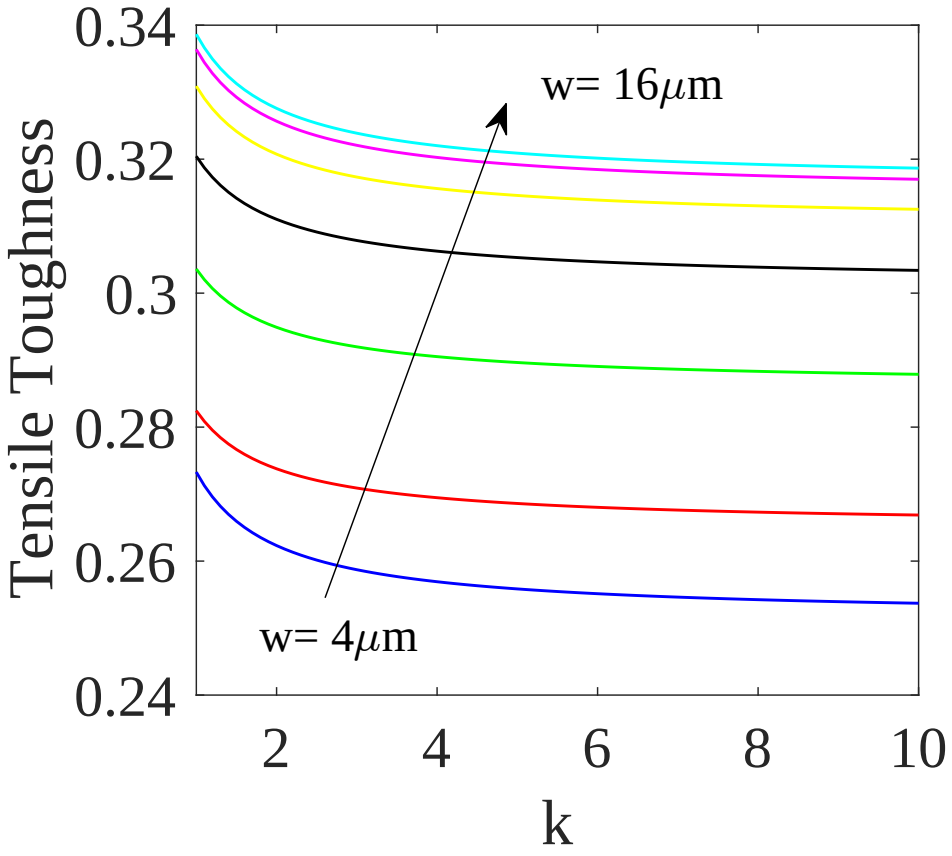

Figure 4.9: ffect of increasing κ for $\xi = 0.05$ on tensile toughness of nacre

The results clearly shows that increasing the thickness of proximity layer decreases the toughness of nacre. Hence, the effects of proximity layer properties on toughness and stiffness are mutually exclusive. Increasing proximity layer thickness, improves the elastic modulus, while it minutely decrease the toughness.

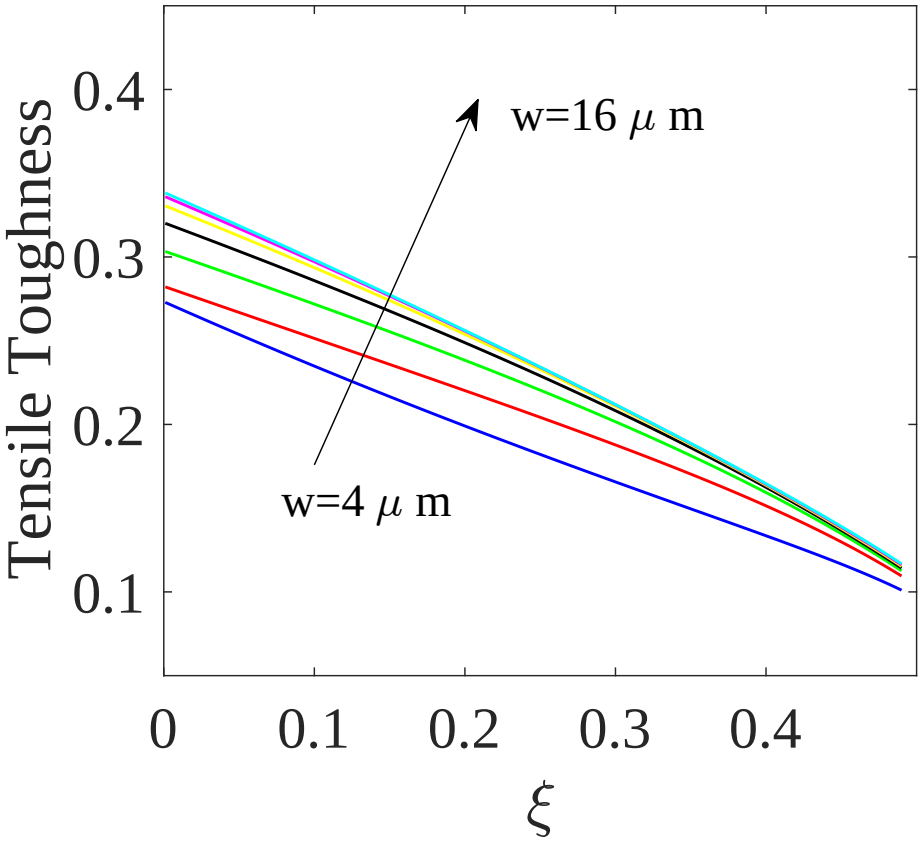

Figure 4.10: Effect of increasing ξ for $\kappa = 10$ on tensile toughness of nacre

4.4 Conclusion

The results of this chapter clarify how nacre solve the problem composites have in their constituents interfaces. Mineral proximity plays role on the mechanical response of the composite and significantly improve the effective mechanical properties of nacre. Moreover, the mineral bridges have a significant effect on the stiffness of the composite. This modulus study on these structures solve important mysteries about nacre and fills the gap between experiments and modeling of nacre. The proposed multilayered shear-lag model can be used to optimize the mechanical performance of nacreous materials.

5

Effect of Waviness in Mechanical Properties of Nacre

5.1 Introduction

One of the major contributions to nacre's impressive properties is the layering of the organic and inorganic components in a brick and mortar pattern, with the ceramic acting as the bricks (tablet) and the protein as the mortar. In a study done by Dimas et al. (2013) the behavior of hierarchical structures was investigated [89]. In that work they stated that adding more hierarchies and staggering the arrangements of mineral platelets contributed to the remarkable mechanical properties. They showed that a brick and mortar arrangement of stiff and soft material has a far more efficient usage of material in the presence of a flaw such as a crack. [103]. The staggering of the mineral tablets creates a system where the mineral platelets carry the tensile load and the mortar transfers the load between the mineral tablets [92]. However unlike a simple brick and mortar pattern, nacre has a waviness to its structure. This work centers on understanding the effect of the tablets' waviness on nacre's mechanical properties.

As seen in many biological materials, superior properties are achieved through complex architectures. Additive manufacturing or 3-D printing is an effective method to obtain irregular geometric shapes optimized for a need [161, 162, 163]. Different types of 3-D printing as well as their benefits and drawbacks are discussed in literature [164]. In this chapter, 3-D printing is employed to prototype samples with complex structure and aid in the

understanding of their mechanical properties. Materials that are independently weak are combined and arranged to create an impressive structure much stronger than its constituents [89]. It has been shown that one can use computer models to form arranged composites and showcase fracture properties, and then use 3-D printing to construct materials with such mechanical performance [89, 162].

Numerical modeling also plays an important role in finding nature's strategy in geometry optimization as well as understanding the mechanical response and deformation mechanisms in composite structure [103], [165], [62]. Finite element analysis is one of the powerful tools in investigating the effects of different features in biological composites and in particular nacre [96]. Finite element analysis can predict a material's response based on discretization of the material into finite elements that imitate a real environment. Often it is used to conduct complex experiments that would otherwise be extremely difficult or impossible to replicate in a lab [93]. In the study done by Katti et al. (2001), the 3-D finite element model was used to study nacre and the nanomechanical properties of the individual components. The effects of interface properties and specifically the asperities were studied using nanoindentation combined with finite element analysis in a study done by Barthelat at al. [66]. It is shown in the literature that every feature of the nacreous structure has an important role in mechanical response and deformation properties. Mineral bridges [79],[88], asperities and the organic matrix [143],[72] have different effects on stiffness, strength and toughness [102, 96, 123]. Moreover, there are numerous studies on the shape and properties of tablets and their role on the superior nacre properties [166].

One of the features that was discovered later in the nacre studies was that the bricks are not flat and that there is a waviness in the organic interface. Different experimental materials science techniques such as Scanning Electron Microscopy (SEM), Transmission Electron Microscopy (TEM), Atomic Force Microscopy (AFM), laser profilometry and optical microscopy were used to prove this theory [65]. The tablets' waviness acts as obstacles to tablet sliding and hence causes more energy dissipation. Another study by Valashani et al. (2015) used a laser engraving technique to make nacre-like materials where glass acts as the brick and polyurethane acts as the matrix [129]. They studied waviness as a geometrical locking within the mechanical response of the brick and mortar structure. Their results show that increasing the tablet locking angle increases the strength of the samples while the energy dissipation drops after an increase [129]. Considering all these efforts, more

numerical and experimental studies are needed to guarantee a better understanding of the deformation mechanisms of the samples with wavy tablets in order to improve the performance of designed advanced composites.

In this chapter, we focus on the effects of the tablet's waviness and try to develop a systematic method to demonstrate the role of waviness in the energy dissipation and damage tolerance of nacreous materials. Both finite element method and 3-D printing were used in this study. Simple brick and mortar composites were compared with several bowtie shaped brick and mortar composites with different bowtie angles. The main effort in this method is to keep the volume percentage of the constituents constant in all the models and prototypes. This helps to figure out the single effect of tablets waviness by eliminating other variables such as the tablets volume fraction. The results of this study can be used in designing advanced brick and mortar composites.

5.2 Materials and Methods

5.2.1 Mechanical Response of Composite Constituents

In this study two approaches were used to study the effect of tablet waviness and waviness angle on the mechanical properties of nacre-like structures. In the experimental phase, we used 3-D printing to make samples with structures that will be explained in the following sections. In order to mimic nacre and combine a stiff and a soft material to make the samples, two available commercial materials in the Object 3-D printer were used to make the composite specimens. The mortar was assigned a stretchy black rubber material called Tango Black Plus to replicate the mortar found in natural nacre and the brick was assigned a white rigid polymer called Vero White Plus. Tensile tests were performed on these materials in order to have a clear idea about their mechanical behavior. The mechanical properties of these constituents can be extracted from their stress-strain curves, Fig. 5.1.

Similar mechanical setup and material properties were used in the finite element analysis. The mechanical response of the constituents is shown in Fig. 5.2. In this study, this behavior is named elastic-plastic-rupture. The mechanical properties obtained from the experiments on the constituents were estimated and inputted for the finite element analysis. The Young's modulus was set to 1 MPa and the Poisson's ratio was set to 0.4 for the

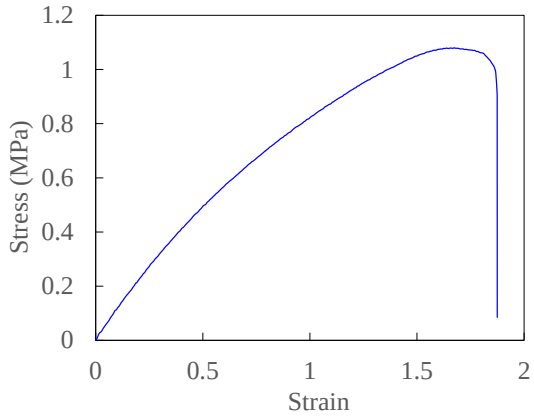

(a) Mortar

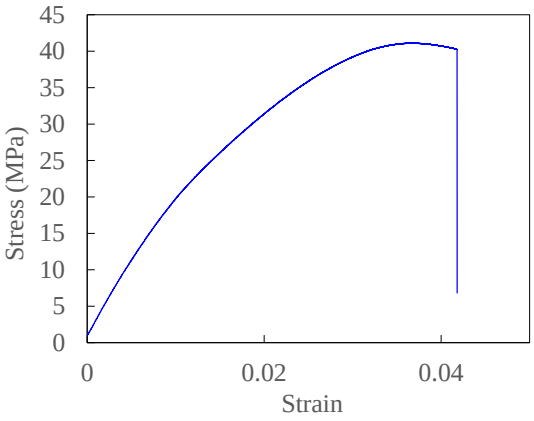

(b) Brick

Figure 5.1: The mechanical response of (a) Tango Black polymer (Mortar) (b) Vero White polymer under tensile testing.

polymeric mortar to imitate the soft layer in a model bioinspired multilayered material. For the bricks, the Young's modulus is measured to be about 1.2 GPa and the Poisson's ratio s measured to be about 0.3 to replicate the hard phase in nacre. The strength of the mortar is about 1 MPa and the strength of the brick is about 40 MPa.

The ductile damage model was applied to simulate the behavior of brick and mortar. In this damage model, the onset of failure is predicted by a damage initiation criterion in which the material stiffness is degraded when the criteria is met. At a specific time step the material's stress tensor is given by the damage formula,

$$\sigma = (1 - D)\bar{\sigma} \tag{5.1}$$

where D is the damage variable and $\bar{\sigma}$ is the initial stress tensor in each increment assuming the damage is not present. A value of 1.0 or higher for D represents that the material is not able to carry load anymore and an element will be removed from the mesh if the value of D exceeds the value of 1.0 in all of its integration points. The properties used for numerical analysis is tabulated in the following table. The fracture strain parameter is chosen such that the numerical fracture stress and strength for one element agrees with the experimental fracture stress and strength.

Table 5.1: Mechanical properties of materials used in numerical analysis.

Material	Modulus (MPa)	Fracture Strain	Tensile Strength (MPa)
Mortar Phase	0.67	1.9	1
Brick Phase	1200	0.045	40

5.2.2 Unit-cell Finite Element Analysis

To compare how the brick and mortar structure impacts strength and stiffness, three models were created and put through tensile boundary conditions. Finite element analysis was used to study the various structural models of nacreous structure. These models differed in terms of the brick shape and the thickness of the mortar. An important consistency among all the models is the brick volume fraction of 80.13%; this allows the models to be comparable and allow accurate conclusions to be drawn. Due to the 3-D printer limitations, the thickness of bricks is assumed to be 1 mm and the thickness of mortar around 0.12mm - 0.2 mm (varies slightly for different models).

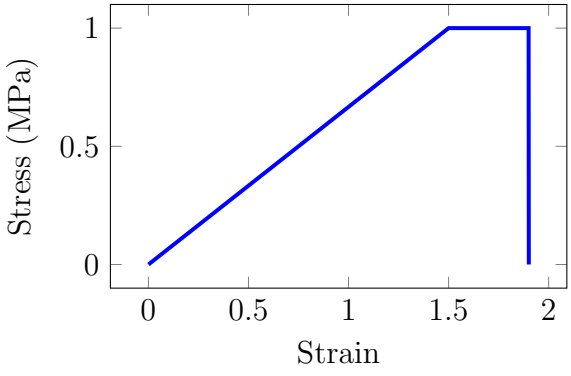

(a) Mortar

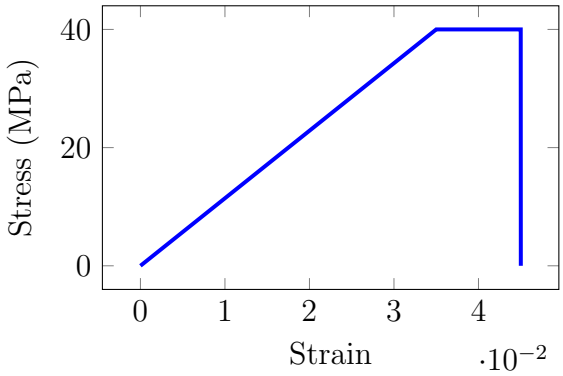

(b) Brick

Figure 5.2: Mechanical behavior of (a) Mortar and (b) Brick assumed to conduct finite element simulations

Hence, the volume percentage of the bricks was determined in the simple brick and mortar structure and then carried throughout the rest of the models. We changed the rectangular cross-section of the bricks to a bowtie shape to create the tablets with waviness. Fig. 5.3 shows the different unit-cell structures designed in this study. These shapes were considered to incorporate the waviness found in nacreous structures. The model called "Wavy" in our study has the first level of waviness. The narrowest part in the tablets thickness is 0.8 mm and the widest is 1 mm. The mortar thickness in this model is calculated to be 0.181 mm in order to maintain the volume fraction of 80.13 % for bricks. The next one is pinched even more so that the narrowest part reduces to 0.6 mm. The mortar thickness in this design is 0.163 mm and is called "Super Wavy." The next level of waviness, used and designed in our study is called "Exaggerated Wavy" with the narrowest part being 0.4 mm and a mortar thickness of 0.147 mm. Finally, the most wavy tablets have the narrowest part of 0.2 mm and is called "Bowtie". In these samples, the mortar thickness is 0.128 mm. Moreover, in order to investigate the effect of overlap of tablets, specimens with "Asymmetric overlap" were designed and fabricated.This leads to a asymmetric shape of tablets in which the pinched section is located about 25% of the length away from the right side, as opposed to the previous models where it was located in the center of the brick. In these models all the tablets had dimensions of 5x1 mm, only the center width and mortar thickness changed between models.

5.2.3 3-D Printed Samples

3-D printed samples with the mentioned unit-cell structure were made using an Objet 3-D printer. The models were given dog-bone ends in order to follow ASTM standards with appropriate dimensions for tensile testing as shown in Figure 5.4a. These models were then 3-D printed and images of the samples can be seen in Figure 5.4b. Three samples were printed from each design. Once the models were printed they were individually tensile tested using Instron 5567A (Instron, Norwood, MA, USA) servo-hydraulic system. They were stretched at a rate of 0.1 mm per minute until the breaking point was reached. From these tests a force-displacement graphs were retrieved. Strain gages were used to determine the elastic modulus of the samples.

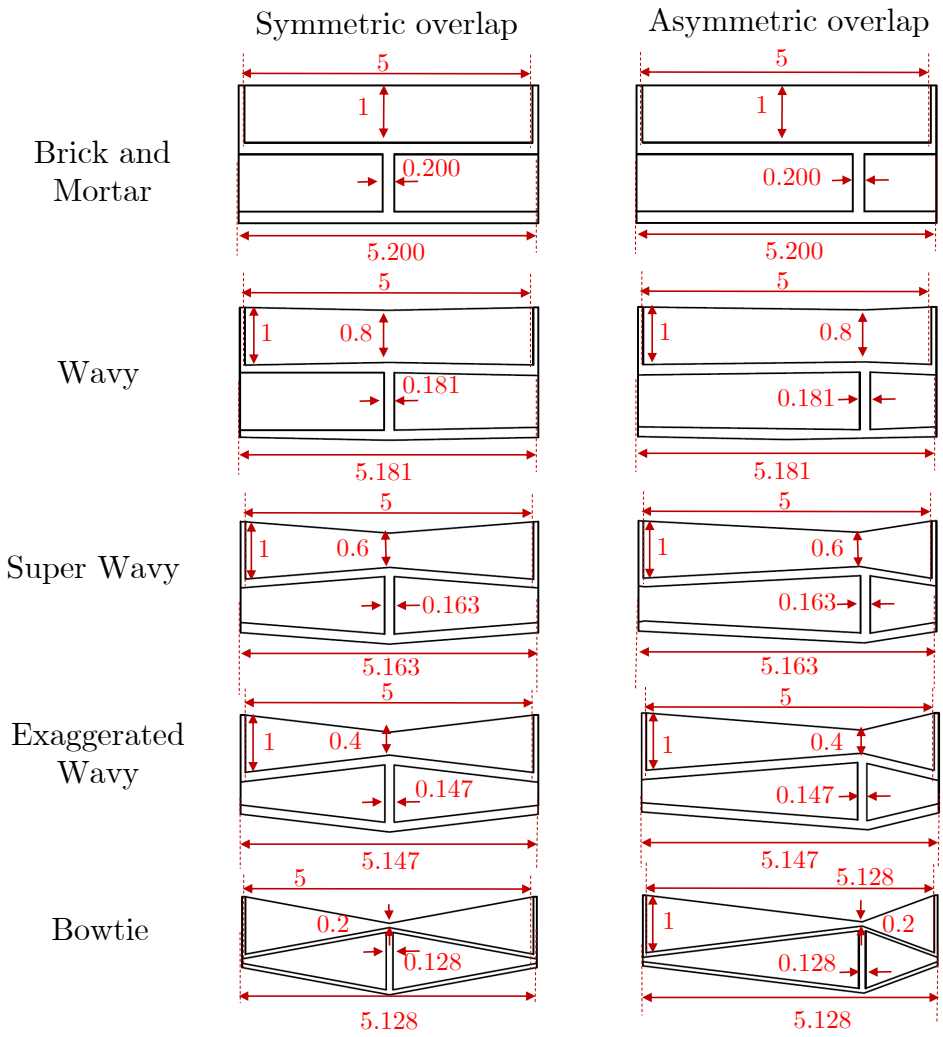

Figure 5.3: The unit-cell geometry of the samples with symmetric and asymmetric tablet overlaps.

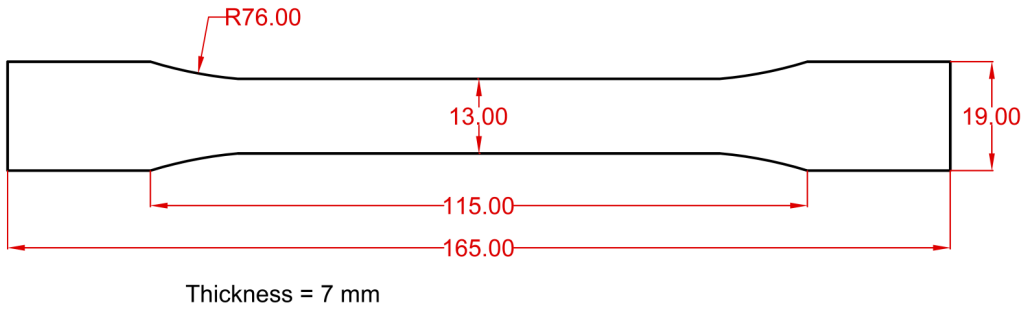

(a)

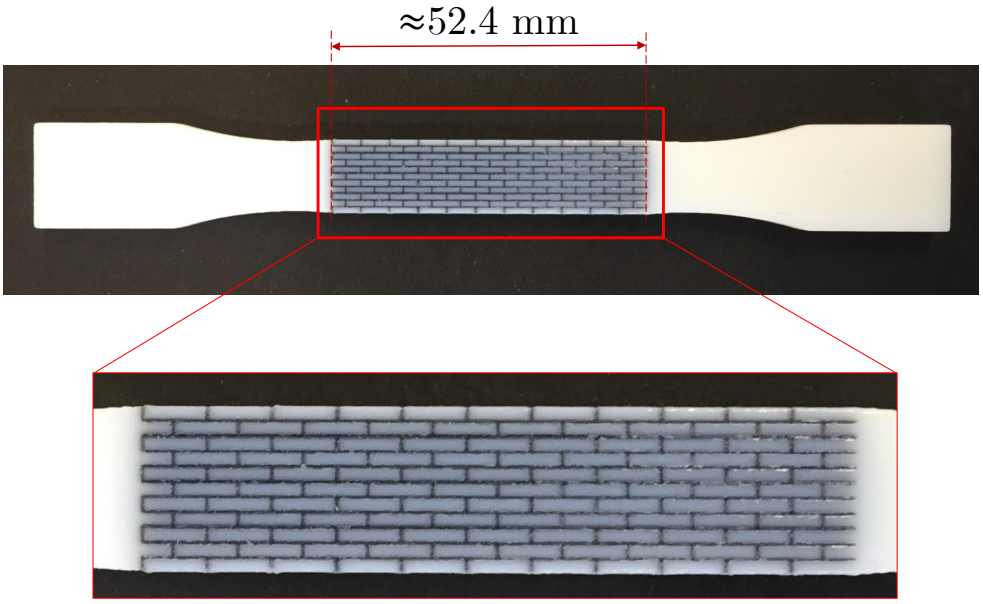

(b)

Figure 5.4: (a) Schematic of ASTM D368 standard dimentions to make samples for tensile testing, (b) A typical sample 3-D printed according to the ASTM standard

5.2.4 Super-cell Finite Element Model

In the first round of testing all the models were given the dimensions of 10x11 tablets. Fig. 5.3 shows the unit-cell structure for the different models. For each case, the left side of the model was held fixed and the right side was stretched. The tensile test modeling were continued till the vertical interfaces fail. Afterwards, the stresses in the vertical interfaces was assumed zero and the rest of displacements were applied (same loading rate) untill the horizontal interfaces also failed. After each test the stress-strain graphs were obtained and the stiffness for each model was derived by dividing the stress by the strain. Stress is defined as the reaction force divided by the width and strain is defined as displacement over length.

5.3 Results and Discussion

5.3.1 Unit-cell Analysis

Two-dimensional finite-element models of different unit cells were constructed using a commercial software. Unit cells were composed of two different materials which were considered as isotropic materials with the same parameters reported previously. The unit cells are analyzed using "Elastic-Plastic-Rupture" mechanical response of the constituents in order to give an idea about the failure sequence of the elements.

The results of the five different unit cells with symmetric overlaps are shown in Fig. 5.5. In the first part of the curve, the whole structure is in elastic regime. Then, there is a reduction in slope which represents the plasticity of the vertical interfaces. After that the vertical interface completely fails and causes a significant drop in the stress-strain curve. Then the stresses in the vertical interfaces were assigned to be zero and the models were rerun to capture the next sequence of events. The stress increased in the horizontal interfaces before the second reduction in the slope. This event indicates that the horizontal interfaces in the mortar have undergone plastic deformation as well. Since the vertical interfaces have smaller lengths in comparison to the horizontal sections, under an applied displacement, the vertical interfaces undergo a large strain and are therefore the first part to fail. The horizontal sections in the mortar experience a smaller strain due to their larger length and fail after the vertical parts. In this approach the material will undergo a plastic deformations before rupture which is much

more realistic than elastic-plastic assumption. In this case, the vertical and horizontal interfaces will break before the whole section yields which means that the total plastic deformation will be much less than elastic-perfect plastic assumption. The first drop on this plot stands for the vertical interface failure while the second drop represents the horizontal interface failure (or brick failure in some cases). It can be seen that the bowtie configuration results in a higher modulus, strength and toughness of the unit cell.

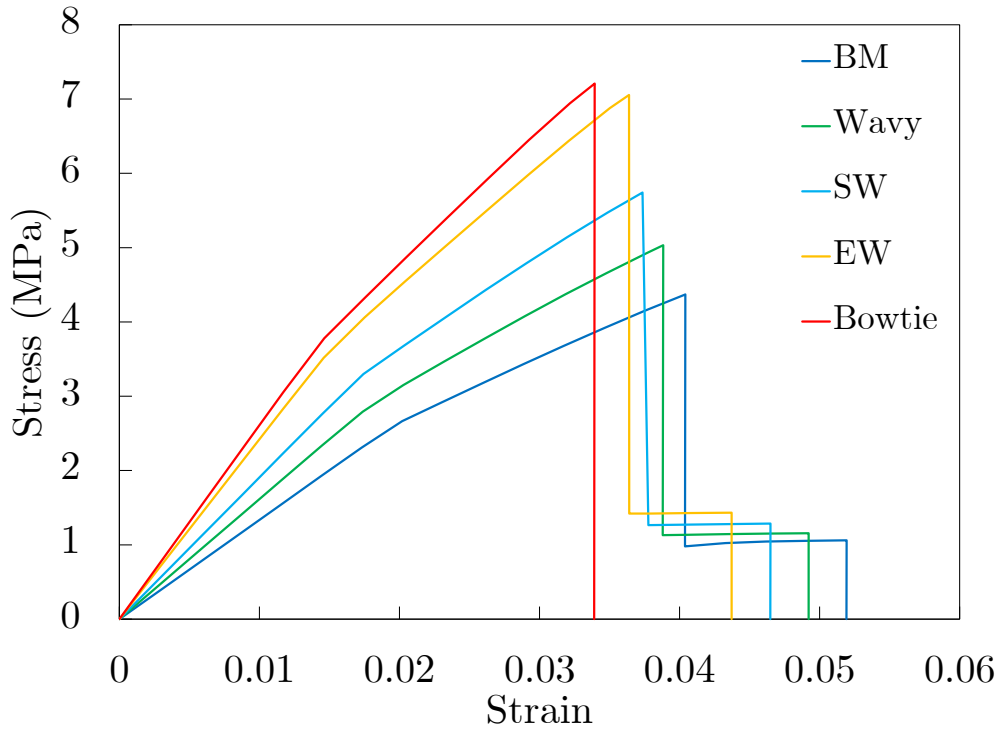

Figure 5.5: Stress-strain comparison of the unit-cell finite element simulations

5.3.2 Mechanical Testing on the 3-D Printed Samples

Tensile tests were performed on ten designs (three samples for each design). Figure 5.6 compares the typical stress-strain curves of the samples with different levels of waviness under tensile testing experiments. There are interesting points that can be obtained from the results. First, the results show that

increasing the waviness angle in the brick and mortar structure, increases the stiffness. This trend can be observed in both symmetric and asymmetric overlap cases. Moreover, comparing the mechanical behaviour of samples with different overlaps, shows that increasing the tablets' overlap, increases the stiffness and strength of the samples. The most interesting phenomenon that is observed in the results and clarifies the effect of tablet's waviness more is the different mechanical behaviour of exaggerated wavy and bowtie samples (symmetric overlap) with other samples. In these samples, the tablets interlocking is high so that the layers are not able to past each other. In exaggerated wavy samples, interlocking increases the stiffness and strength, however transfers a high portion of load to the bricks and causes their failure. In this case the failure is catastrophic. In bowtie samples, the effect of stress concentration due to the sharp edge in the bricks adds up to the transferred load and subsequently, the samples break in lower stresses. These events drastically affect the toughness of the samples.

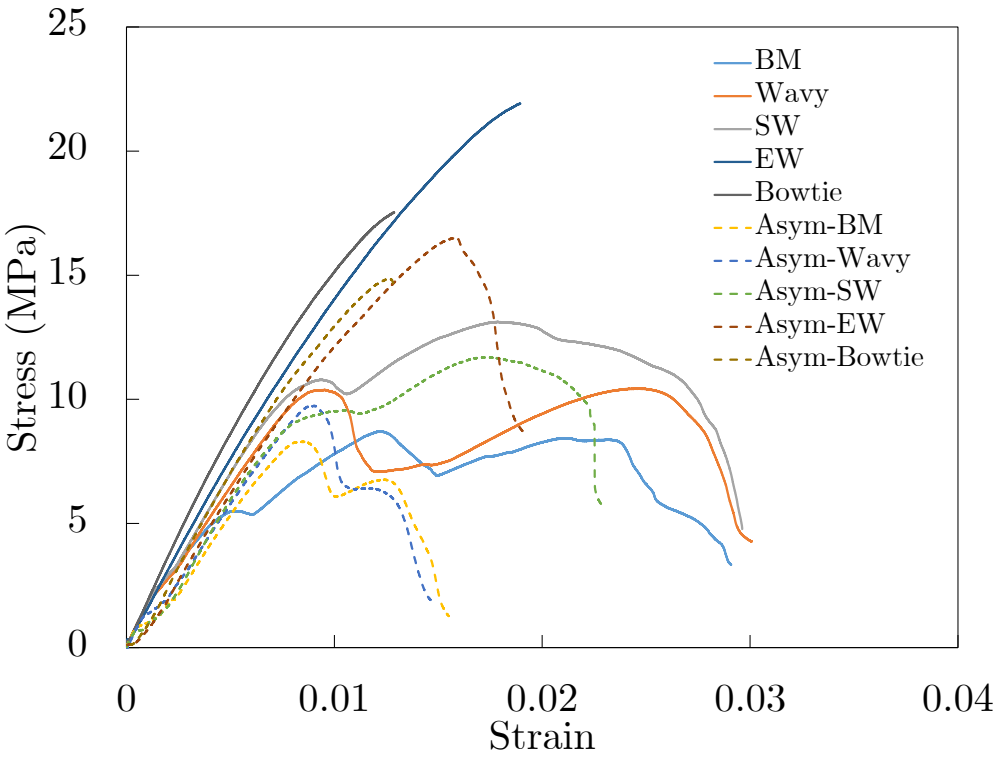

Figure 5.6: Stress-strain comparison of the 3-D printed samples

The failure pattern of the samples indicates the difference between the nature of failure in samples with exaggerated wavy tablets and other samples. The typical failure sequence in the 3-D printed samples is shown in Fig. 5.7. The layer sliding and gradual failure of horizontal interfaces is completely clear in the samples except the exaggerated wavy and bowtie ones. This phenomenon causes a lot of energy dissipation and subsequently high ductility and toughness.

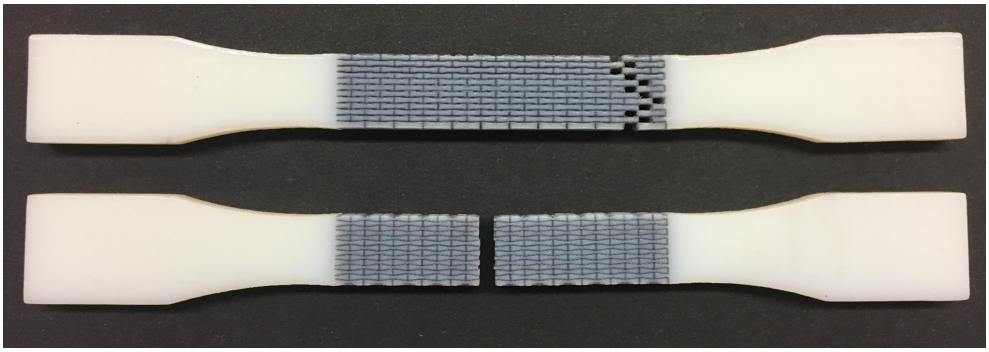

Figure 5.7: Stress-strain comparison of the samples

5.3.3 Super-cell Finite Element Model

After the creation of the models, static testing ensued. Fig. 5.8 shows a typical stress distribution in the samples in the early stages of deformation as well as the failure sequences of the elements. In the design with the exaggerated wavy tablets, the strength of bricks determined the strength and the nature of Load-Displacement curve; however in the other samples, they are determined by the stress in the mortar phase. The exact same phenomena and trends observed in the experimental analysis can be found in the numerical analysis. However, the numbers are a little different which are due to the flaws in the sample manufacturing. Comparing the stress in Fig. 5.8 it is show that as the waviness increases the stress concentration in the tablets increases. This may cause brick failure if the matrix is too strong and does not fail before reaching that stress.

The results show that the elastic modulus increases as the waviness level increases. However, for strength and toughness there is an optimum design

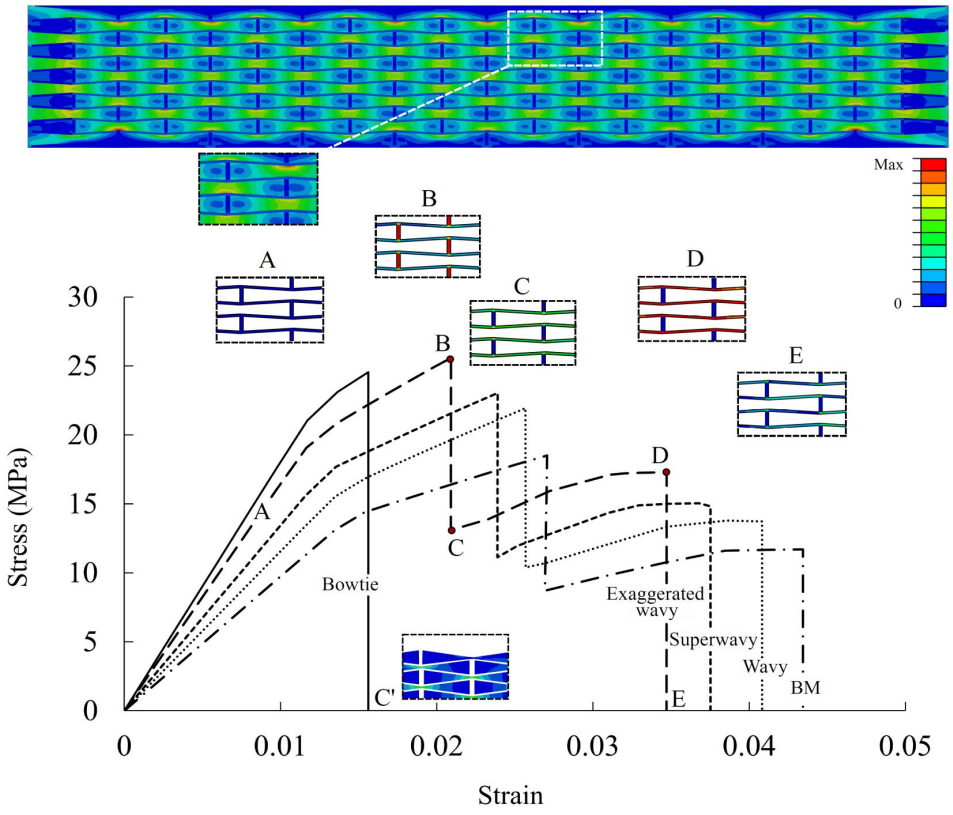

Figure 5.8: The comparison between stress-strain behaviour of samples obtained by finite element simulations

based on the mechanical properties of the constituents. Our modeling approach is capable of accurately capturing the mechanical properties of the multimaterial 3D printed samples. When the waviness level passes a certain limit, the interlocking effect prevents the energy dissipation through tablet sliding which decreases the toughness. Moreover, another effect that act against the improvement of mechanical performance is the stress concentration in the tablets which cause a sudden failure in the tablets and consequently in the samples.

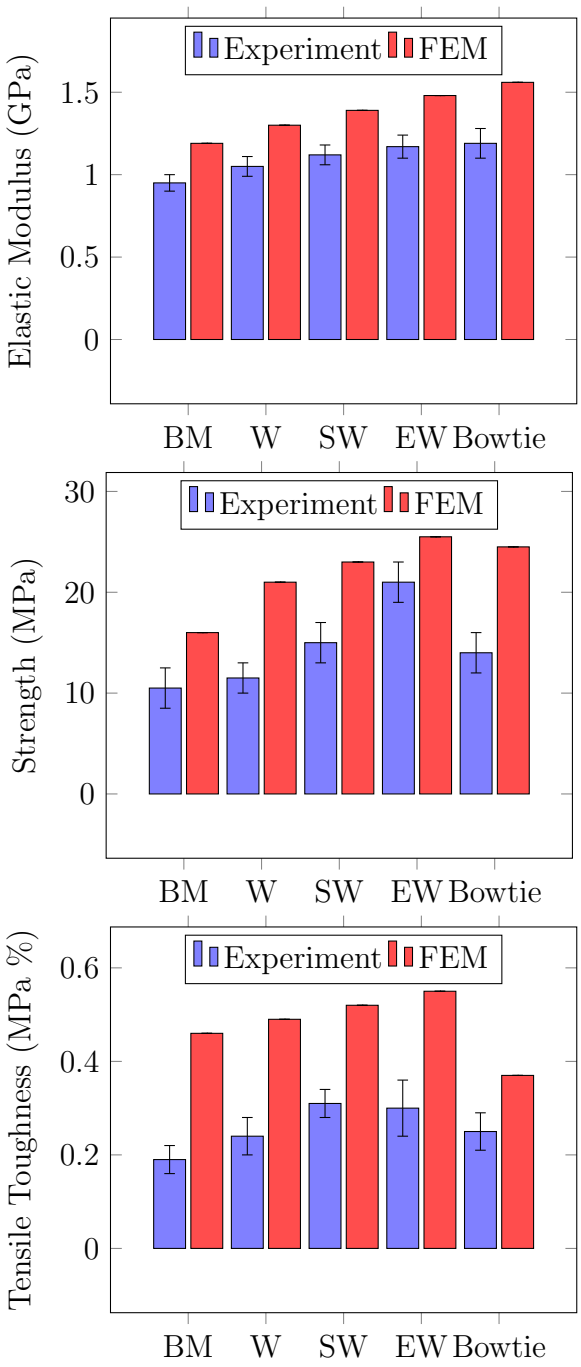

Figure 5.9: A comparison between the various mechanical properties of samples with different waviness level in experiments and numerical analysis

5.4 Conclusion

Biologists, material scientists and solid mechanicians have been working on different theories to explain all the mechanisms responsible for the superior mechanical properties of nacre as a model hard/soft multilayered composite.

Obviously, there are numerous factors that work synergistically to boost the toughness, strength, and stiffness of nacre. One of these factors is the waviness in the platelets since they are thicker in the outer edge than the core. In this study we systematically investigated the effect of this waviness in the tablets by making finite element models and 3-D printed samples.

We consistently kept the volume of fraction of the constituent materials exactly the same in order to be able to compare the mechanical behavior of samples, and to evaluate the pure effect of tablet waviness on their response. Hence, all the dimensions except the thickness of mortar were kept identical. We played with the mortar thickness to adjust the volume fractions in the system. Moreover, ASTM standards for tensile testing of elastomers were used to make the 3-D printed samples.

Our results show that the platelet waviness is extremely effective in increasing the stiffness of brick and mortar structure. Platelet waviness has relatively high impact on the strength and toughness of these multilayered materials, and affects their energy dissipation mechanisms. Out exaggerated waviness structure exhibit the most optimum structure with respect to stiffness, strength and toughness. In the experimental results, we observed that the exaggerated waviness may cause tablet failure followed by a dramatic stress drop. However, this event happens after causing a lot of energy dissipation in the system. Overall we have clearly shown than that a slight waviness in the tablets significantly improve the stiffness, strength and toughness. This results and the research method can be used to design tougher multilayered composites with different combination of constituents.

6

Fracture Properties of Bamboo

6.1 Introduction

There are many experimental studies on bamboo, including measuring strength, Young's modulus of matrix and fiber, and through analysis of microstructures and fiber distribution [167]-[170]. In a recent study by Dixon et al., the flexural properties of Moso bamboo in the axial direction, along with the compressive strengths in the axial and transverse directions were measured. Based on the microstructural variations and solid cell wall properties, analytical models of mechanical properties of bamboo which describe the experimental results were developed [23]. Numerical methods such as the finite element method (FEM) can be useful in understanding the mechanical behavior of composite materials in general[102, 171]. Considering that bamboo is an inhomogeneous orthotropic material, complex methods were used to investigate its properties numerically [12, 24, 172, 173]. Moreover, in order to estimate how the microstructure influences the effective properties of these materials, multiscale methods such as homogenization can be used [174]-[176]. Another approach to model bamboo is to employ a homogeneous, averaged value of Young's modulus, allowing comparisons and demonstrating the limitations of simplified procedures.

This paper presents the results of a combined experimental and theoretical/computational study of the resistance-curve behavior of Moso Culm bamboo. In this study, the hierarchical structure of bamboo is described using multi-scale images of structure between the micro- and macro-scales. This is followed by a section in which the experimental fracture resistance-

curve measurements are described. Then, the experimental results are elucidated before presenting theoretical/computational models for the estimation of resistance-curve behavior. Hence, the main goal of this study is to explain the basic deformation and toughening mechanisms for mixed mode fracture of bamboo using experimental and numerical methods. The implications are described and the conclusions can be used as a guide to design and make bio-inspired fracture-resistant composites.

6.2 Materials and Methods

The specific material studied in this paper is Moso Bamboo. Samples of the bamboo were obtained to study the microstructure, the fracture properties and crack resistance behavior. The bamboo samples were approximately five years old. The samples were cut from a bamboo culm with the following dimension: width, W = 8.0 mm; height, H = 8.0 mm and length, L = 56.0 mm.

Microstructural information is pivotal in understating the fracture properties and toughening mechanisms in composite materials. Thus, sections of bamboo specimens were cut with Beuhler diamond cutter and polished down to a 1 μm surface finish with Beuhler polisher and aluminum carbide abrasive (course to fine grit sizes). Then the samples were cleansed by acetone and menthol. The prepared samples were viewed under the optical microscope. In addition, image analysis was performed in order to characterize the mesoscale distribution of fiber bundles across the bamboo culm wall thickness.

Fig. 6.1 shows the structures of the bamboo obtained by optical microscopy. These images show bamboo structure consisting of bundles of vascular fibers in a matrix of primarily parenchyma cells. Most significantly, the microstructure is highly graded in that the volume fraction of the fibers increases from the inside to outside, the latter being the part that is exposed to the atmosphere or environment. The volume fraction of fibers across the thickness of the bamboo culm from the outer surface to the inner surface is computed from the optical images and presented in Fig. 6.2. These three regions can be classified as high fiber density region (at and near the outer surface of the culm), low fiber density region (at and near inner surface of the culm) and the medium fiber density region (in between the two).

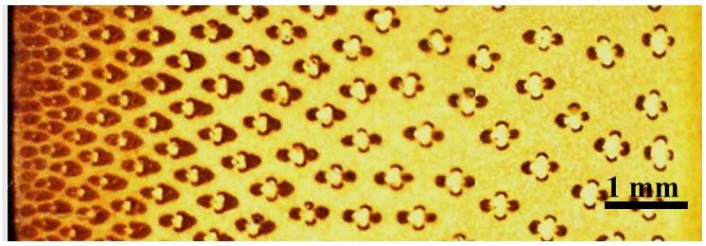

Figure 6.1: Optical microscopy image of the functionally graded microstructure of bamboo.

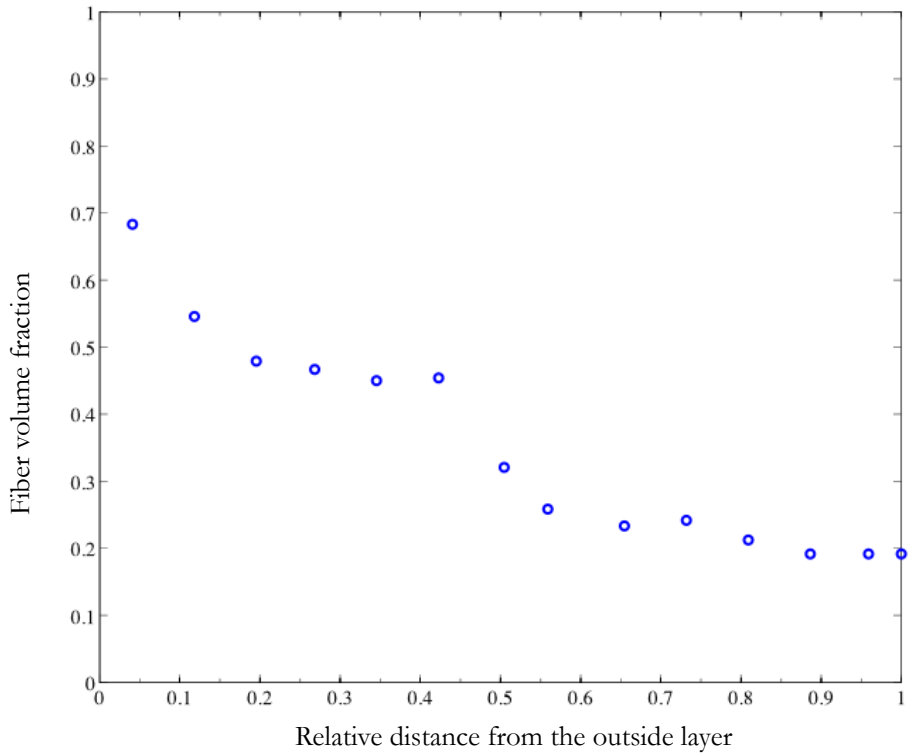

Figure 6.2: Dependence of fiber volume fraction on radial distance from the outer bamboo wall

6.2.1 Crack-Resistance Curve

Experimental Procedure

Constant moment crack growth resistance tests were performed on single edge notched bend (SENB) specimens of dimensions 8.0 mm × 8.0 mm × 56.0 mm. The specimens were notched at the centre with initial notch/height ratio, $d/h = 0.25$. The specimens were characterized into two categories, according to the placement of the notch. Specimens notched in the outer side of Longitudinal(L)/Tangential (θ) orientation are hereby referred to outside cracked, while those notched on inside part of the L/θ orientation are referred to as inside cracked.

Tests were carried out under four-point-bending using an Instron 8871 servo-hydraulic testing machine under constant loading rate. The outer and inner sample spans were 52.0 mm and 30.0 mm, respectively. Fig. 6.3 shows the schematic diagram of the test setup, sample and the loading condition. Testing was done under loading control. For each test peak loads were selected and loading ramped at a loading rate of 1 N/s. At each peak load, the crack extension/position was measured by a Quester Brandon High-Resolution Camera. This experimental setup is of particular interest, since the crack microstructure interaction can be observed readily with the microscope. Experimental data of applied loads and crack extensions were recorded for the analysis of the resistance-curve behavior of bamboo.

Finite Element Simulations

Three-dimensional finite element simulations were performed to extract the exact values of crack driving forces, J-integral; mode-I, K_I; mode-II, K_{II}; and mode-III, K_{III}, stress intensity factors for the four-point bending specimen. Using symmetry, only half of the beam was simulated and symmetrical boundary conditions were applied to the model. 20-node quadratic brick elements were used around the crack tip. In order to save computational time, a combination of 8-node brick and 6-node wedge elements were used to discretize the domain far from the crack tip, Fig. 6.4. Approximately 500,000 elements and 980,000 nodes were used to form the finite element model.

The material properties used in the finite element simulations are presented in Table 6.1. Fiber volume fractions as a function of thickness were extracted from the optical microscopy measurements. Later, classical rule of mixture was applied to estimate the actual graded elastic properties of

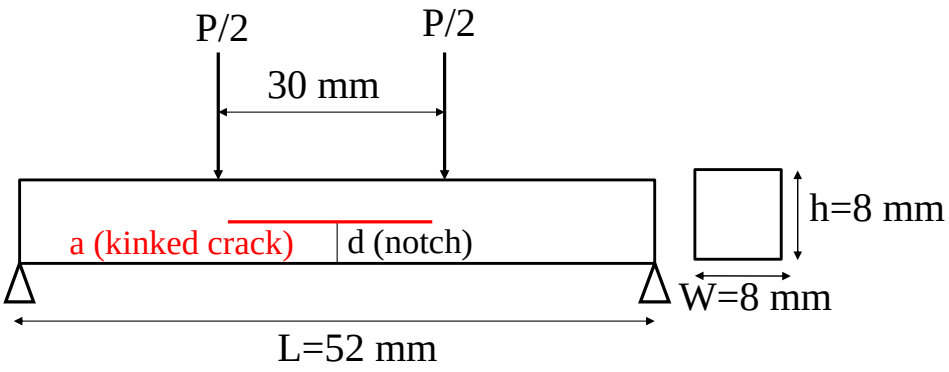

Figure 6.3: Schematic of the setup and beam cross-section for the four-point bending experiment.

bamboo microstructure as a function of distance from the outer layer. The estimate of bamboo Young's modulus as a function of the distance from the outer layers was applied to bamboo cross section in the finite element simulation, Fig. 6.5.

Table 6.1: Material properties of the constituents in Bamboo mesostructure.

Material	Young's Modulus	Poisson's Ratio
Fiber	36 GPa [177]	0.35 [38]
Matrix	500 MPa [168]	0.38 [178]

The computed contours of Mises stresses around a crack tip for a kinked crack size, a = 5 mm, are presented in Fig. 6.6. The resulting crack driving forces and stress intensity factors for a unit load are computed and plotted as a function of the beam depth in Figs. 6.7 and 6.8. As the crack size increases, mode-I and mode-II stress intensity factors and the resulting crack driving force, G, reach to a plateau in the middle of the beam. Meanwhile, mode-III stress intensity factors are zero for all crack sizes in the middle of the samples. These cross-sectional midpoint (max) mode-I and mode-II stress intensity factors were used in the calculation of mode mix and resistance curve behavior of bamboo. Mode mix (ψ) (sometimes called the phase angle

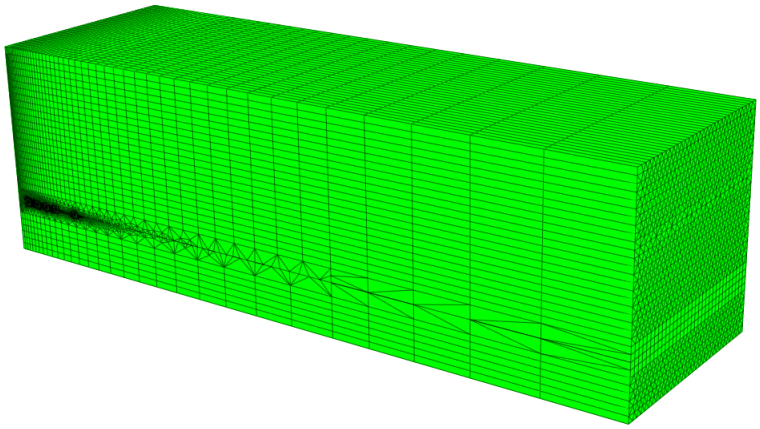

(a)

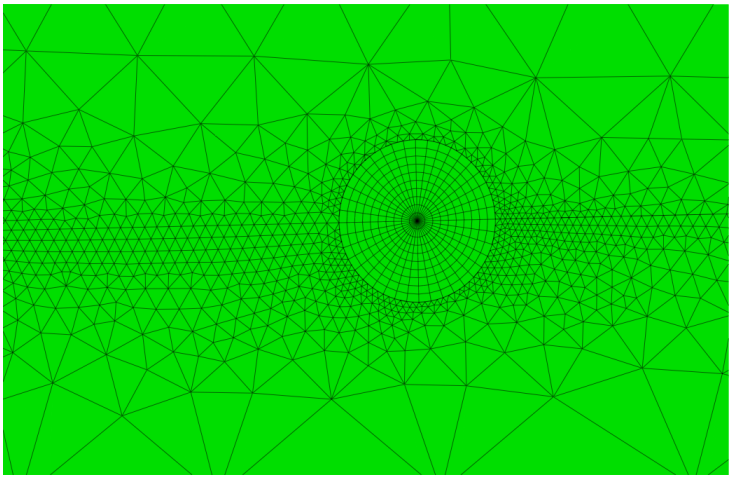

(b)

Figure 6.4: Finite element mesh for (a) the entire model and (b) around the crack tip.

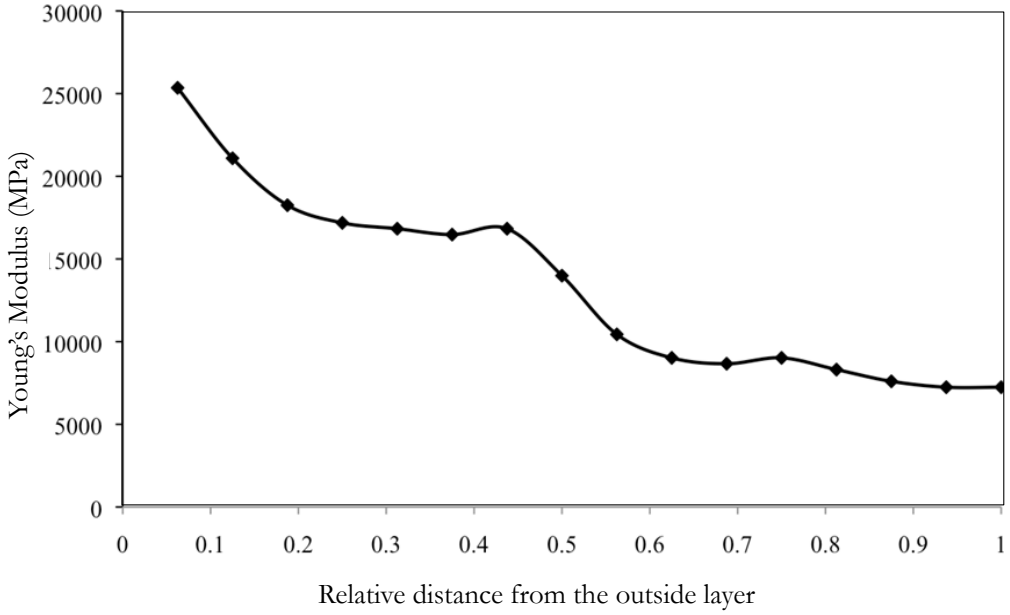

Figure 6.5: Variation of the Young's modulus along the cross-section of the bamboo specimen.

of fracture) is the relative proportions of tractions ahead of the crack tip in sliding mode (mode II) and opening mode (mode I) in the fracture (Eqn. 6.1).

$$tan\psi = \frac{K_{II}}{K_I} \tag{6.1}$$

The computed crack driving forces, stress intensity factors and mode mix as a function of crack length is presented in Figs. 6.9 - 6.11.

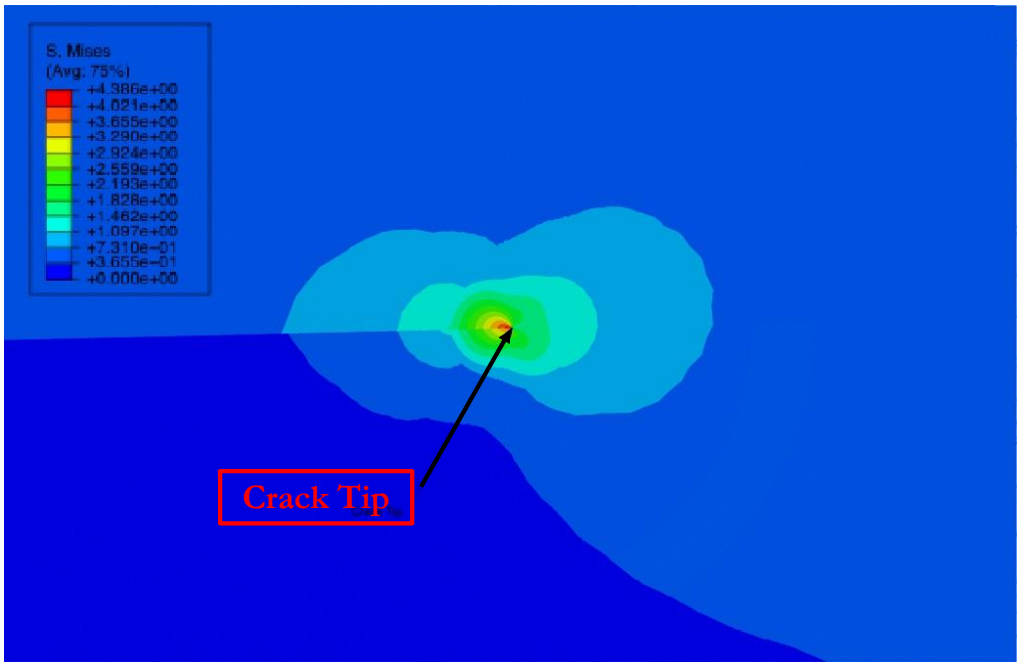

Figure 6.6: Contours of the Mises stresses around the crack tip of the size a = 5 mm.

Toughening models

The fracture toughness of a composite structure, toughened by the mechanism of crack-bridging, was first modeled by Budiansky et al. using elastic-

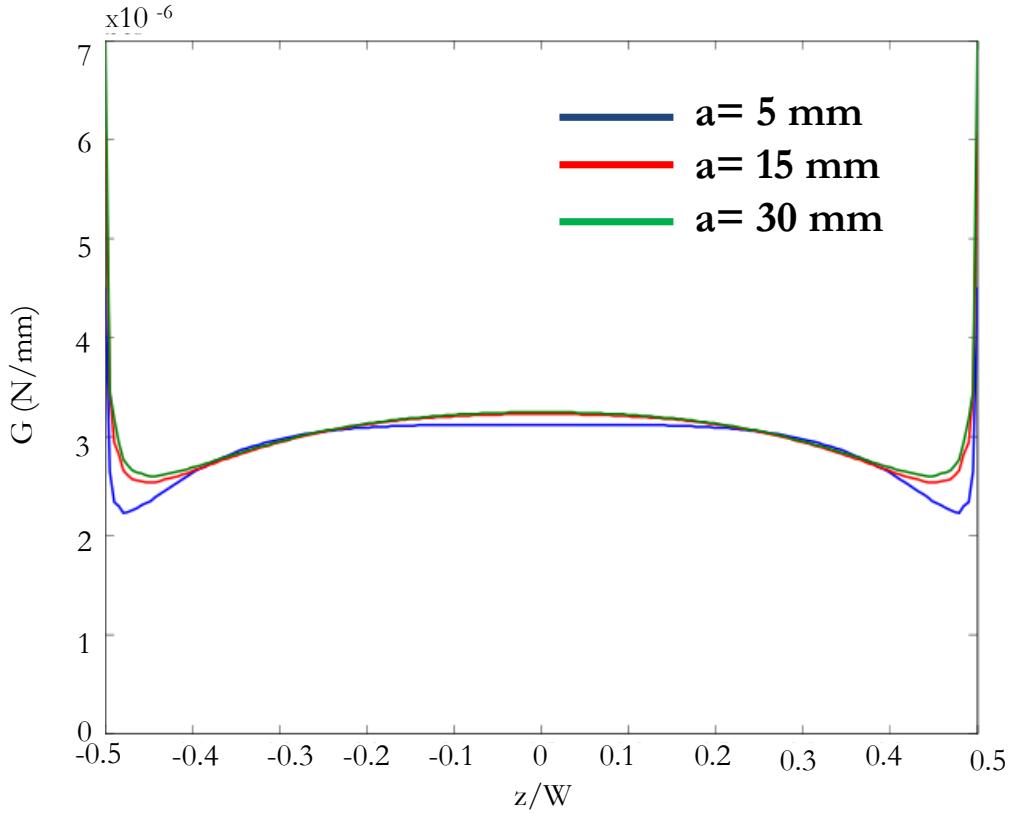

Figure 6.7: Variation of the crack driving force, G, of a three-dimensional crack in the cross-section of a four-point bend beam under unit load, 1 N.

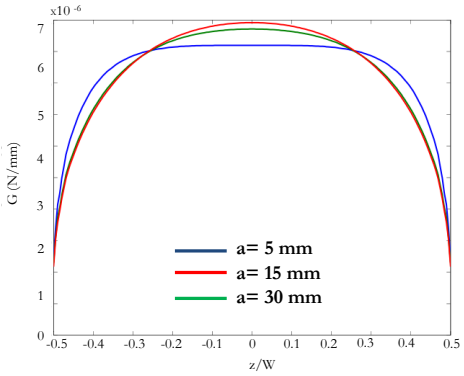

(a)

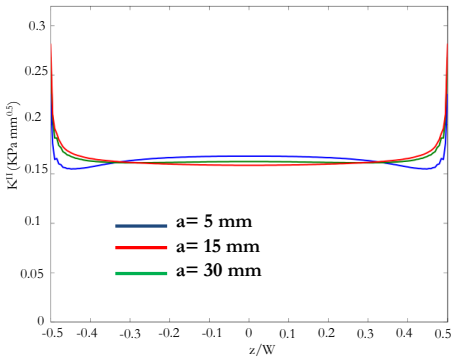

(b)

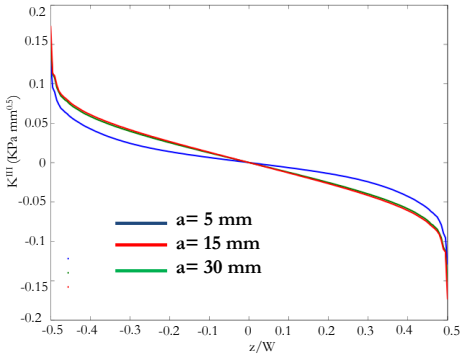

(c)

Figure 6.8: Variation of mode-I (a) and mode-II (b) and mode III (c) stress intensity factors as a function of the depth of the beam for an outside-notched specimen.

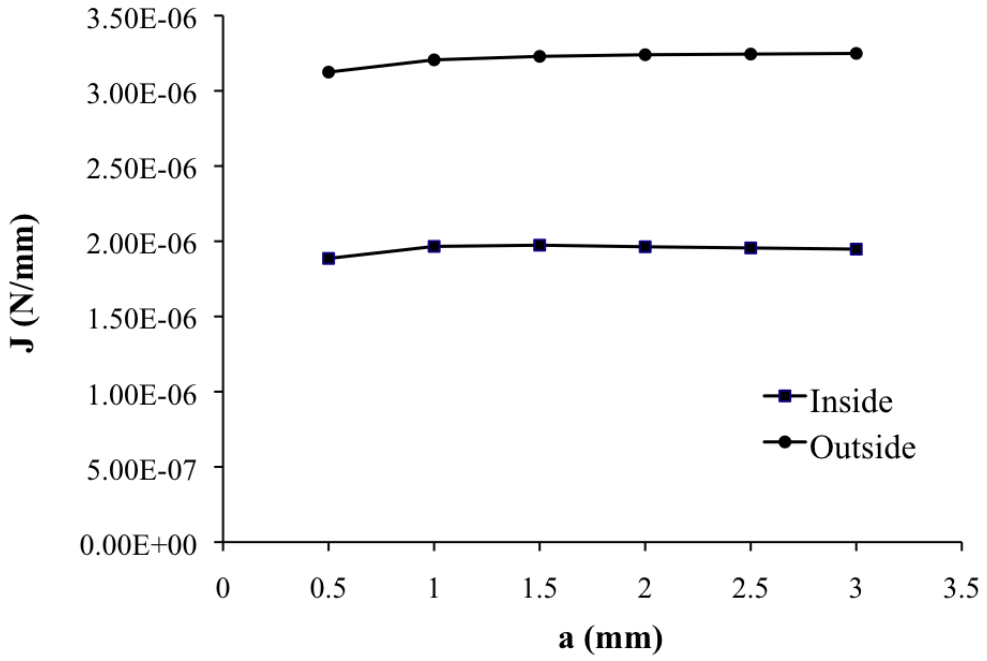

Figure 6.9: Variation of Crack Driving force, J-integral, for unit load as a function of the crack length.

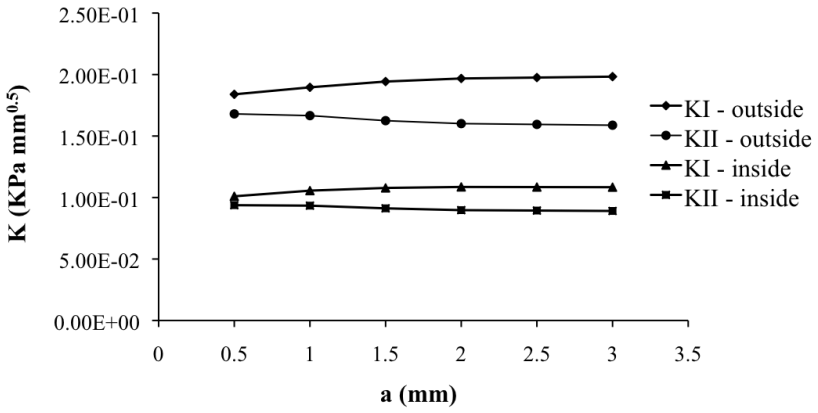

(a)

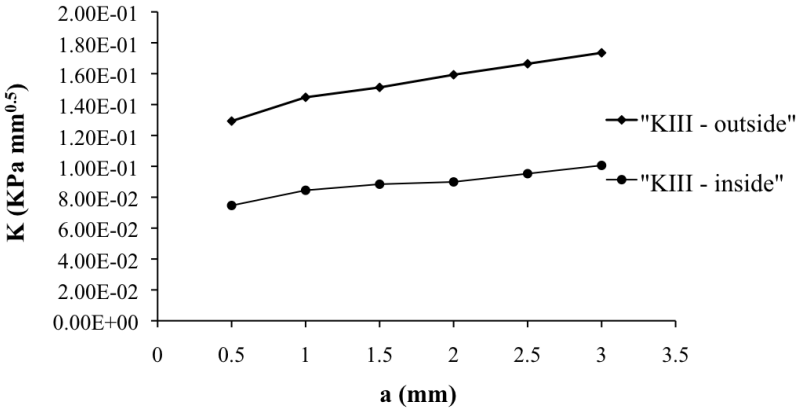

(b)

Figure 6.10: (a) Variation of mode-I and mode-II stress intensity factors as a function of the crack length, at the cross-sectional mid-point of the beam, and (b) variation of mode-III stress intensity factor as a function of the crack length, at the corners of the crack tip.

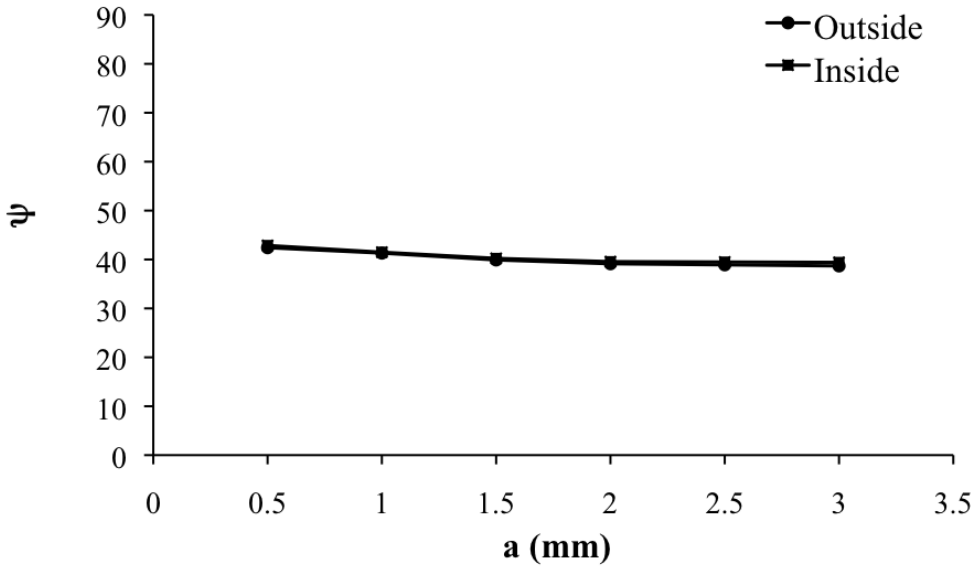

Figure 6.11: Mode mix as a function of the crack length, at the cross-sectional mid-point of the beam.

ideally plastic springs [179]. This model analytically estimates the toughening due to small-scale bridging (SSB). In this case the bridge length is relatively small compared to crack length, specimen dimensions, and distances from the crack to the specimen boundaries. The toughening due to SSB, $\triangle K_{SSB}$, is given by,

$$\triangle K_{SSB} = \sqrt{\frac{2}{\pi}} V_f \int_0^L \frac{\alpha \sigma_y}{\sqrt{x}} dx \tag{6.2}$$

where α is a constraint/triaxiality factor, V_f is the volume fraction of ductile phase, σ_y represents the uniaxial yield stress, x is the distance from the crack tip, and L is the bridging length, which is equal to the distance from the crack tip to the last unfractured reinforcement.

A large scale bridging model developed by Bloyer et al. [180, 181] was used to estimate the toughening due to large scale bridging (LSB) effects. This model that depends on the traction distribution, crack length, and specimen geometry, employs a weight function, $h(a, x)$ to calculate the stress intensity diminution caused by the shielding zone. For LSB the toughening due to ligament bridging $\triangle K_{LSB}$ is given by,

$$\triangle K_{LSB} = V_f \int_0^L \alpha \sigma_y h(a, x) dx \tag{6.3}$$

The weight function for the bridging tractions is given by Fett and Munz [182],

$$h(a, x) = \sqrt{\frac{2}{\pi a}} \frac{1}{\sqrt{1 - \frac{x}{a}}} (1 + \Sigma_{(\rho,\mu)} \frac{A_{\rho\mu}(\frac{a}{w})}{(1 - \frac{a}{w})} (1 - \frac{x}{a})^{\rho+1}) \tag{6.4}$$

where the coefficients A are given in the Table 6.2. Hence, the fracture toughness of the composite bamboo structure is the summation of crack-initiation toughness K_m and the added toughness, $\triangle K$, due to SSB or LSB. K_m is referring to mixed mode matrix toughness before fiber bridging happens and is found through experiments.

$$K_c = K_m + \triangle K \tag{6.5}$$

Once K_c is obtained the energy release rate can be calculated as,

$$G_c = \frac{K_c^2}{E_c'} \tag{6.6}$$

Table 6.2: Coefficients of $A_{\rho,\mu}$.

	μ				
ρ	0	1	2	3	4
0	0.4980	2.4463	0.0700	1.3187	-3.0670
1	0.5416	-5.0806	24.3447	-32.7208	18.1214
2	-0.1928	2.5586	-12.6415	19.7630	-10.9860

where G_c is the composite energy release rate, $E_c^{'} = E_c/(1-\nu^2)$ is the composite plane strain Young's modulus, ν is the Poisson's ratio, E_c is the composite Young's moduli.

In this study, α is taken to be 1.0 [179]. The volume fractions of fibers for outside and inside cracks are 0.45 and 0.2, respectively. The uniaxial yield stress for outside crack with denser fibers is around 620 MPa whereas for inside crack is around 220 MPa. The Young's moduli are about 16 GPa and 7.5 GPa for outside and inside cracks, respectively.

6.3 Results and Discussion

The experimental results and resistance-curve behavior of bamboo are presented in the following section.

6.3.1 Crack-Resistance Curve

The resistance of the bamboo to crack growth was found as a plot of applied load versus crack growth length for the two different crack orientations. It was observed that for each case the applied load increased with additional crack growth leading to a rising curve. This indicates that the resistance to crack extension increases with crack length.

The cracks in both inside- and outside-notched samples grow parallel to the longitudinal direction of fibers. In all the specimens tested, the crack does not grow straight. All cracks kink 90° with respect to fibers orientation and advance parallel to the fiber direction. The applied load associated with this pre-crack is known as P_0 , and it is a measure of the material's resistance to crack initiation. It can be observed that this value appears to depend on the placement of the notch, with higher value for inside-notched specimen than the outside-notched specimens. After pre-cracking further stable crack growth occurs at a higher load.

The resistance curve for the bamboo structure as a function of crack (kinked) length is presented in Fig. 6.12. It is noted that the R-curve of bamboo does not exhibit saturation behavior; however, the curve rises gradually up to point of instability. This instability point can be considered as a point of failure for any given notch position. In general, it can be said that this corresponds to a crack size of $\sim$12 mm. The differences in the fracture resistance of the bamboo in different notch orientations can be explained as a result of the graded structure of bamboo. Bamboo is a composite material consisting of vascular bundles of fibers in a matrix of parenchyma cells. Bamboo derives its strength from the vascular fibers that can sustain higher stresses during deformation. As shown in Fig. 6.1, the outer circumference of the bamboo culm has a higher density of fibers, with the density decreasing towards the inner circumference. This implies that the stresses due to the bending loads would be highest at the outer side of the wall and lowest at the inner side of the wall. In the presence of notches or cracks; however, the high energy involved due to the deformation and bending of regions with higher density of fibers causes a high stress concentrations at the notch/crack tips, which leads to high crack driving forces at crack tips for a unit load, Fig. 6.9. Meanwhile, the regions with the least fiber density do not result in high stress concentrations at crack tips, but rather tend to dissipate the energy by some inelastic deformation. It could be said that the much higher loads observed for an inside-notched sample can be explained by two following reasons: (a) the higher level of strain energy of the uncracked outer layer to applied bending loads, and (b) the energy-dissipating capability of lesser fiber-density notched region. The combination of these two conditions results in higher crack initiation/propagation loads for a sample with a inside crack. For the case of outside-notched sample, the opposite occurs. That is, the part in contact with the applied load (the bottom part of the bamboo) is weak and bends easily under lower applied loads. The resulting bending stress is tensile in the region that contains the notch. As a result of the high fiber density, which causes high stress concentrations at the crack tip, much lower stresses are magnified to levels equivalent to crack-driving force. Hence, lower loads for crack initiation/propagation are observed for the outside-notched samples.

The main effect of mixed mode on toughness of a bamboo is postulated to be on the matrix toughness, K_m. Afterwards, the large scale mode-I fiber bridging formulations can precisely predict the toughening behavior of bamboo. Hence, as the formulation clearly shows, the contribution of mode-

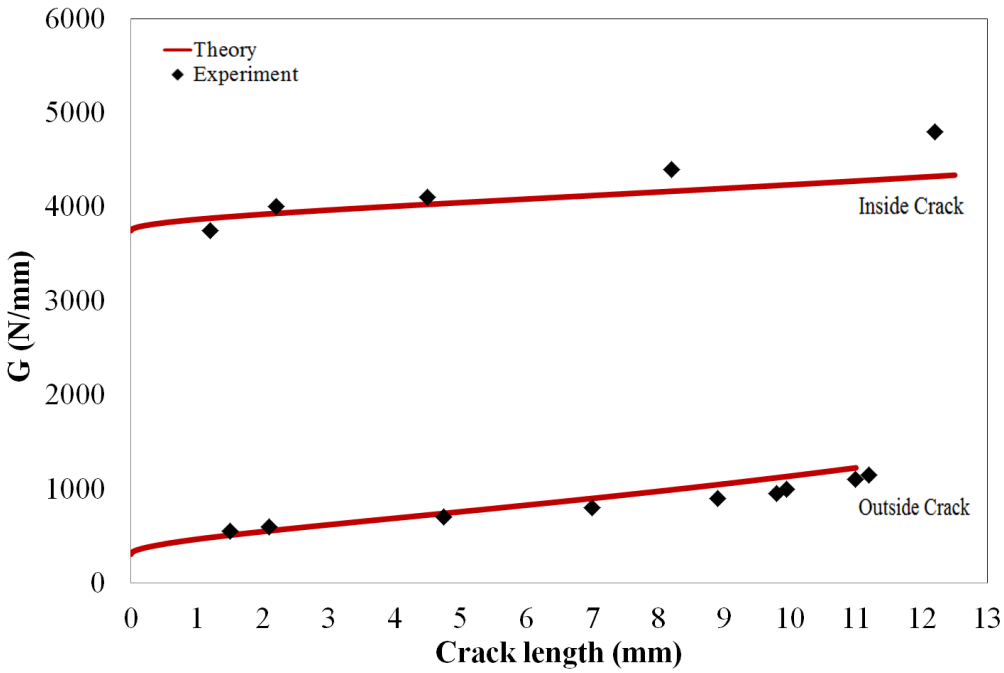

Figure 6.12: Resistance curve behavior of bamboo for two possible crack configurations

II toughening mechanism to intrinsic toughness of bamboo is negligible.

6.3.2 Crack/Microstructure Interactions

It is quite clear from Fig. 6.12 that the bamboo exhibit R-Curve behavior in both inside and outside cracked directions. However, this behavior is more pronounced for samples with an outside crack than samples with an inside crack. During the inside crack propagation, the energy release rate starts around 3700 N/mm and constantly increases to around 4100 N/mm. The energy release rate of an outside crack is around 350 N/mm at the beginning of the crack initiation. This value rises to 1100 N/mm after 11 mm of crack length. Fig. 6.13 and 6.14 show typical crack/microstructure interactions of bamboo as the load is increased to advance the crack, for the outside-notched and inside-notched specimens, respectively. These observations were made possible by means of a high-resolution camera that enables the position of cracks to be tracked and recorded. It can be observed that the crack starts from two corners of the notch due to the relatively high stress concentrations at these points. However, the loads at which crack growth starts depends on the side of the bamboo that contains the notch, being highest for the inside-notched specimen and least for the outside-notch specimen. The important observation from Fig. 6.13 and 6.14 is that the direction of crack growth or the crack growth path deviates from that of the original notch, which is perpendicular to fiber longitudinal direction.

Another observation from Fig. 6.13 and 6.14 is that the length and width of the crack increases with applied loads, with bridging across the faces of the cracks. Such bridges absorb energy, and thus, reduce the effective stress intensities at the crack tip. Hence, higher applied loads are required for crack growth, leading to rising observed crack-resistance curves (R-curves) of Fig. 6.12. A comparison of Fig. 6.13 and 6.14 reveals that the effects of crack bridging on toughness in the inside-notched specimen is larger and more pronounced, due to the lower fiber density. This shows that the inner side of the bamboo culm is tougher than the outer side, which in turn is stronger than the inner part.

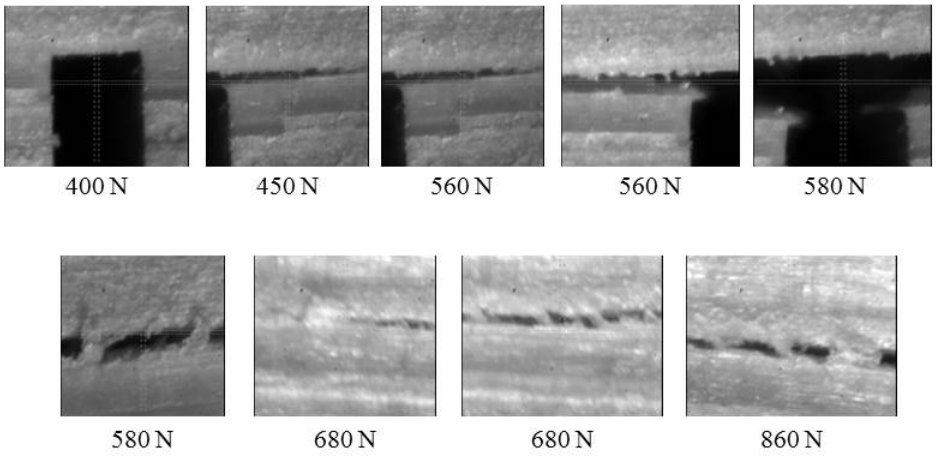

Figure 6.13: Crack/Microstructure Interactions for crack growth in samples with outside crack. Magnification 100X

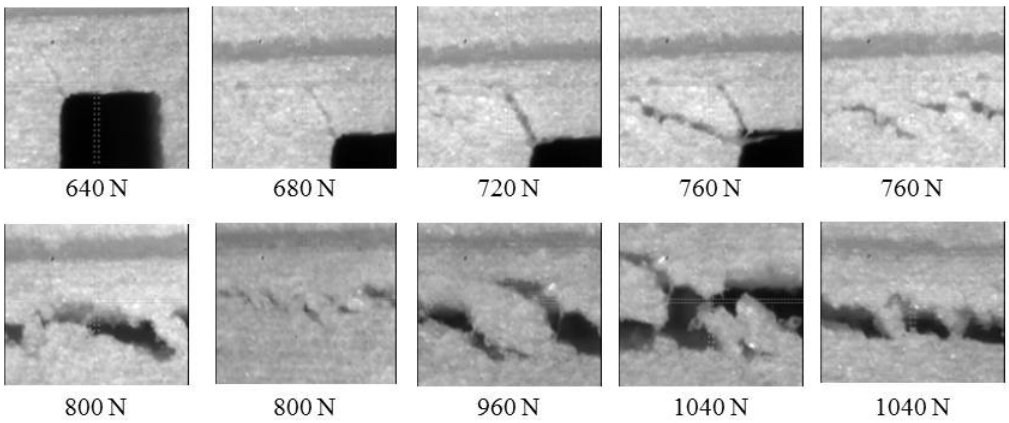

Figure 6.14: Crack/Microstructure Interactions for crack growth in samples with inside crack. Magnification 100X

6.4 Conclusion

The paper presents the results of an experimental study of the structure and toughening mechanisms in Moso culm bamboo. The hierarchical and multi-scale structure of bamboo is revealed via laser scanning and atomic force microscopy. These methods reveal a distribution of nano-scale fibers within fiber bundles in a parenchyma cell matrix. Experiments show that all cracks, independent of the notch direction, appear to follow a path parallel to the fiber's longitudinal direction. Finite element method along four-bend tests was used to study bamboo toughness for two possible crack configurations and R-curve behavior due to crack bridging for inside and outside cracks is clearly presented. In all cases, the toughening was observed to occur via crack bridging mechanism. The R-curve behavior is also shown to be dependent on the density of the fibers. This results in higher crack-tip shielding levels where the bridge laths are larger in the lower stress regions with lower fiber densities, when crack growth occurs along the fibers. Conversely, the toughening due to crack bridging is lower in the outer regions in which the bridges are smaller. The implications of the results are quite significant as they show that the microstructural requirements for improved strength and deformation resistance in bamboo structures are different from those required for improved toughening and resistance curve behavior. The overall toughening can be observed more significantly in the regions with lower density fibers while fibers strengthen the structure.

7

Effect of Humidity on Torsional Properties of Bamboo

7.1 Introduction

Bamboo is one of the oldest building materials used by mankind. There are signs in far east, for instance, where Chinese writings and drawings refer to bamboo that date back from 1600 to 100 BC. [27],[20]. Bamboo has been used to fabricate structural elements and also as an alternative to steel in reinforced concrete [28]. Sustainability and the practice of using environmentally friendly materials is continually gaining momentum in both developed and underdeveloped parts of the world [19]-[22]. This is largely due to the decreasing supply of available timber around the world. Natural materials all around us exhibit fascinating properties that are typically multifunctional and optimal for the construction purposes [24]. Bamboo is a very favorable sustainable material for the construction industry. Bamboo's attractive combination of strength-to-weight ratios, stiffness-to-weight ratios, and shape factors make it an ideal candidate for construction materials and many other applications [21]-[26].

Most bamboo culms are cylindrical and hollow, with diameters ranging from 0.25 inches to 12 inches. Bamboo is considered a composite made up of non-uniformly distributed longitudinal fibers [29, 30, 34]. Separating the culms are evenly spaced nodes with internal diaphragms (knots). The main constituents of bamboo culms are cellulose, hemicellulose and lignin, which amount to over 90% of the total mass [31]-[33]. The minor constituents of

bamboo include resins, tannins, waxes and inorganic salts. As an orthotropic material, the density of the bamboo changes through the cross-section, ranging from 500 $\frac{kg}{m^3}$ to 800 $\frac{kg}{m^3}$, with the higher density located at the outside face. The unique fiber-matrix ratio and distribution give bamboo exceptional strength characteristics [35]-[37]. To prevent non-uniformity in stress concentration and increase bonding strength between layers, the variation in the properties along the thickness of the culm should be modeled using a smooth transition [40]-[42]. There are many variables that affect the strength of bamboo, including maturity, season when it is harvested, and the treatment applied after the bamboo harvest. Previous studies have shown that the optimum maturity period is about 3-4 years to provide maximum strength [183]. Following this period of time the strength and density of bamboo begins to decay. At the optimum maturity period, bamboo has shown tensile strengths greater than spruce and equal to or greater than steel per unit weight.

Few studies treating the modeling of natural fibers have been found in the literature due to the complexity of the microstructure [167, 34]. However, there are many experimental studies on bamboo measuring strength, Young's modulus of matrix and fiber, and through the analysis of its microstructure and fiber distribution [36],[167]-[170]. In a study by Dixon et al. (2014), the flexural properties of Moso bamboo in the axial direction, along with the compressive strengths in the axial and transverse directions were measured, and based on the microstructural variations and extrapolated solid cell wall properties of bamboo, analytical models which describe the experimental results were developed [23]. Another approach used to estimate how the microstructure influences the effective properties of bamboo is to model these materials through the use of homogenization, or the extraction of the microstructure properties that can then be introduced to the section as a whole [174]-[176]. Employing a homogeneous, averaged value of Young's modulus can also be used, allowing comparisons and demonstrating the limitations of simplified procedures. However, considering that bamboo has complicated shapes and material distribution inside its domain with many important details, the numerical methods such as the Finite Element Method (FEM) can be useful tools for understanding the mechanical behavior of these Functionally Graded Materials (FGMs) [24], [38], [177], [172], [39] and many composite structures in general [171] [184]. Molecular Dynamics is another effective tool to study the properties of composite materials [33, 185, 186].

In spite of its structural application, there have been no prior mechanistic

studies on the role of water content with regard to the mechanical performance of bamboo. Many studies have been conducted on other biological materials such as nacre and bone. As an example, the existence and role of water in the structure of nacre has been investigated by many researchers. It has been mentioned that the effect of water acts to increase the ductility of nacre and increase the toughness [62, 69]. The conductivity of bamboo and the effect of absorbed water were investigated in a study conducted by Shiji et al. [187]. However, more multiscale investigation is needed to understand the effect of water content or humidity on the mechanical performance.

The goal of this study is to experimentally and numerically investigate the mechanical behavior of bamboo in torsion. While other studies have estimated the modulus and stiffness, very few studies have investigated the torsional properties and shear modulus of bamboo. In this chapter, a new method of modeling was used to estimate the shear modulus of bamboo. Additionally, the effect of humidity on the torsional behavior of bamboo was investigated. The results of this study can be used as a guide to improve the properties of bamboo in different applications, take advantage of the effect of water on natural materials, and to design and make bio-inspired composites with remarkable mechanical properties.

7.2 Materials and Method

7.2.1 Experimental Procedure

Samples from the Phyllostachys species of bamboo were used for the torsional experiments conducted in this study. The bamboo samples were approximately five years old. The bamboo was kiln dried and stored in a ventilated warehouse for at least a year followed by storage within the lab. The storage assured that only gradual moisture changes took place and ensured that cracks in the bamboo did not form prior to testing. The experiment in torsion was conducted using a Tinius Olsen Model 290 torsion testing machine (Fig. 7.1) with a maximum torque of 10,000 lb-in. The onboard load display was bypassed with the use of LabView software platform with a custom written program to record load, rotation, and strains. Two fixtures were fabricated out of mild steel with six $\frac{3}{8}$ in. -24 thread bolts in each for securing the bamboo sample.

Kiln dried Phyllostachys bamboo was cut to 14 inches in length. The

specific length of 14 inches was chosen due to the limitation of the testing machine having a maximum specimen length of 20 inches in addition to the bamboo node spacing. With the specimen having a node spacing of approximately 12 inches, the fittings could be clamped within one inch of a node on each end of the 14 inches specimen. The average diameter of the bamboo was about $2\frac{1}{4}$-inch with a $\frac{1}{4}$-inch wall thickness.

An important factor in a torsion experiment is to prevent slippage between the specimen and the fixture for accurate rotation recordings measurements. Preliminary tests of the fixture system resulted in the bolts slipping on the bamboo surface at a torque of approximately 800 lb-in. Further tightening of the bolts would pose additional damage to the specimen and larger concentrated loads at the location of the bolts. As a result, a new system was developed by precisely drilling $\frac{9}{32}$ in. holes where the fitting bolts would normally meet with the bamboo. A series of one inch wide washers bent to the outside curvature of the bamboo along with $\frac{3}{4}$ in. washers bent to the inside curvature are used in conjunction with $\frac{1}{4}$-inch bolts and matching nuts, one inch in length to create the mounting setup. In addition, 80 grit drywall sandpaper was sandwiched between the outside washer and bamboo to provide increased friction. A completed bamboo specimen setup is shown in Fig. 7.1.

By orientating the bolt heads parallel to the longitudinal fiber direction, the heads can bear the applied transverse load. The specimen was mounted into the fitting with the fitting bolts tightened onto the washers and bearing on the bolt head. Using the $\frac{9}{32}$-inch hole through the bamboo and large washers distributed the load evenly and prevented excessive concentrated loads at the hole locations. Using the setup, the experiment proved to be successful with no slippage and failure occurring in between the mounting holes, showing that excessive concentrated loads are not taking place at the holes. Loading occurred at five degrees per minute until the specimen reached failure. Throughout the experiment load (torque) and rotation were recorded at a rate of 5 data points per second.

Microstructure of Bamboo

Fig. 7.2 shows the structures of bamboo as scanned using a laser scanner. This image shows bamboo structure consisting of bundles of vascular fibers in a matrix of parenchyma cells. Most significantly, the mesostructure is highly graded in that the volume fraction of the fibers in the bamboo culm

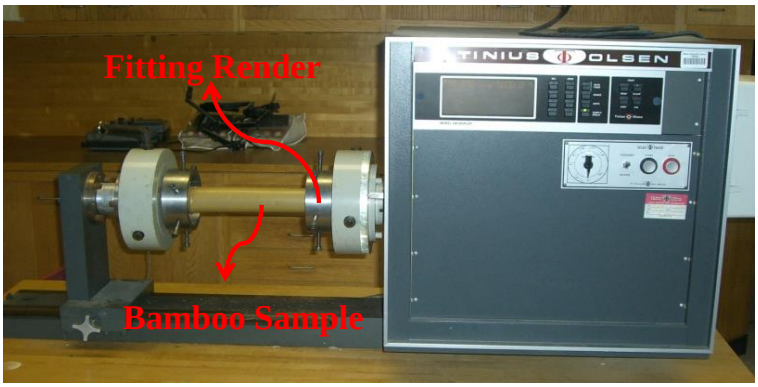

(a)

(b)

Figure 7.1: (a) Experimental setup, (b) The fixtures (grit drywall sandpaper, bolts and matching nuts) that were used to secure the bamboo sample during the torsion test.

increases from inside to outside, the latter being the part that is exposed to the atmosphere or environment. The high fiber density region, low fiber density region and the medium fiber density region (in-between these two regions) can be seen in the image. The microstructural features of the fiber bundles were also studied here by means of an Atomic Force Microscope (AFM). Samples were polished with a 4000 grit sand paper to a 1 μm surface finish. Later, the surface roughness of the samples was studied with an AFM in the tapping mode. Two and three-dimensional images are captured and shown in Fig. 7.2.

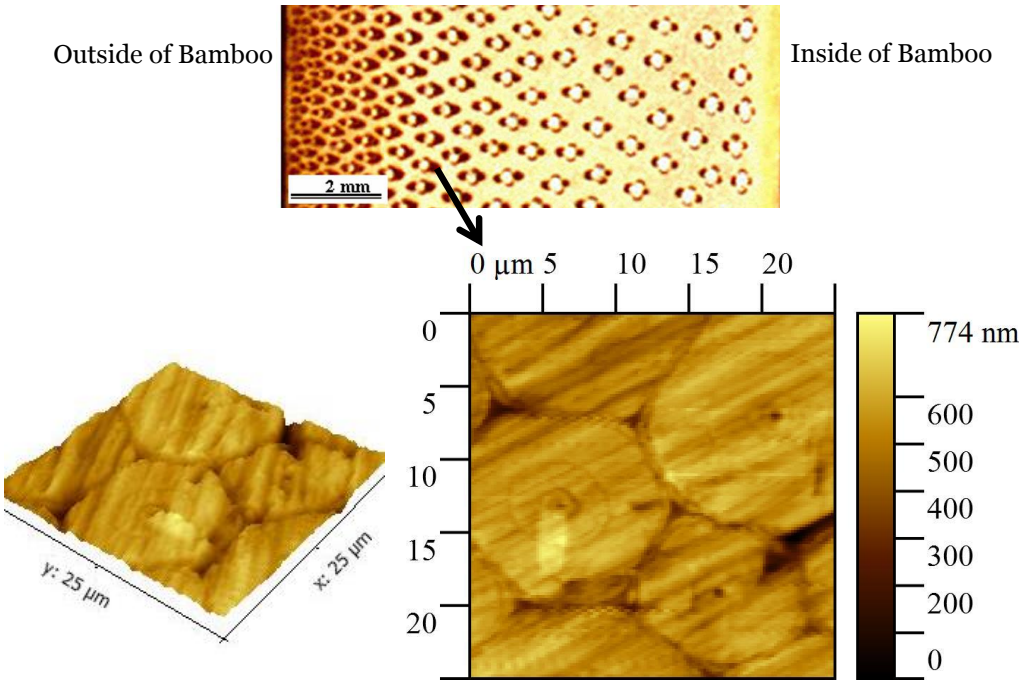

Figure 7.2: Bamboo cross section image taken using laser scanner and the 2D and 3D AFM images of the bamboo fibers.

Effect of Humidity

To understand the effect of water content on the shear behavior of bamboo, samples were prepared and kept in five environments with different

humidities. The humidities were set to 25%, 40%, 60%, 80% and 100%. The humidity was controlled in a moisture and temperature chamber where the humidity was set to a constant value. A high precision programmable constant temperature and humidity chamber (VisionScientific Co. LTD, South Korea) was used. Samples remained in the chamber for 48 hours, removed and immediately tested. The samples were cut from the same parts of the bamboo stalks. Five samples for each humidity were tested and the torque-rotation curves were obtained.

7.2.2 Finite Element Analysis

Three-dimensional finite element simulations were performed to extract the shear properties of the samples assuming orthotropic mechanical behavior. Four-node tetrahedron elements were used to mesh the model (Fig. 7.3). A total of 151381 elements and 679949 nodes were used to define the finite element model.

The material properties of the fiber and matrix used to find the components of the orthotropic stiffness tensor are presented in Table 6.1. Fiber volume fractions as a function of thickness were calculated from the laser scanning measurements. The laser scanning images were used to count the number of fibers per unit length as a function of the distance from the outer layer of bamboo. Later, the general rule of mixtures for composites was applied to estimate the actual graded elastic properties of bamboo microstructure as a function of thickness [188]. Orthotropy is the property of a point within an object rather than for the property of the object as a whole. Bamboo is both orthotropic and inhomogeneous which means it possesses orthotropic properties that vary from inside to outside layers.

The simulations were performed in two steps. In the first step, the distribution of fiber was implemented into the model. The gradient of stiffness from the inside layer to outside layer was assumed to be linear [189]. Therefore, two different sets of orthotropic properties, one for the inside layer and the other one for the outside layer were sufficient to define the properties of the bulk model. The properties presented in Table 6.1, the orientation of the fibers in the parenchyma cell, and the orthotropic properties of the parenchyma cell itself were used to define the stiffness tensor of the bamboo model in torsion. The second step was to apply the torsion load on the sample and compute the rotations from the results as the other end is fixed in all directions and rotations.

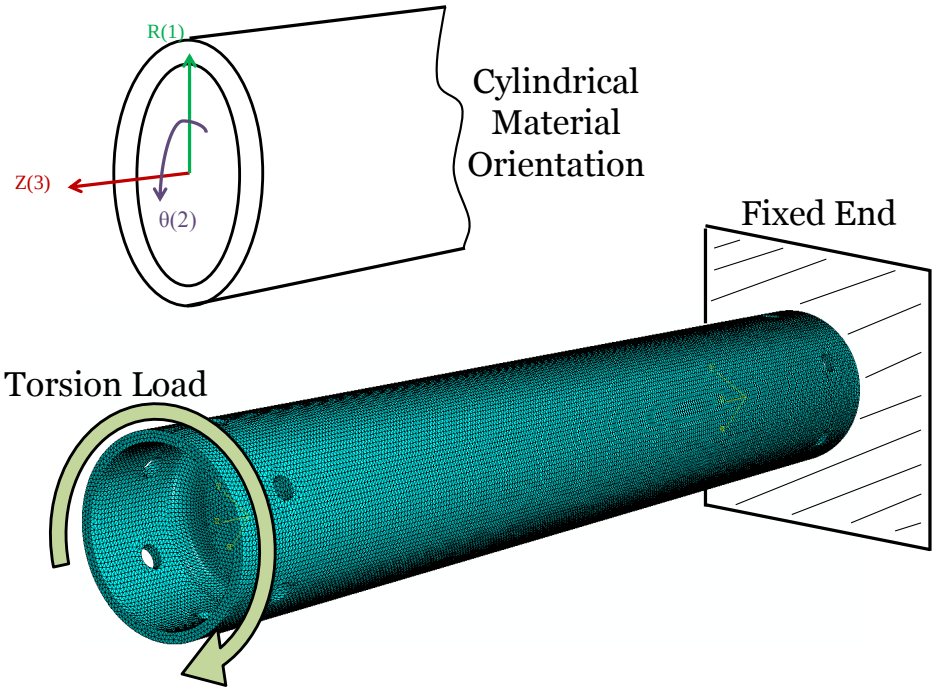

Figure 7.3: The three dimensional meshed model and the assigned material orientation used to implement the orthortropical mechanical behavior.

7.3 Results and Discussion

7.3.1 Torsion Tests

The raw data (torque-rotation) of the torsion experiments on different samples were obtained. Since, the measurement of total strain field of a heterogeneous orthotropic material is difficult, and the finite element results showed that the behavior of dry samples (environmental humidities less than 25%) can be reasonably approximated as a linear orthotropic material, this behavior was assumed to compute the stress strain curves for all samples. The slope of these curves in the early stage of deformation is the average shear modulus. The typical shear stress-shear strain curve for the torsion experiment on samples kept in an environment with 25% humidity is presented in Fig. 7.4. All the 25% humidity samples show a similar linear behavior under torsion. The shear strength of these samples is approximately 1700 $\frac{lb}{in^2}$.

Fig. 7.5 shows a fractured sample under torsion. It was observed that the crack did not start from the fixture bolts on the sample. Hence, it proves that the test setup was successful in applying pure torque on the sample and in preventing stress concentration around the bolts.

7.3.2 Finite Element Analysis

The shear modulus of bamboo was computed using finite element analysis and the prescribed experimental data. The general rule of mixtures was assumed to be able to implement the mechanical properties of bamboo into the model. The compliance matrix, S, used for the inside and outside layers are the following:

$$S = \begin{pmatrix} \frac{1}{E_1} & -\frac{\nu_{21}}{E_2} & -\frac{\nu_{31}}{E_3} & 0 & 0 & 0 \\ -\frac{\nu_{12}}{E_1} & \frac{1}{E_1} & -\frac{\nu_{32}}{E_3} & 0 & 0 & 0 \\ -\frac{\nu_{13}}{E_1} & -\frac{\nu_{23}}{E_2} & \frac{1}{E_1} & 0 & 0 & 0 \\ 0 & 0 & 0 & \frac{1}{G_{23}} & 0 & 0 \\ 0 & 0 & 0 & 0 & \frac{1}{G_{31}} & 0 \\ 0 & 0 & 0 & 0 & 0 & \frac{1}{G_{21}} \end{pmatrix}$$

The nine components of the compliant tensor needed to define the compliance matrix for the inside and outside layers is computed by considering

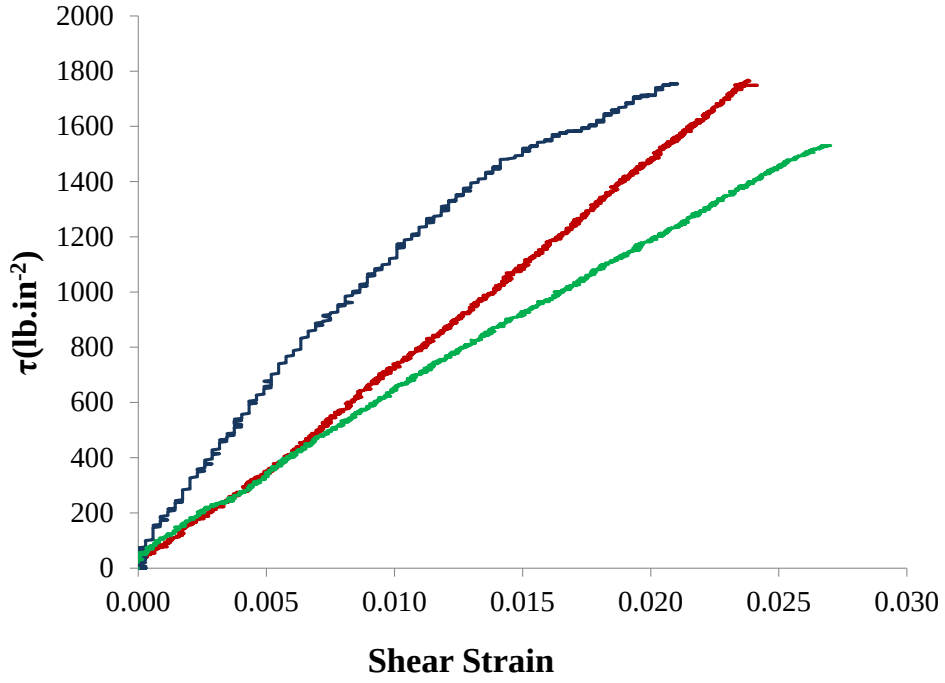

Figure 7.4: The shear stress-shear strain curve of the bamboo specimens computed from the torsion experiment with 25% environmental humidity.

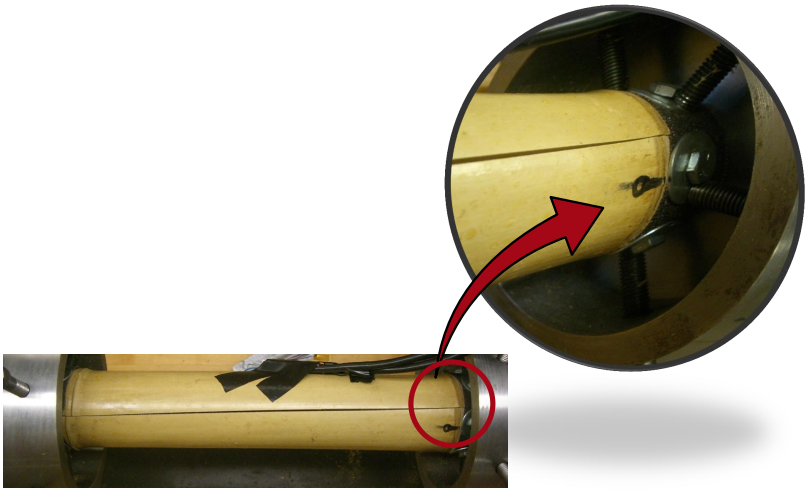

Figure 7.5: The samples under torsion tests were not fractured from the holes. This proves that the test setup is successful in eliminating the effect of stress concentration around the holes.

the volume fraction of fibers in the inner and outer layers of bamboo. The properties of the outer layer and inner layer are as following:

Table 7.1: Components of complaint tensor considered in the finite element model for inside and outside layers.

	E_1 (ksi)	E_2 (ksi)	E_3 (ksi)	ν_{12}	ν_{23}	ν_{13}	G_{12} (ksi)	G_{23} (ksi)	G_{13} (ksi)
Inside	40	40	70	0.35	0.35	0.35	29	20	20
Outside	360	360	2900	0.3	0.35	0.35	1100	145	145

These numbers can be extracted from the numbers presented in the Table 6.1 and the rule of mixtures for composites in different directions assuming 80 % fibers for outer layer and 20 % fiber for the inner layer and the rest are parenchyma-cells. E_1 is the modulus in R direction which assumed to be the same as E_2 which is the modulus in θ direction and E_3 is the modulus along the fibers (Z direction). The properties of an average wood (mainly made of paranchyma-cells) can be used to find the shear moduli in inner and outer layers. The compliant tensor is then defined and implemented into the finite element model. Fig. 7.6a shows how the distribution of stiffness in the system, which increases from inside to outside layers. The stiffness gradient is assumed to be linear in the model [24]. Fig. 7.6b shows the maximum principle stress distribution of the bamboo sample under torsion. Finding the compliant tensor for samples in higher environmental humidities requires knowledge of the mechanical properties of bamboo fibers and parenchyma cell with different water contents. Hence, the proposed numbers apply for the bamboo samples prepared in low environmental humidity (under 25%).

These simulations are used to estimate an average shear modulus of the bamboo. In order to find the shear modulus, a specific amount of rotational deformation was applied to one end of the model while the other side was fixed. The reaction torque that appears in the fixed end can be used to find the average shear modulus. The following equation which only applies for isotropic materials was used to find the average shear modulus (G). The geometry of the model should be used to find the torsional rigidity (J).

$$\theta = \frac{TL}{JG} \tag{7.1}$$

where θ is the angle of twist, T is the torque or moment, L is the length of

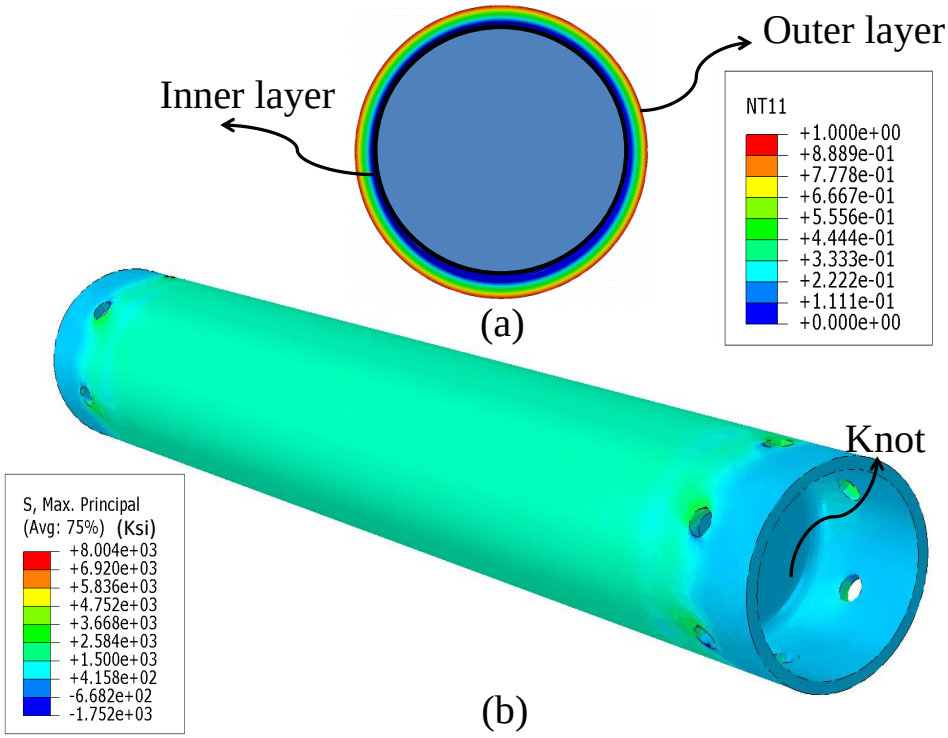

Figure 7.6: (a) The gradient of stiffness in the cross section of the bamboo model, (b) The maximum principle stress distribution in the sample after the application of torsion.

the model and J is the torsion constant for the section, and G is the average shear modulus.

Table 7.2: Comparison between shear modulus found by finite element method (FEM) and experiments.

Method	Experimental (25% humidity)	Numerical (FEM)
Shear Modulus (ksi)	108	133

The numerical simulation results agree well with experimental data as shown in Table 7.2. This shows that the proposed modeling approach is correct for a dry (25% environmental humidity) bamboo samples using the available data on the mechanical properties of bamboo fiber and matrix. The slight difference between the experiments and numerical results is perhaps due to vast variety in the mechanical properties of the fibers and matrix of different bamboo samples. While, all bamboo sample have the same age and were prepared under the same protocol, there is still a variety of properties from samples to sample. Modeling the samples with higher humidity requires more information about the properties of bamboo fibers and parenchyma cell with different water contents.

7.3.3 Effect of Humidity

The goal of this study is to understand the effect of environmental humidity on the shear modulus and shear strength of bamboo samples. The raw data (torque-rotation) of the torsion experiments of samples with different environmental humidities are presented in Fig. 7.7. Assuming homogeneous isotropic behavior, the shear stress-shear strain curves from experimental data for the samples are calculated and presented in Fig. 7.8. The slope of these curves at the early stage of deformation is the average shear modulus and can be compared for samples prepared in different environmental humidities.

The results indicate that as the humidity (water content) increases, the failure shear strain of the bamboo samples increases. Moreover, the shear stress-shear strain curves show a softening region due to the increased humidity. The samples with humidity level of 25% and 40% behave linearly, while samples with 60%-100% humidity behave nonlinearly, since humidity increases the softening behavior of bamboo. The samples with 25% humidity

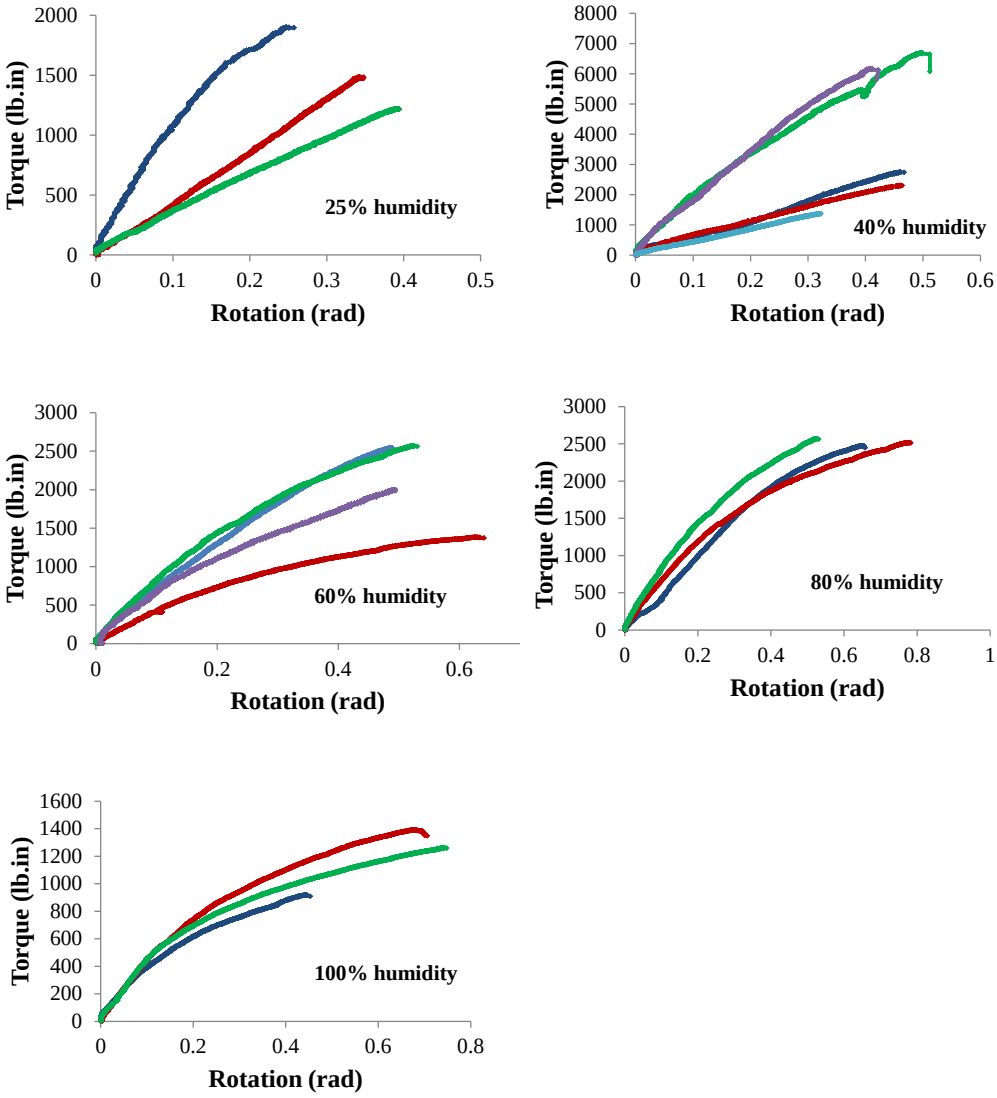

Figure 7.7: The torque-rotation curves obtained from torsion experiment on bamboo specimens prepared in 25% to 100% environmental humidity.

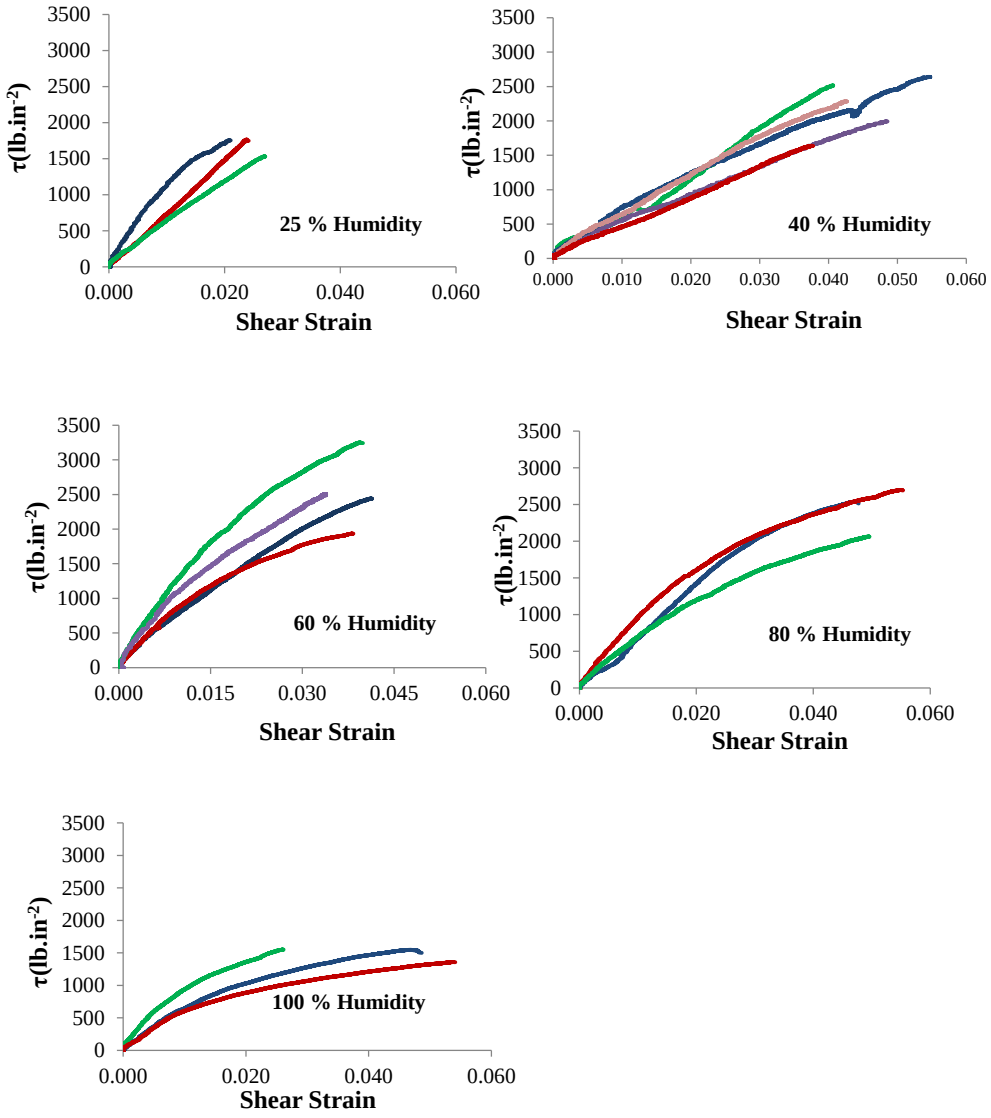

Figure 7.8: The shear stress-shear strain curves of the bamboo specimens computed from the torsion experiment with 25% to 100% environmental humidities.

show a failure strain of around 0.028, while, the samples with 40% and 60% humidity show a failure strain of around 0.045, and samples with 80% and 100% humidity show a failure strain of around 0.056. The effects of humidity on the ultimate strength of the samples are presented in Fig. 7.9. The results clearly show that there is an *optimum environmental humidity* between 60% and 80% that causes the highest shear strength in bamboo. Moreover, increase in humidity beyond 80%, causes a significant drop of the ultimate strength.

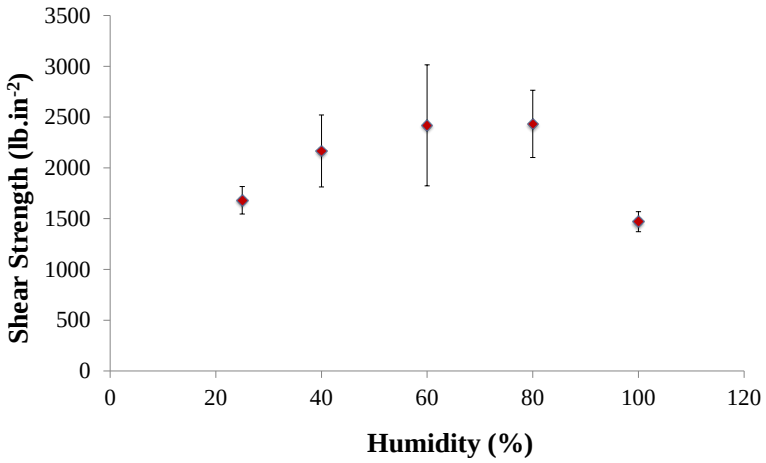

Figure 7.9: Effect of humidity on the ultimate strength of the samples. The error bars show the standard deviation of the experimental results.

Fig. 7.10 presents the effect of humidity on the shear modulus of the samples. The results show that there is a small jump in the shear modulus of bamboo at environmental humidity of about 60%, otherwise, all other samples show almost similar shear stiffness of about 100,000 psi.

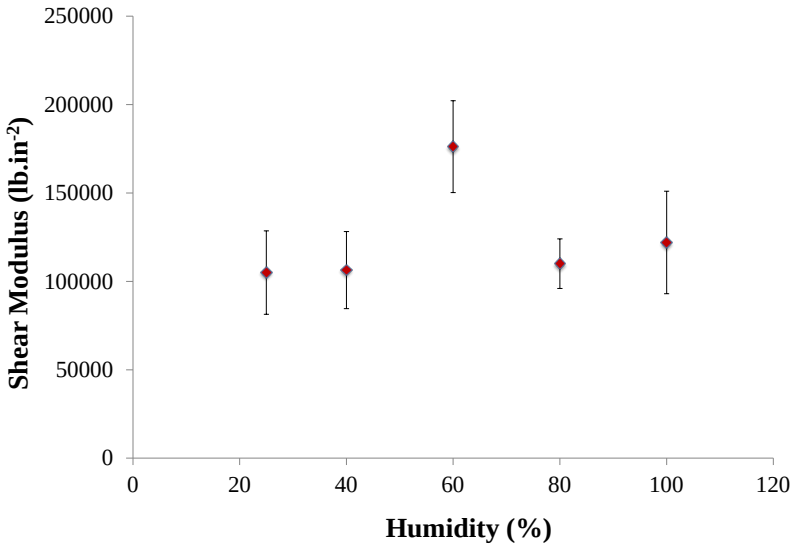

Figure 7.10: Effect of humidity on the shear modulus of the samples. The error bars show the standard deviation of the experimental results.

7.4 Conclusion

This study presents the results of experimental and numerical studies on the torsional behavior of bamboo, a natural functionally graded composite material with remarkable mechanical properties. Since water content plays an important role on mechanical properties of natural materials, the experimental part of this study focused on the effect of humidity on the performance of bamboo samples under torsion. Finite element analysis was used to model bamboo under torsion as a heterogenous orthotropic material with linear distribution of fiber across the section. The shear modulus found from the numerical analysis is consistent well with the experimental data which shows that the finite element analysis can be used as a tool to estimate an average shear modulus of the samples. The overall results also show that bamboo kept in an environment with humidity level of 60% demonstrated the highest shear modulus. The optimal humidity of the samples for highest strength is between 60% - 80%. The results show that bamboo exhibits more ductility under torsion as the humidity of the samples increases. The results of this

study provides crucial information on the role of water on the optimal shear strength of bamboo. This information is essential in understanding the role of water on mechanical properties of bamboo fiber and matrix.

8

Summery and Conclusions

Studying the strength and stiffness of natural composites has a profound impact on the development of man-made materials. Designs in nature are incredible for their combination of building blocks and amplification of properties [3],[5]. One of these composites is nacre, which possesses impressive mechanical properties in terms of its strength and stiffness. Nacre is made up of 95% aragonite ($CaCO_3$) and 5% organic materials [102]. These components are weak individually, with protein as soft as skin and minerals as brittle as chalk; however they come together to form a remarkably strong composite [17]. The high mineral content in nacre makes it one of the stiffest natural composites [3]. The arrangement of nacre structure allows it to be twice as strong and a thousand times tougher than its constituent materials [168, 190]. For example, while ceramics are superior to metals because they are stiffer, harder, and can be used at higher temperature their brittleness is a major drawback. However replicating the mechanisms in nacre could lead to ceramic-based composites significantly tougher than typical ceramics, broadening their potential uses [5]. There is much effort focused on mimicking the structure of nacre using various methods [191]-[193]. Even so, the deformation and toughening mechanisms of these materials need more in-depth investigations in order to design and fabricate nature-inspired composites.

In the present thesis, we extensively investigated the mechanical and fracture properties of nacre and nacre-inspired ceramic-polymer composites. Our experimental, numerical and analytical results shed light on the nacre's strategies to improve its mechanical properties. Nano-features, functionally graded interfaces and tablet's waviness are the most important known elements play roles in toughening and strengthening mechanisms of nacre. All

these elements are explored in the present dissertation. Moreover, the functionally graded structure of bamboo and its hierarchical structures is also studied. The effect of micro and nanoscale elements which cause small-scale bridging and the functionally graded structure which cause different crack resistance mechanisms in the structure, as well as the effect of humidity which pronounce the effect of water molecules on mechanical response of bamboo, were investigated.

From the findings of this research we can conclude that, in both nacre and bamboo the mechanical properties are highly dependent on the water content. In nacre, water molecules affect the mechanical response of the protein and the interaction between the ceramic and protein due to the charges. Water molecules change the mechanical properties of bamboo constituents at different levels. Moreover, the effect of functionally graded micro and nanostructures is important in their mechanical and fracture properties. Sharp changes in mechanical properties of constituents of a composite significantly affect its performance. Nature through the process of evolution teaches us that we have to avoid sharp interfaces in composites. In bamboo, we can observe functionally graded structure at different levels. The microstructure of bamboo changes through its thickness while; the size of bamboo fibers also changes. Similarly, we have shown that in multilayered composites, sharp changes in the interface of ceramic and polymer is a source of weakness.

Furthermore, the hierarchical structure of natural composites has an outstanding role in their toughness. We have shown that in each scale multiple toughening mechanisms are active and this is partially due to the hierarchical structure. Crack deflection and fiber pull-out are important toughening mechanism in these composites which are extensively investigated in this dissertation. Increasing fiber pull-out force to some extent can increase the toughness, however there is a compromise. Large Increase in the fiber pull-out force can cause fiber failure, and therefore, decrease the toughness. Our analytical solutions can help us find the optimum scenario considering all the present factors. Despite the multilayered or cylindrical geometry, the interfaces need to be strong enough to cause structure integrity, and at the same time weak enough to allow fiber pull-out and layer sliding. In nacre, tablet's waviness and proximity layer control this interface strength. In bamboo, fiber and matrix materials has a similar origin but different microstructure. The similar material origin creates a strong interface, while the foamy structure of parenchyma-cell decrease its strength.

Bibliography

[1] Ortiz, C., & Boyce, M. C. (2008). Bioinspired structural materials. Science, 319(5866), 1053-1054.

[2] Weaver, J. C., Milliron, G. W., Miserez, A., Evans-Lutterodt, K., Herrera, S., Gallana, I., ... & Kisailus, D. (2012). The stomatopod dactyl club: a formidable damage-tolerant biological hammer. Science, 336(6086), 1275-1280.

[3] Barthelat, F. (2010). Nacre from mollusk shells: a model for high-performance structural materials. Bioinspiration & biomimetics, 5(3), 035001.

[4] Woesz, A., Weaver, J. C., Kazanci, M., Dauphin, Y., Aizenberg, J., Morse, D. E., & Fratzl, P. (2006). Micromechanical properties of biological silica in skeletons of deep-sea sponges. Journal of Materials Research, 21(08), 2068-2078.

[5] Espinosa, H. D., Juster, A. L., Latourte, F. J., Loh, O. Y., Gregoire, D., & Zavattieri, P. D. (2011). Tablet-level origin of toughening in abalone shells and translation to synthetic composite materials. Nature communications, 2, 173.

[6] Mayer, G., & Sarikaya, M. (2002). Rigid biological composite materials: structural examples for biomimetic design. Experimental Mechanics, 42(4), 395-403.

[7] Currey, J. D., Landete-Castillejos, T., Estevez, J., Ceacero, F., Olguin, A., Garcia, A., & Gallego, L. (2009). The mechanical properties of red deer antler bone when used in fighting. Journal of Experimental Biology, 212(24), 3985-3993.

[8] Li, X., Chang, W. C., Chao, Y. J., Wang, R., & Chang, M. (2004). Nanoscale structural and mechanical characterization of a natural nanocomposite material: the shell of red abalone. Nano letters, 4(4), 613-617.

[9] Grunenfelder, L. K., Suksangpanya, N., Salinas, C., Milliron, G., Yaraghi, N., Herrera, S., ... Kisailus, D. (2014). Bio-inspired impact-resistant composites. Acta biomaterialia, 10(9), 3997-4008.

[10] Prabhakaran, M. P., Venugopal, J., Ramakrishna, S. (2009). Electrospun nanostructured scaffolds for bone tissue engineering. Acta Biomaterialia, 5(8), 2884-2893.

[11] Johnson, M., Walter, S. L., Flinn, B. D., Mayer, G. (2010). Influence of moisture on the mechanical behavior of a natural composite. Acta biomaterialia, 6(6), 2181-2188.

[12] Askarinejad, S., Kotowski, P., Shalchy, F., & Rahbar, N. (2015). Effects of humidity on shear behavior of bamboo. Theoretical and Applied Mechanics Letters, 5(6), 236-243.

[13] Askarinejad, S., Kotowski, P., Youssefian, S., & Rahbar, N. (2016). Fracture and mixed-mode resistance curve behavior of bamboo. Mechanics Research Communications.

[14] Launey, M. E., Chen, P. Y., McKittrick, J., Ritchie, R. O. (2010). Mechanistic aspects of the fracture toughness of elk antler bone. Acta biomaterialia, 6(4), 1505-1514.

[15] Song, Z. Q., Ni, Y., Peng, L. M., Liang, H. Y., & He, L. H. (2016). Interface failure modes explain non-monotonic size-dependent mechanical properties in bioinspired nanolaminates. Scientific Reports, 6.

[16] Xu, Z. H., & Li, X. (2011). Deformation strengthening of biopolymer in nacre. Advanced Functional Materials, 21(20), 3883-3888.

[17] Ji, B., & Gao, H. (2004). Mechanical properties of nanostructure of biological materials. Journal of the Mechanics and Physics of Solids, 52(9), 1963-1990.

[18] Wang, R. Z., Suo, Z., Evans, A. G., Yao, N., & Aksay, I. A. (2001). Deformation mechanisms in nacre. Journal of Materials Research, 16(9), 2485-2493.

[19] Sathitsuksanoh, N., Zhu, Z., Ho, T. J., Bai, M. D., & Zhang, Y. H. P. (2010). Special issue on lignocellulosic bioethanol: current status and perspectives. Bioresources Technology, 101(492), 64929.

[20] Lo, T.Y., Cui, H.Z., Tang, P.W.C., Leu, H.C. (2008) The effect of fiber density on strength capacity of bamboo. Construction Building Materials;22(7):1532-5.

[21] Ghavami, K. (2005). Bamboo as reinforcement in structural concrete elements. Cement and concrete composites, 27(6), 637-649.

[22] Xiao, Y., Zhou, Q., & Shan, B. (2009). Design and construction of modern bamboo bridges. Journal of Bridge Engineering, 15(5), 533-541.

[23] Dixon, P. G., & Gibson, L. J. (2014). The structure and mechanics of Moso bamboo material. Journal of the Royal Society Interface, 11(99), 20140321.

[24] Tan, T., Rahbar, N., Allameh, S. M., Kwofie, S., Dissmore, D., Ghavami, K., & Soboyejo, W. O. (2011). Mechanical properties of functionally graded hierarchical bamboo structures. Acta biomaterialia, 7(10), 3796-3803.

[25] Huang, X., Netravali, A. (2009). Biodegradable green composites made using bamboo micro/nano-fibrils and chemically modified soy protein resin.Composites Science and Technology, 69(7), 1009-1015.

[26] Janssen, J. J. A. (1981). Bamboo in building structures (Doctoral dissertation, Technische Hogeschool Eindhoven

[27] Yu, D., Tan, H., Ruan, Y. (2011). A future bamboo-structure residential building prototype in China: Life cycle assessment of energy use and carbon emission. Energy and Buildings, 43(10), 2638-2646.

[28] Geymayer, H. G., Cox, F. B. (1970, October). Bamboo reinforced concrete. In ACI Journal Proceedings (Vol. 67, No. 10). ACI.

[29] Habibi, M. K., & Lu, Y. (2014). Crack propagation in bamboo's hierarchical cellular structure. Scientific reports, 4, 5598.

[30] Low, I. M., Che, Z. Y., & Latella, B. A. (2006). Mapping the structure, composition and mechanical properties of bamboo. Journal of materials research, 21(8), 1969-1976.

[31] Zou, L., Jin, H., Lu, W. Y., & Li, X. (2009). Nanoscale structural and mechanical characterization of the cell wall of bamboo fibers. Materials Science and Engineering: C, 29(4), 1375-1379.

[32] Fernandes, A. N., Thomas, L. H., Altaner, C. M., Callow, P., Forsyth, V. T., Apperley, D. C., ... & Jarvis, M. C. (2011). Nanostructure of cellulose microfibrils in spruce wood. Proceedings of the National Academy of Sciences, 108(47), E1195-E1203.

[33] Youssefian, S., Rahbar, N. (2015). Molecular Origin of Strength and Stiffness in Bamboo Fibrils. Scientific reports, 5.

[34] Silva, E. C. N., Walters, M. C., Paulino, G. H. (2006). Modeling bamboo as a functionally graded material: lessons for the analysis of affordable materials. Journal of Materials Science, 41(21), 6991-7004.

[35] Ghavami, K. (1995). Ultimate load behaviour of bamboo-reinforced lightweight concrete beams. Cement and concrete composites, 17(4), 281-288.

[36] Lakkad, S. C., & Patel, J. M. (1981). Mechanical properties of bamboo, a natural composite. Fibre science and technology, 14(4), 319-322.

[37] Lo, T. Y., Cui, H. Z., & Leung, H. C. (2004). The effect of fiber density on strength capacity of bamboo. Materials Letters, 58(21), 2595-2598.

[38] Nogata, F., & Takahashi, H. (1995). Intelligent functionally graded material: bamboo. Composites Engineering, 5(7), 743-751.

[39] Ghavami, K., Rodrigues, C. D. S., & Paciornik, S. (2003). Bamboo: functionally graded composite material.

[40] Suresh, S., Mortensen, A. (1988) Fundamentals of functionally graded materials. IOM Communications, London

[41] Paulino, G.H., Jin, Z.H., Dodds RH Jr (2003) In: Karihaloo B, Knauss WG (eds) Comprehensive structural integrity, vol 2. Elsevier, p 607

[42] Janssen, J.J.A. (1991) Mechanical properties of bamboo. Kluwer Academic Publishers

[43] Amada, S., & Untao, S. (2001). Fracture properties of bamboo. Composites Part B: Engineering, 32(5), 451-459.

[44] Shao, Z. P., Fang, C. H., & Tian, G. L. (2009). Mode I interlaminar fracture property of moso bamboo (Phyllostachys pubescens). Wood science and technology, 43(5-6), 527-536.

[45] Jackson, A. P., Vincent, J. F. V., & Turner, R. M. (1988, September). The mechanical design of nacre. In Proc. R. Soc. Lond. B (Vol. 234, No. 1277, pp. 415-440). The Royal Society.

[46] Meyers, M. A., Chen, P. Y., Lin, A. Y. M., & Seki, Y. (2008). Biological materials: structure and mechanical properties. Progress in Materials Science, 53(1), 1-206.

[47] Espinosa, H. D., Rim, J. E., Barthelat, F., & Buehler, M. J. (2009). Merger of structure and material in nacre and bone?Perspectives on de novo biomimetic materials. Progress in Materials Science, 54(8), 1059-1100.

[48] Meyers, M. A., McKittrick, J., & Chen, P. Y. (2013). Structural biological materials: critical mechanics-materials connections. science, 339(6121), 773-779.

[49] Porter, M. M., Yeh, M., Strawson, J., Goehring, T., Lujan, S., Siripasopsotorn, P., ... & McKittrick, J. (2012). Magnetic freeze casting inspired by nature. Materials Science and Engineering: A, 556, 741-750.

[50] Munch, E., Launey, M. E., Alsem, D. H., Saiz, E., Tomsia, A. P., & Ritchie, R. O. (2008). Tough, bio-inspired hybrid materials. Science, 322(5907), 1516-1520.

[51] Launey, M. E., Munch, E., Alsem, D. H., Saiz, E., Tomsia, A. P., & Ritchie, R. O. (2010). A novel biomimetic approach to the design of high-performance ceramic?metal composites. Journal of the Royal Society Interface, 7(46), 741-753.

[52] Wang, R. Z., Wen, H. B., Cui, F. Z., Zhang, H. B., & Li, H. D. (1995). Observations of damage morphologies in nacre during deformation and fracture. Journal of Materials Science, 30(9), 2299-2304.

[53] Ritchie, R. O. (2011). The conflicts between strength and toughness. Nature materials, 10(11), 817.

[54] Hunger, P. M., Donius, A. E., & Wegst, U. G. (2013). Platelets self-assemble into porous nacre during freeze casting. Journal of the mechanical behavior of biomedical materials, 19, 87-93.

[55] Bonderer, L. J., Feldman, K., & Gauckler, L. J. (2010). Platelet-reinforced polymer matrix composites by combined gel-casting and hot-pressing. Part I: Polypropylene matrix composites. Composites science and technology, 70(13), 1958-1965.

[56] Tang, Z., Kotov, N. A., Magonov, S., & Ozturk, B. (2003). Nanostructured artificial nacre. Nature materials, 2(6), 413.

[57] Bouville, F., Maire, E., Meille, S., Van de Moortle, B., Stevenson, A. J., & Deville, S. (2014). Strong, tough and stiff bioinspired ceramics from brittle constituents. Nature materials, 13(5), 508.

[58] Jackson, A. P., Vincent, J. F. V., & Turner, R. M. (1989). A physical model of nacre. Composites Science and Technology, 36(3), 255-266.

[59] Bass, J. D. (1995). Elasticity of minerals, glasses, and melts. Mineral physics & crystallography: a handbook of physical constants, 45-63.

[60] Currey, J. D., & Taylor, J. D. (1974). The mechanical behaviour of some molluscan hard tissues. Journal of Zoology, 173(3), 395-406.

[61] Currey, J. D. (1976). Further studies on the mechanical properties of mollusc shell material. Journal of Zoology, 180(4), 445-453.

[62] Verma, D., Katti, K., & Katti, D. (2007). Nature of water in nacre: a 2D Fourier transform infrared spectroscopic study. Spectrochimica Acta Part A: Molecular and Biomolecular Spectroscopy, 67(3-4), 784-788.

[63] Mohanty, B., Katti, K. S., Katti, D. R., & Verma, D. (2006). Dynamic nanomechanical response of nacre. Journal of materials research, 21(8), 2045-2051.

[64] Feng, Q. L., Cui, F. Z., Pu, G., Wang, R. Z., & Li, H. D. (2000). Crystal orientation, toughening mechanisms and a mimic of nacre. Materials Science and Engineering: C, 11(1), 19-25.

[65] Barthelat, F., & Espinosa, H. D. (2007). An experimental investigation of deformation and fracture of nacre?mother of pearl. Experimental mechanics, 47(3), 311-324.

[66] Barthelat, F., Li, C. M., Comi, C., & Espinosa, H. D. (2006). Mechanical properties of nacre constituents and their impact on mechanical performance. Journal of Materials Research, 21(8), 1977-1986.

[67] Bruet, B. J. F., Qi, H. J., Boyce, M. C., Panas, R., Tai, K., Frick, L., & Ortiz, C. (2005). Nanoscale morphology and indentation of individual nacre tablets from the gastropod mollusc Trochus niloticus. Journal of Materials Research, 20(9), 2400-2419.

[68] Smith, B. L., Schffer, T. E., Viani, M., Thompson, J. B., Frederick, N. A., Kindt, J., ... & Hansma, P. K. (1999). Molecular mechanistic origin of the toughness of natural adhesives, fibres and composites. Nature, 399(6738), 761.

[69] Mohanty, B., Katti, K. S., & Katti, D. R. (2008). Experimental investigation of nanomechanics of the mineral-protein interface in nacre. Mechanics Research Communications, 35(1-2), 17-23.

[70] Katti, K. S., Mohanty, B., & Katti, D. R. (2006). Nanomechanical properties of nacre. Journal of Materials Research, 21(5), 1237-1242.

[71] Moshe-Drezner, H., Shilo, D., Dorogoy, A., & Zolotoyabko, E. (2010). Nanometer-Scale Mapping of Elastic Modules in Biogenic Composites: The Nacre of Mollusk Shells. Advanced Functional Materials, 20(16), 2723-2728.

[72] Xu, Z. H., Yang, Y., Huang, Z., & Li, X. (2011). Elastic modulus of biopolymer matrix in nacre measured using coupled atomic force microscopy bending and inverse finite element techniques. Materials Science and Engineering: C, 31(8), 1852-1856.

[73] Stempfl, P., Pantal, O., Njiwa, R. K., Rousseau, M., Lopez, E., & Bourrat, X. (2007). Friction-induced sheet nacre fracture: effects of nano-shocks on cracks location. International Journal of Nanotechnology, 4(6), 712-729.

[74] Stempfl, P. H., Pantal, O., Rousseau, M., Lopez, E., & Bourrat, X. (2010). Mechanical properties of the elemental nanocomponents of nacre structure. Materials Science and Engineering: C, 30(5), 715-721.

[75] Ghosh, P., Katti, D. R., & Katti, K. S. (2007). Mineral proximity influences mechanical response of proteins in biological mineral? protein hybrid systems. Biomacromolecules, 8(3), 851-856.

[76] Barthelat, F., Tang, H., Zavattieri, P. D., Li, C. M., & Espinosa, H. D. (2007). On the mechanics of mother-of-pearl: a key feature in the material hierarchical structure. Journal of the Mechanics and Physics of Solids, 55(2), 306-337.

[77] Meyers, M. A., Lin, A. Y. M., Chen, P. Y., & Muyco, J. (2008). Mechanical strength of abalone nacre: role of the soft organic layer. Journal of the mechanical behavior of biomedical materials, 1(1), 76-85.

[78] Xu, Z. H., & Li, X. (2011). Deformation strengthening of biopolymer in nacre. Advanced Functional Materials, 21(20), 3883-3888.

[79] Schffer, T. E., Ionescu-Zanetti, C., Proksch, R., Fritz, M., Walters, D. A., Almqvist, N., ... & Morse, D. E. (1997). Does abalone nacre form by heteroepitaxial nucleation or by growth through mineral bridges?. Chemistry of Materials, 9(8), 1731-1740.

[80] Weiner, S., & Lowenstam, H. A. (1986). Organization of Extracellularly Mineralized Tissues: A Comparative Study of Biological Crystal Growt. Critical Reviews in Biochemistry, 20(4), 365-408.

[81] Addadi, L., & Weiner, S. (1997). Biomineralization: A pavement of pearl. Nature, 389(6654), 912.

[82] Song, F., & Bai, Y. L. (2003). Effects of nanostructures on the fracture strength of the interfaces in nacre. Journal of Materials Research, 18(8), 1741-1744.

[83] Song, F., Soh, A. K., & Bai, Y. L. (2003). Structural and mechanical properties of the organic matrix layers of nacre. Biomaterials, 24(20), 3623-3631.

[84] Cartwright, J. H., & Checa, A. G. (2007). The dynamics of nacre self-assembly. Journal of the Royal Society Interface, 4(14), 491-504.

[85] Hou, W. T., & Feng, Q. L. (2003). Crystal orientation preference and formation mechanism of nacreous layer in mussel. Journal of Crystal Growth, 258(3-4), 402-408.

[86] Checa AG, Rodraguez-Navarro AB. 2005 Self-organisation of nacre in the shells of Pterioida (Bivalvia: Mollusca). *Biomaterials* 26(9), 1071-1079.

[87] Checa, A. G., Okamoto, T., & Ramrez, J. (2006). Organization pattern of nacre in Pteriidae (Bivalvia: Mollusca) explained by crystal competition. Proceedings of the Royal Society of London B: Biological Sciences, 273(1592), 1329-1337.

[88] Checa, A. G., Cartwright, J. H., & Willinger, M. G. (2011). Mineral bridges in nacre. Journal of structural biology, 176(3), 330-339.

[89] Dimas, L. S., Bratzel, G. H., Eylon, I., & Buehler, M. J. (2013). Tough composites inspired by mineralized natural materials: computation, 3D printing, and testing. Advanced Functional Materials, 23(36), 4629-4638.

[90] Dimas, L. S., & Buehler, M. J. (2014). Modeling and additive manufacturing of bio-inspired composites with tunable fracture mechanical properties. Soft Matter, 10(25), 4436-4442.

[91] Currey, J. D. (1977, April). Mechanical properties of mother of pearl in tension. In Proc. R. Soc. Lond. B (Vol. 196, No. 1125, pp. 443-463). The Royal Society.

[92] Gao, H., Ji, B., Jger, I. L., Arzt, E., & Fratzl, P. (2003). Materials become insensitive to flaws at nanoscale: lessons from nature. Proceedings of the national Academy of Sciences, 100(10), 5597-5600.

[93] Katti, D. R., Katti, K. S., Sopp, J. M., & Sarikaya, M. (2001). 3D finite element modeling of mechanical response in nacre-based hybrid nanocomposites. Computational and Theoretical Polymer Science, 11(5), 397-404.

[94] Katti, K. S., Katti, D. R., Pradhan, S. M., & Bhosle, A. (2005). Platelet interlocks are the key to toughness and strength in nacre. Journal of Materials Research, 20(5), 1097-1100.

[95] Sen, D., & Buehler, M. J. (2011). Structural hierarchies define toughness and defect-tolerance despite simple and mechanically inferior brittle building blocks. Scientific reports, 1, 35.

[96] Katti, D. R., & Katti, K. S. (2001). Modeling microarchitecture and mechanical behavior of nacre using 3D finite element techniques Part I Elastic properties. Journal of Materials Science, 36(6), 1411-1417.

[97] Katti, D. R., Pradhan, S. M., & Katti, K. S. (2004). Modeling the organic-inorganic interfacial nanoasperities in a model bionanocomposite, nacre. Reviews on Advanced Materials Science, 6(2), 162-168.

[98] Evans, A. G., Suo, Z., Wang, R. Z., Aksay, I. A., He, M. Y., & Hutchinson, J. W. (2001). Model for the robust mechanical behavior of nacre. Journal of Materials Research, 16(9), 2475-2484.

[99] Shao, Y., Zhao, H. P., Feng, X. Q., & Gao, H. (2012). Discontinuous crack-bridging model for fracture toughness analysis of nacre. Journal of the Mechanics and Physics of Solids, 60(8), 1400-1419.

[100] Shao, Y., Zhao, H. P., & Feng, X. Q. (2014). On flaw tolerance of nacre: a theoretical study. Journal of The Royal Society Interface, 11(92), 20131016.

[101] Begley, M. R., Philips, N. R., Compton, B. G., Wilbrink, D. V., Ritchie, R. O., & Utz, M. (2012). Micromechanical models to guide the development of synthetic "brick and mortar" composites. Journal of the Mechanics and Physics of Solids, 60(8), 1545-1560.

[102] Askarinejad, S., & Rahbar, N. (2015). Toughening mechanisms in bioinspired multilayered materials. Journal of The Royal Society Interface, 12(102), 20140855.

[103] Dimas, L. S., & Buehler, M. J. (2012). Influence of geometry on mechanical properties of bio-inspired silica-based hierarchical materials. Bioinspiration & biomimetics, 7(3), 036024.

[104] Zhu, T. T., Bushby, A. J., & Dunstan, D. J. (2008). Size effect in the initiation of plasticity for ceramics in nanoindentation. Journal of the Mechanics and Physics of Solids, 56(4), 1170-1185.

[105] Dunstan, D. J., & Bushby, A. J. (2013). The scaling exponent in the size effect of small scale plastic deformation. International Journal of Plasticity, 40, 152-162.

[106] Li, N., Nastasi, M., & Misra, A. (2012). Defect structures and hardening mechanisms in high dose helium ion implanted Cu and Cu/Nb multilayer thin films. International Journal of Plasticity, 32, 1-16.

[107] Salehinia, I., Wang, J., Bahr, D. F., & Zbib, H. M. (2014). Molecular dynamics simulations of plastic deformation in Nb/NbC multilayers. International Journal of Plasticity, 59, 119-132.

[108] Salehinia, I., Shao, S., Wang, J., & Zbib, H. M. (2015). Interface structure and the inception of plasticity in Nb/NbC nanolayered composites. Acta Materialia, 86, 331-340.

[109] Salehinia, I., Shao, S., Wang, J., & Zbib, H. M. (2014). Plastic deformation of metal/ceramic nanolayered composites. JOM, 66(10), 2078-2085.

[110] Dutta, A., Tekalur, S. A., & Miklavcic, M. (2013). Optimal overlap length in staggered architecture composites under dynamic loading conditions. Journal of the Mechanics and Physics of Solids, 61(1), 145-160.

[111] Yao, H., Song, Z., Xu, Z., & Gao, H. (2013). Cracks fail to intensify stress in nacreous composites. Composites Science and Technology, 81, 24-29.

[112] Zhang, Z. Q., Liu, B., Huang, Y., Hwang, K. C., Gao, H. (2010). Mechanical properties of unidirectional nanocomposites with non-uniformly

or randomly staggered platelet distribution. Journal of the Mechanics and Physics of Solids, 58(10), 1646-1660.

[113] Liu, G., Ji, B., Hwang, K. C., Khoo, B. C. (2011). Analytical solutions of the displacement and stress fields of the nanocomposite structure of biological materials. Composites Science and Technology, 71(9), 1190-1195.

[114] Dimas, L. S., Giesa, T., & Buehler, M. J. (2014). Coupled continuum and discrete analysis of random heterogeneous materials: elasticity and fracture. Journal of the Mechanics and Physics of Solids, 63, 481-490.

[115] Jager, I., Fratzl, P. (2000). Mineralized collagen fibrils: a mechanical model with a staggered arrangement of mineral particles. Biophysical Journal, 79(4), 1737-1746.

[116] Wagner, H. D., Weiner, S. (1992). On the relationship between the microstructure of bone and its mechanical stiffness. Journal of Biomechanics, 25(11), 1311-1320.

[117] Kotha, S. P., Kotha, S., Guzelsu, N. (2000). A shear-lag model to account for interaction effects between inclusions in composites reinforced with rectangular platelets. Composites Science and Technology, 60(11), 2147-2158.

[118] Shuchun, Z., Yueguang, W. (2007). Effective elastic modulus of bone-like hierarchical materials. Acta Mechanica Solida Sinica, 20(3), 198-205.

[119] Chen, B., Wu, P. D., Gao, H. (2009). A characteristic length for stress transfer in the nanostructure of biological composites. Composites Science and Technology, 69(7), 1160-1164.

[120] Wei, X., Naraghi, M., Espinosa, H. D. (2012). Optimal length scales emerging from shear load transfer in natural materials: application to carbon-based nanocomposite design. ACS nano, 6(3), 2333-2344.

[121] Li, X., Gao, H., Scrivens, W. A., Fei, D., Thakur, V., Sutton, M. A., ... & Myrick, M. L. (2005). Structural and mechanical characterization of nanoclay-reinforced agarose nanocomposites. Nanotechnology, 16(10), 2020.

[122] Morits, M., Verho, T., Sorvari, J., Liljestrom, V., Kostiainen, M. A., Groschel, A. H., & Ikkala, O. (2017). Toughness and Fracture Properties in NacreMimetic Clay/Polymer Nanocomposites. Advanced Functional Materials.

[123] Niebel, T. P., Bouville, F., Kokkinis, D., & Studart, A. R. (2016). Role of the polymer phase in the mechanics of nacre-like composites. Journal of the Mechanics and Physics of Solids, 96, 133-146.

[124] Long, B., Wang, C. A., Lin, W., Huang, Y., & Sun, J. (2007). Polyacrylamide-clay nacre-like nanocomposites prepared by electrophoretic deposition. Composites Science and Technology, 67(13), 2770-2774.

[125] Bonderer, L. J., Studart, A. R., & Gauckler, L. J. (2008). Bioinspired design and assembly of platelet reinforced polymer films. Science, 319(5866), 1069-1073.

[126] Mammeri, F., Le Bourhis, E., Rozes, L., & Sanchez, C. (2005). Mechanical properties of hybrid organicinorganic materials. Journal of materials chemistry, 15(35-36), 3787-3811.

[127] Chen, R., Wang, C. A., Huang, Y., & Le, H. (2008). An efficient biomimetic process for fabrication of artificial nacre with ordered-nanostructure. Materials Science and Engineering: C, 28(2), 218-222.

[128] Corni, I., Harvey, T. J., Wharton, J. A., Stokes, K. R., Walsh, F. C., & Wood, R. J. K. (2012). A review of experimental techniques to produce a nacre-like structure. Bioinspiration & biomimetics, 7(3), 031001.

[129] Valashani, S. M. M., & Barthelat, F. (2015). A laser-engraved glass duplicating the structure, mechanics and performance of natural nacre. Bioinspiration & biomimetics, 10(2), 026005.

[130] Zlotnikov, I., Gotman, I., Burghard, Z., Bill, J., & Gutmanas, E. Y. (2010). Synthesis and mechanical behavior of bioinspired ZrO2?organic nacre-like laminar nanocomposites. Colloids and Surfaces A: Physicochemical and Engineering Aspects, 361(1-3), 138-142.

[131] Bai, H., Walsh, F., Gludovatz, B., Delattre, B., Huang, C., Chen, Y., ... & Ritchie, R. O. (2016). Bioinspired Hydroxyapatite/Poly (methyl

methacrylate) Composite with a Nacre Mimetic Architecture by a Bidirectional Freezing Method. Advanced Materials, 28(1), 50-56.

[132] Deville, S., Saiz, E., & Tomsia, A. P. (2006). Freeze casting of hydroxyapatite scaffolds for bone tissue engineering. Biomaterials, 27(32), 5480-5489.

[133] Launey, M. E., Munch, E., Alsem, D. H., Barth, H. B., Saiz, E., Tomsia, A. P., & Ritchie, R. O. (2009). Designing highly toughened hybrid composites through nature-inspired hierarchical complexity. Acta Materialia, 57(10), 2919-2932.

[134] Wegst, U. G., Schecter, M., Donius, A. E., & Hunger, P. M. (2010). Biomaterials by freeze casting. Philosophical Transactions of the Royal Society of London A: Mathematical, Physical and Engineering Sciences, 368(1917), 2099-2121.

[135] Liu, M., Sun, J., Sun, Y., Bock, C., & Chen, Q. (2009). Thickness-dependent mechanical properties of polydimethylsiloxane membranes. Journal of micromechanics and microengineering, 19(3), 035028.

[136] Qi, H. J., & Boyce, M. C. (2005). Stress-strain behavior of thermoplastic polyurethanes. Mechanics of Materials, 37(8), 817-839.

[137] ASTM E1820-06. Standard Test Method for Measurement of Fracture Toughness Annual Book of ASTM Standards, Vol. 03.01: Metals - Mechanical Testing; Elevated and Low-temperature Tests; Metallography (ASTM International, West Conshohocken, Pennsylvania, USA, 2006).

[138] Hedgepeth, J. M. (1961). Stress concentrations in filamentary structures.

[139] Nairn, J. A. (1988). Fracture mechanics of unidirectional composites using the shear-lag model I: theory. Journal of composite materials, 22(6), 561-588.

[140] Nairn, J. A., & Mendels, D. A. (2001). On the use of planar shear-lag methods for stress-transfer analysis of multilayered composites. Mechanics of Materials, 33(6), 335-362.

[141] Benveniste, Y., & Miloh, T. (1986). The effective conductivity of composites with imperfect thermal contact at constituent interfaces. International Journal of Engineering Science, 24(9), 1537-1552.

[142] Cheng, Z. Q., He, L. H., & Kitipornchai, S. (2000). Influence of imperfect interfaces on bending and vibration of laminated composite shells. International Journal of Solids and Structures, 37(15), 2127-2150.

[143] Wang, Z., Zhu, J., Jin, X. Y., Chen, W. Q., & Zhang, C. (2014). Effective moduli of ellipsoidal particle reinforced piezoelectric composites with imperfect interfaces. Journal of the Mechanics and Physics of Solids, 65, 138-156.

[144] Hashin, Z. (1991). Composite materials with interphase: thermoelastic and inelastic effects. In Inelastic Deformation of Composite Materials (pp. 3-34). Springer New York.

[145] Gu, S. T., He, Q. C., & Pensee, V. (2015). Homogenization of fibrous piezoelectric composites with general imperfect interfaces under antiplane mechanical and in-plane electrical loadings. Mechanics of Materials, 88, 12-29.

[146] Nairn, J. A., & Liu, Y. C. (1997). Stress transfer into a fragmented, anisotropic fiber through an imperfect interface. International Journal of Solids and Structures, 34(10), 1255-1281.

[147] Nairn, J. A. (2007). Numerical implementation of imperfect interfaces. Computational Materials Science, 40(4), 525-536.

[148] Martin, P. A. (1992). Boundary integral equations for the scattering of elastic waves by elastic inclusions with thin interface layers. Journal of nondestructive evaluation, 11(3-4), 167-174.

[149] H. Tada, P. C Paris,G. R Irwin (2000). The analysis of cracks handbook (pp. 58-58). New York: ASME Press. Chicago.

[150] Munch, E., Launey, M. E., Alsem, D. H., Saiz, E., Tomsia, A. P., & Ritchie, R. O. (2008). Tough, bio-inspired hybrid materials. Science, 322(5907), 1516-1520.

[151] Thouless, M. D., & Evans, A. G. (1988). Effects of pull-out on the mechanical properties of ceramic-matrix composites. Acta Metallurgica, 36(3), 517-522.

[152] Marshall, D. B., Evans, A. G., Drory, M., Bradt, R. C., Evans, A. G., Hasselman, D. P. H., & Lange, F. F. (1986). Fracture mechanics of ceramics.

[153] Phillips, D. C. (1972). The fracture energy of carbon-fibre reinforced glass. Journal of Materials Science, 7(10), 1175-1191.

[154] Marshall, D. B., & Evans, A. G. (1985). Failure Mechanisms in Ceramic-Fiber/Ceramic-Matrix Composites. Journal of the American Ceramic Society, 68(5), 225-231.

[155] Cox, B. N., & Marshall, D. B. (1994). Concepts for bridged cracks in fracture and fatigue. Acta Metallurgica et Materialia, 42(2), 341-363.

[156] Stewart, R. L., Chyung, K., Taylor, M. P., Cooper, R. F., Bradt, R. C., Evans, A. G., ... & Lange, F. F. (1986). Fracture Mechanics of Ceramics. Plenum Press, NY, 33.

[157] Curkovic, L., Bakic, A., Kodvanj, J., & Haramina, T. (2010). Flexural strength of alumina ceramics: Weibull analysis. Transactions of FAMENA, 34(1), 13-19.

[158] Evans, A. G., & McMeeking, R. M. (1986). On the toughening of ceramics by strong reinforcements. Acta Metallurgica, 34(12), 2435-2441.

[159] Dastjerdi, A. K., Rabiei, R., & Barthelat, F. (2013). The weak interfaces within tough natural composites: experiments on three types of nacre. Journal of the mechanical behavior of biomedical materials, 19, 50-60.

[160] Zhang, Y., Gong, S., Zhang, Q., Ming, P., Wan, S., Peng, J., ... & Cheng, Q. (2016). Graphene-based artificial nacre nanocomposites. Chemical Society Reviews, 45(9), 2378-2395.

[161] de Obaldia, E. E., Jeong, C., Grunenfelder, L. K., Kisailus, D., & Zavattieri, P. (2015). Analysis of the mechanical response of biomimetic

materials with highly oriented microstructures through 3D printing, mechanical testing and modeling. Journal of the mechanical behavior of biomedical materials, 48, 70-85.

[162] Libonati, F., Gu, G. X., Qin, Z., Vergani, L., & Buehler, M. J. (2016). Bone?Inspired Materials by Design: Toughness Amplification Observed Using 3D Printing and Testing. Advanced Engineering Materials, 18(8), 1354-1363.

[163] Zhang, P., Heyne, M. A., & To, A. C. (2015). Biomimetic staggered composites with highly enhanced energy dissipation: Modeling, 3D printing, and testing. Journal of the Mechanics and Physics of Solids, 83, 285-300.

[164] Lipson, H., & Kurman, M. (2013). Fabricated: The new world of 3D printing. John Wiley & Sons.

[165] Tang, H., Barthelat, F., & Espinosa, H. D. (2007). An elasto-viscoplastic interface model for investigating the constitutive behavior of nacre. Journal of the Mechanics and Physics of Solids, 55(7), 1410-1438.

[166] Malik, I. A., & Barthelat, F. (2016). Toughening of thin ceramic plates using bioinspired surface patterns. International Journal of Solids and Structures, 97, 389-399.

[167] Bai, X., Lee, A. W., Thompson, L. L., & Rosowsky, D. V. (2007). Finite element analysis of Moso bamboo-reinforced southern pine OSB composite beams. Wood and fiber science, 31(4), 403-415.

[168] Li, S. H., Zeng, Q. Y., Xiao, Y. L., Fu, S. Y., & Zhou, B. L. (1995). Biomimicry of bamboo bast fiber with engineering composite materials. Materials Science and Engineering: C, 3(2), 125-130.

[169] Nugroho, N., & Ando, N. (2001). Development of structural composite products made from bamboo II: fundamental properties of laminated bamboo lumber. Journal of wood science, 47(3), 237.

[170] Lee, A. W., Bai, X., & Bangi, A. P. (1997). Flexural properties of bamboo-reinforced southern pine OSB beams. Forest products journal, 47(6), 74.

[171] Askarinejad, S., Rahbar, N., Sabelkin, V., Mall, S. (2015). Mechanical behavior of a notched oxide/oxide ceramic matrix composite in combustion environment: experiments and simulations. Composite Structures, 127, 77-86.

[172] Bathe, K.J. (1996) Finite element procedures. Prentice-Hall, Englewood Cliffs

[173] Cook, R.D., Malkus, D.S., Plesha, M.E., Witt, R.J. (2002) Concepts and applications of finite element analysis 4th edn. John Wiley and Sons, USA

[174] Sanchez-Palencia, E. (1980) Non-homogeneous media and vibration. Theory lecture notes in physics 127. Springer, Berlin

[175] Santare, M. H., & Lambros, J. (2000). Use of graded finite elements to model the behavior of nonhomogeneous materials. Journal of Applied Mechanics, 67(4), 819-822.

[176] Kim, J. H., & Paulino, G. H. (2002). Isoparametric graded finite elements for nonhomogeneous isotropic and orthotropic materials. Journal of Applied Mechanics, 69(4), 502-514.

[177] Amada, S., Ichikawa, Y., Munekata, T., Nagase, Y., & Shimizu, H. (1997). Fiber texture and mechanical graded structure of bamboo. Composites Part B: Engineering, 28(1-2), 13-20.

[178] Shin, F. G., Xian, X. J., Zheng, W. P., Yipp, M. W. (1989). Analyses of the mechanical properties and microstructure of bamboo-epoxy composites. Journal of materials science, 24(10), 3483-3490.

[179] Budiansky, B., Amazigo, JC., Evans, AG.(1988). Small-scale crack bridging and the fracture toughness of particulate-reinforced ceramics. J Mech Phys Solids, 36(2),16787.

[180] Bloyer, D. R., Rao, K. T. V., Ritchie, R. O. (1998). Fracture toughness and R-curve behavior of laminated brittle-matrix composites. Metall Mater Trans A, 29A (10), 248396.

[181] Bloyer, D. R., Rao, K. T. V., Ritchie, R. O. (1999). Fatigue-crack propagation behavior of ductile/ brittle laminated composites. Metall Mater Trans A, 30A (3), 63342.

[182] Fett, T., Munz, D. (1994) Stress intensity factors and weight functions for one dimensional cracks, Report KfK 5290. Karlsruhe: Institut fur Material forschung.

[183] Sekhar, A. C., Bhartari, R. K. (1960). Studies on strength of Bamboos: a note on its mechanical behaviour. Indian Forester, 86(5), 296-301.

[184] Mousanezhad, D., Ebrahimi, H., Haghpanah, B., Ghosh, R., Ajdari, A., Hamouda, A. M. S., Vaziri, A. (2015). Spiderweb honeycombs. International Journal of Solids and Structures, 66, 218-227.

[185] Shalchy, F., Rahbar, N. (2015). Nanostructural Characteristics and Interfacial Properties of Polymer Fibers in Cement Matrix. ACS applied materials and interfaces, 7(31), 17278-17286.

[186] Salahshoor, H., Rahbar, N. (2012). Nano-scale fracture toughness and behavior of graphene/epoxy interface. Journal of Applied Physics, 112(2), 023510.

[187] Shiji, Y., Muramoto, Y., Shimizu, N. (2004, October). Electrical insulating properties of bamboo and effect of water absorption on them. In Electrical Insulation and Dielectric Phenomena, 2004. CEIDP'04. 2004 Annual Report Conference on (pp. 348-351). IEEE.

[188] Askeland, D. R., & Phule, P. P. (2003). The Science and Engineering of Materials, Brooks/Cole. Cerca con Google.

[189] Amada, S., & Lakes, R. S. (1997). Viscoelastic properties of bamboo. Journal of Materials Science, 32(10), 2693-2697.

[190] Wang, S., Zhu, X., Li, Q., Wang, R., & Wang, X. (2016). Damage-tolerance strategies for nacre tablets. Journal of structural biology, 194(2), 199-204.

[191] Li, R., He, C., Cheng, L., Lin, G., Wang, G., Shi, D., ... & Yang, Y. (2017). Polyoxometalate-enabled photoreduction of graphene oxide to bioinspired nacre-like composite films for supercapacitor electrodes. Composites Part B: Engineering, 121, 75-82.

[192] Wu, Y., Cao, R., Wu, G., Huang, W., Chen, Z., Yang, X., & Tu, Y. (2016). From ultratough artificial nacre to elastomer: Poly (n-butyl

acrylate) grafted graphene oxide nanocomposites. Composites Part A: Applied Science and Manufacturing, 88, 156-164.

[193] Flores-Johnson, E. A., Shen, L., Guiamatsia, I., & Nguyen, G. D. (2014). Numerical investigation of the impact behaviour of bioinspired nacre-like aluminium composite plates. Composites Science and Technology, 96, 13-22.